

**Cell type-focused compound screen in human organoids  
reveals molecules and pathways controlling cone  
photoreceptor death**

**Inauguraldissertation**

zur

Erlangung der Würde eines Doktors der Philosophie

vorgelegt der

Philosophisch-Naturwissenschaftlichen Fakultät

der Universität Basel

von

**Stefan Spirig**

**2024**

Originaldokument gespeichert auf dem Dokumentenserver der Universität Basel  
edoc.unibas.ch

Genehmigt von der Philosophisch-Naturwissenschaftlichen Fakultät  
auf Antrag von

Erstbetreuer/in: Prof. Dr. Botond Roska

Zweitbetreuer/in: Prof. Dr. Fiona Doetsch

Externe/r Experte/in: Prof. Dr. Stephan C. F. Neuhauss

Basel, den 19.12.2023

Prof. Dr. Marcel Mayor

Dekan





# Table of contents

<b>1 Acknowledgments .....</b>	<b>1</b>
<b>2 Introduction.....</b>	<b>2</b>
2.1 <i>Human organoid generation .....</i>	2
2.2 <i>Human organoid applications and screening .....</i>	4
2.3 <i>Cell types and selective vulnerability.....</i>	5
2.4 <i>The human retina and photoreceptors .....</i>	5
2.5 <i>Retinal diseases and degeneration.....</i>	8
2.6 <i>Human retinal organoids to study retinal degeneration .....</i>	11
<b>3 Aim of this thesis .....</b>	<b>13</b>
<b>4 Manuscript information .....</b>	<b>14</b>
4.1 <i>Detailed author contributions .....</i>	14
<b>5 Manuscript.....</b>	<b>15</b>
<i>SUMMARY .....</i>	16
<i>INTRODUCTION.....</i>	17
<i>RESULTS.....</i>	20
<i>DISCUSSION .....</i>	41
<i>ACKNOWLEDGMENTS.....</i>	46
<i>AUTHOR CONTRIBUTIONS .....</i>	46
<i>MATERIALS AND METHODS .....</i>	47
<i>SUPPLEMENTARY FIGURES AND SUPPLEMENTARY FIGURE LEGENDS.....</i>	63
<i>REFERENCES .....</i>	77
<b>6 Discussion and outlook .....</b>	<b>83</b>
6.1 <i>Organoids for drug discovery screening.....</i>	83
6.2 <i>Organoids to predict side effects.....</i>	85

<i>6.3 Limitations of human retinal organoids</i> .....	85
<i>6.4 CS-KI-1 and CS-KI-2 as potential cone-protective agents</i> .....	86
<b>7 Concluding remarks</b> .....	<b>88</b>
<b>8 References</b> .....	<b>89</b>
<b>9 Appendix: manuscript supplementary tables</b> .....	<b>95</b>

# 1 Acknowledgments

This thesis was made possible through the support and contributions of many. I wish to thank my principal advisor Botond Roska for his consistent support and collaborative efforts. I also thank Gray Camp, Fiona Doetsch, and Stephan Neuhaus, as former and current members of my PhD committee, for their guidance.

I am grateful for the following funding that supported this work: European Research Council advanced grant HURET N°883781, Swiss National Science Foundation Synergia grant CRSII3\_141801, Swiss National Science Foundation grant 310030\_212186, a Louis-Jeantet Foundation award, a Körber Foundation award, an NCCR Molecular Systems Engineering grant, all awarded to Botond Roska, as well as the IOB PhD and MD-PhD program on Translational Visual Neurosciences.

I acknowledge my collaborators Valeria J. Arteaga-Moreta, Zoltan Raics, Susana Posada-Céspedes, P. Timo Kleindienst, Adrienn Volak, Jannick Imbach, Svitlana Malysheva, Rebecca A. Siwicki, Vincent Hahaut, Yanyan Hou, Simone Picelli, Marco Cattaneo, Josephine Jüttner, Cameron S. Cowan, and Magdalena Renner, all of whom are former or current IOB members, for their contributions.

Thanks are also extended to Larissa Utz, Alissa Muller, Tiago M. Rodrigues, Alex Fratzl, Tamas Dalmay, and Patrick King for their comments on the manuscript, and to the entire Roska lab at IOB for stimulating discussions.

I appreciate the collaboration of Stephanie Chreng, Olaf Galuba, Inga Galuba, Isabelle Claerr, Steffen Renner, Myriam Duckely, Daniel K. Baeschlin, and Vincent Unterreiner from the Novartis Chemical Biology and Therapeutics department, as well as the FAST Lab at Novartis.

Special thanks go to my dear friends Verónica Moreno-Juan and Álvaro Herrero-Navarro from the Roska group for their assistance and encouragement.

I am grateful to my entire family, but especially my mother Guiomar Spirig-Velandia and my sisters Gabriela Spirig, and Natalia Ramirez, for their constant encouragement and support.

Last but not least, I thank Lisa Bachmann, for standing by me throughout this journey.

## **2 Introduction**

### **2.1 Human organoid generation**

Organoids are three-dimensional cellular assemblies that replicate the cellular composition, structural organization and, in some cases, the function of their corresponding organ (Lancaster and Knoblich 2014; Clevers 2016; Paşca et al. 2022). Organoids have become innovative model systems, providing insights into developmental processes as well as the intricate biology of tissues and organs (Rossi et al. 2018). Additionally, they are increasingly utilized as potential sources of cells or tissues for transplantation purposes (Sağraç et al. 2021) and may play an important role in evaluating the feasibility and safety of novel therapeutic strategies in the future (Kim et al. 2019). A wide range of organoids have been generated that model organs such as the brain, retina, gastrointestinal tract, thyroid, heart, vasculature, lung, liver, pancreas, kidney, female and male reproductive tracts, and the placenta (Rossi et al. 2018; Chumduri and Turco 2021; Tang et al. 2022; Patrício et al. 2023).

Organoids are generated from stem cells, including organ-specific adult stem cells, embryonic stem cells, or induced pluripotent stem cells (iPSCs). Adult organ stem cells, which are undifferentiated cells located in mature tissues, are capable of self-renewal and differentiation into the specialized cell types of their resident organ (Clevers and Watt 2018). A well-known example is that of hematopoietic stem cells in the bone marrow, which have the ability to differentiate into various types of blood cells, including red blood cells, white blood cells, and platelets (Morrison et al. 1995). Numerous organs across the body contain stem cells that play a crucial role in tissue renewal and repair after damage (Montagnani et al. 2016). Cells harvested from tissue biopsies and samples enable the development and cultivation of organoids that closely replicate the structure and function of their native organ (Drost and Clevers 2017). Organoid models, such as those of the intestine, liver, and lungs, are commonly produced using tissue-derived stem cells (Choi et al. 2016; Hindley et al. 2016; Pleguezuelos-Manzano et al. 2020) (Figure 1).

Pluripotent stem cells are able to differentiate into nearly any cell type of the body. These cells can be derived from embryos, known as embryonic stem cells, or reprogrammed from differentiated

cells to form iPSCs (Romito and Cobellis 2016). iPSCs are created by inducing a pluripotent state through the expression of four key transcription factors: OCT4, KLF4, SOX2, and MYC (Takahashi and Yamanaka 2006; Takahashi et al. 2007). Embryonic stem cells and iPSCs are both utilized to generate a wide variety of organoids, including those that mimic the retina and the brain (Rossi et al. 2018) (Figure 1).

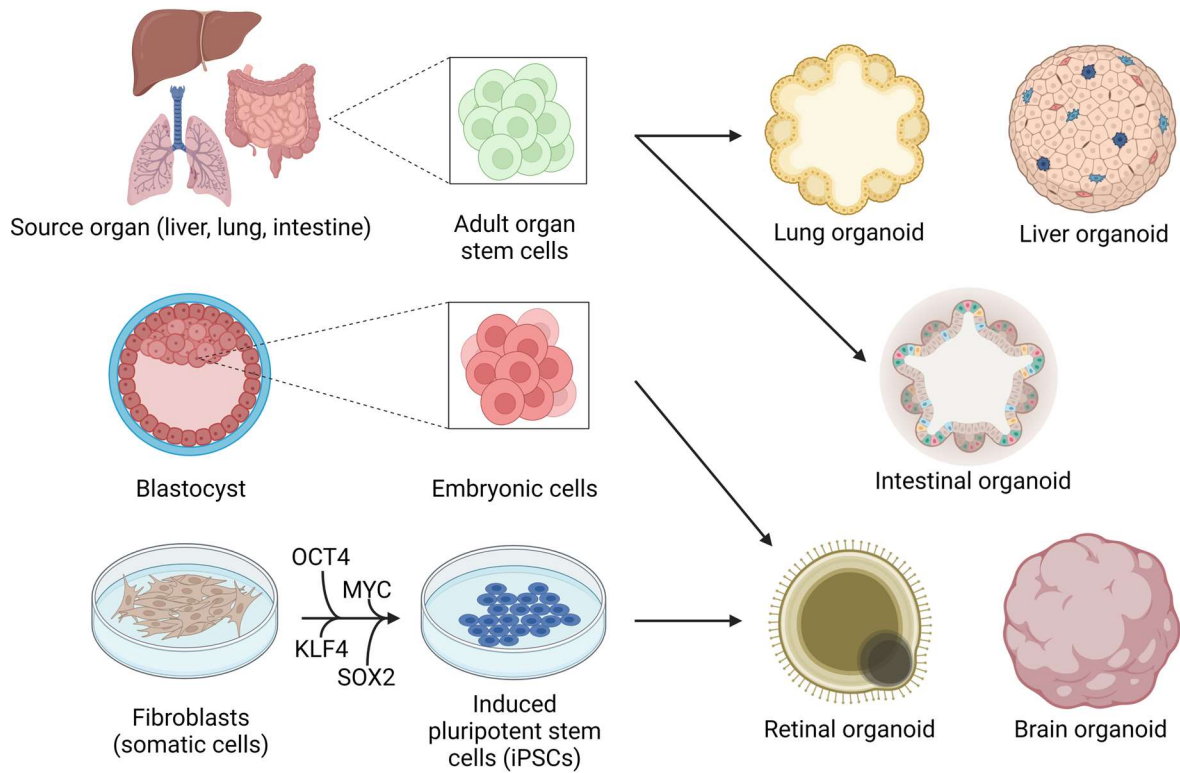


**Figure 1: Stem cells and organoids.** Schematic illustration of different types of stem cells, along with their respective methods of generation or isolation, and common types of organoids into which they can typically differentiate.

## 2.2 Human organoid applications and screening

Much of the current organoid research concentrates on defining and improving these new models, but they have already significantly advanced our understanding of development and tissue biology. Intestinal organoids have provided insights into the role of enteroendocrine cells, revealing the influence of BMP signaling on hormone expression, a finding that has been validated by subsequent studies using animal models (Basak et al. 2017; Beumer et al. 2018). Organoids also hold promise in virology, offering insights into infectious diseases that surpass those derived from traditional 2D cell cultures. For instance, human brain organoids used to study the replication dynamics of Zika and Herpes Simplex viruses have generated more in-depth findings than conventional cell culture systems (Krenn et al. 2021).

One significant advantage of organoids over animal models is their potential for ethical and scalable production, potentially facilitating their application in high-throughput drug screening (Spirig and Renner 2023). High-throughput screening is crucial to drug discovery, typically involving assays that assess the binding or inhibition of well-defined, isolated targets or that employ 2D cell cultures to replicate disease phenotypes, such as abnormal growth in cancer research (Houston and Banks 2003; Blay et al. 2020; Fen et al. 2021). Initial large-scale screening using organoids has employed cancer organoids. These are cultured from tumor tissues taken from biopsies or surgical excisions (Jin et al. 2018) and show great promise for personalized medicine. In some cases, organoid experiments have successfully predicted the responses of patients to certain treatments. Despite the variety of patient samples used in such screenings, fewer than sixty compounds have so far been evaluated per screen (Broutier et al. 2017; Toshimitsu et al. 2022).

Lukonin et al. and Chen et al. stand out as pioneering studies in the domain of large-scale testing of compounds on non-cancer organoids. Lukonin et al. conducted a screen with mouse intestinal organoids on the effects of numerous compounds on organoid development (Lukonin et al. 2020). Chen et al. conducted a compound screen on maintaining photoreceptor survival using dissociated cells derived from mouse retinal organoids (Chen et al. 2023). However, prior to our work as presented here, large-scale compound screens on human organoids had not been performed.

## **2.3 Cell types and selective vulnerability**

Organs and tissues are composed of various cell types with specific roles. Traditionally, cell types have been defined by their morphology, marker gene expression, and in some cases by their function, such as the electrophysiological properties characteristic of neurons (McKinley et al. 2020). Today, single-cell technologies like single-cell RNA sequencing allow high-throughput analysis of individual cell transcriptomes (Weaver et al. 2014; Sagar et al. 2018). Numerous organoid models studied with this technology have shown that organoid transcriptomes closely mirror those of the corresponding human organs, for example brain, retina, and intestine (Haber et al. 2017; Velasco et al. 2019; Cowan et al. 2020).

The study of cell types is of critical importance in medical research, as many diseases selectively target specific cells. In Type 1 diabetes, the immune system targets and destroys pancreatic beta-cells (Burrack et al. 2017). Podocytes, the key to blood filtration, are susceptible to kidney diseases like focal segmental glomerulosclerosis (Kwiatkowska et al. 2020). Even in the central nervous system, which contains an immense variety of cell types (Tremblay 2020), diseases may affect only a small subset. The motor symptoms of Parkinson's disease are mainly due to selective loss of dopaminergic neurons in the ventral substantia nigra pars compacta (Raza et al. 2019). Similarly, Huntington's disease predominantly affects medium spiny GABAergic neurons located in the striatum (McColgan and Tabrizi 2018).

Thus, given that organoids reflect the cell types of their respective organs, they present significant opportunities for disease research: testing potential therapies for efficacy on specific target cell types.

## **2.4 The human retina and photoreceptors**

A prime example of an organ with a variety of functionally distinct cell types is the retina. The human retina is a complex, multilayered sensory membrane lining the inner posterior segment of the eye that plays a crucial role in visual perception. This neural tissue converts light stimuli into electrical signals that are then transmitted to the brain through the optic nerve. Structurally, the



various cellular layers of the retina, such as the ganglion cell layer, inner nuclear layer, and outer nuclear layer, each contain specific cell types important for visual processing. These cell types mainly form connections with each other through synapses located in the outer and inner plexiform layers (Dowling 2012) (Figure 2).

Photoreceptor cells, bipolar cells, and ganglion cells are the primary neuronal components, whereas Müller cells and microglia are the main glial elements (Masland 2012). Photoreceptors detect light and convey visual information to around ten distinct varieties of bipolar cells. These then relay the visual information to a more diverse array of ganglion cells. Serving as the retina's output neurons, the ganglion cells have axons that come together and create the optic nerve, constituting a pathway that transmits information to other parts of the brain. Horizontal cells play a role in shaping the information flow from photoreceptors to bipolar cells, whereas a range of amacrine cell types modulate information transfer from bipolar cells to ganglion cells (Dowling 2012) (Figure 2).

Photoreceptors consist of two main classes called rods and cones. Rods, characterized by their cylindrical shape, are predominant and are distributed throughout the retina except for the fovea, which is the most central part of the retina and allows high-acuity vision. Rods exhibit high sensitivity to low light levels, such as at dusk. Cones, tapered in structure, are concentrated in the fovea and facilitate high acuity and trichromatic vision (Kawamura and Tachibanaki 2008; Arshavsky and Burns 2012) (Figure 2).

Photoreceptors contain outer segments that are rich in photopigments. Upon absorption of a photon, these photopigments undergo conformational changes that trigger a phototransduction cascade. This cascade leads ultimately to hyperpolarization of the photoreceptor membrane and modulates glutamate release at synaptic terminals, subsequently affecting downstream neurons (Yarfitz and Hurley 1994).

The retinal pigment epithelium (RPE), a monolayer of pigmented cells in close contact with the photoreceptors, is also essential for the visual cycle (Figure 2). The RPE recycles retinal, which is the main cofactor of photopigments, and facilitates the daily shedding and renewal of

photoreceptor outer segment discs. It also provides nourishment and structural support to the photoreceptors (Strauss 2005).

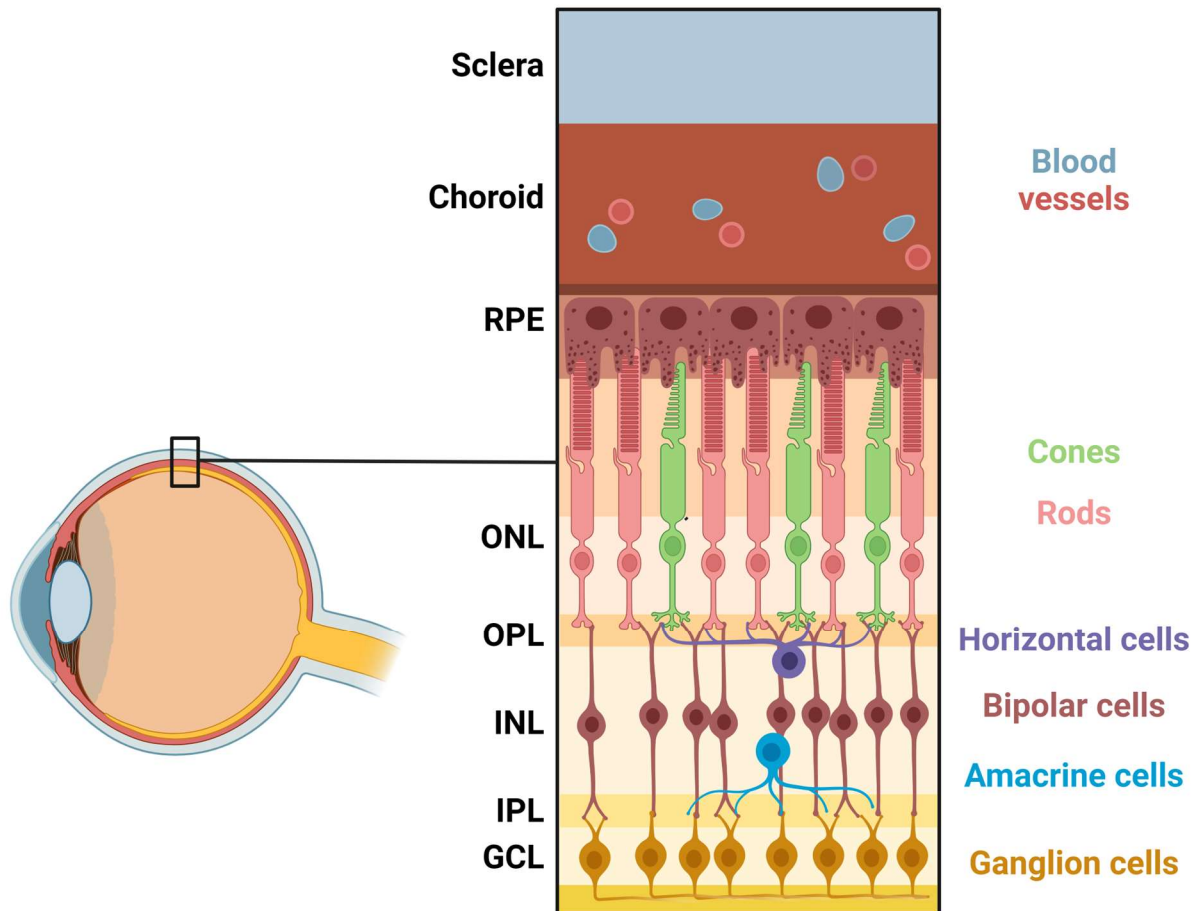


**Figure 2: Human retina and its cell types.** Left: Schematic representation of the human eye with the area of interest indicated for a detailed view on the right. Right: Detailed schematic of the posterior section of the eye, with tissue layers labeled on the left. RPE: Retinal Pigment Epithelium, ONL: Outer Nuclear Layer, OPL: Outer Plexiform Layer, INL: Inner Nuclear Layer, IPL: Inner Plexiform Layer, GCL: Ganglion Cell Layer. The cell types are color-coded and labeled on the right.

## **2.5 Retinal diseases and degeneration**

The retina is susceptible to a variety of diseases that may eventually result in blindness. The three most common blinding conditions diabetic retinopathy, glaucoma, and age-related macular degeneration (AMD) (D'Amico 1994), each have very limited treatment options.

Diabetic retinopathy is a complication stemming from diabetes that impacts blood vessels in the retina, potentially leading to microaneurysms, bleeding, and the formation of new, abnormal blood vessels, all of which can culminate in blindness (Cheung et al. 2010). Glaucoma results in degeneration of retinal ganglion cells that comprise the optic nerve, and is commonly associated with increased intraocular pressure (Morgan 2012). AMD, predominantly observed in the elderly, leads to dysfunction and/or degeneration of RPE cells and photoreceptors (Fleckenstein et al. 2021).

Beyond blood vessels and the RPE, ganglion cells and photoreceptors stand out as the primary cell classes vulnerable to retinal diseases. In the experimental part of this thesis, we focus specifically on strategies to delay degeneration of cones.

### **2.5.1 Retinitis pigmentosa**

Another prevalent category of diseases that impacts photoreceptors is inherited retinal dystrophies typically caused by a single defective gene. A well-known condition within this group is retinitis pigmentosa, encompassing a variety of genetic disorders that lead to degeneration of photoreceptors and affect over 5 million individuals worldwide (Parmeggiani 2011). The disease primarily impacts rods, where the associated genes are predominantly expressed. While the mechanisms of rod degeneration are not fully understood, they are thought to result directly from the mutated genes (Humphries et al. 1992; Ferrari et al. 2011). Rod loss results in minor or no visual impairments as these cells primarily function under very dim light conditions, i.e., under situations that are less common in daily human activities (Zeitz et al. 2015). Unfortunately, the death of rods triggers cone degeneration, leading ultimately to significant visual impairment or blindness (Narayan et al. 2016).

The connection between loss of rods and cone death is not completely understood. However, several hypotheses suggest that the absence of rods creates an unfavorable retinal environment for cones. Key factors implicated in secondary cone degeneration include inflammation, dysregulation of retinal oxygen homeostasis, disruption of nutrient supply, and lack of rod-derived trophic support (Narayan et al. 2016) (Figure 3).

In terms of inflammatory processes, microglia, which are resident immune cells in the retina, are activated by the dying rods, inducing a state of inflammation that subsequently affects the cones (Gupta et al. 2003). Photoreceptors in a healthy retina consume a significant amount of oxygen (Caprara and Grimm 2012) and one potential explanation for cone death is that rod degeneration leads to an excess of oxygen that damages the cones (Shen et al. 2005) (Figure 3).

Nutrient supply is another potential aspect by which the death of rods impacts nutrient availability for cones. In addition to playing a critical role in phototransduction and maintaining photoreceptor outer segments, the RPE serves as the primary conduit for photoreceptor nutrition (Lakkaraju et al. 2020). The photoreceptor layer of the retina lacks a direct blood supply. Instead, nutrients sourced from the choroid, a blood vessel-rich tissue situated between the sclera and the retina, traverse the RPE and reach the photoreceptors (Linsenmeier and Padnick-Silver 2000). The relationship between photoreceptors and the RPE is significantly compromised by rod degeneration, potentially leading to a nutrient deficit for the cones (Punzo et al. 2009; Newton and Megaw 2020) (Figure 3).

Rods themselves secrete trophic factors essential for cone survival (Mohand-Said et al. 1998), including the rod-derived cone viability factor (rdCVF) that has been shown to enhance cone viability when administered exogenously (Léveillard et al. 2004; Aït-Ali et al. 2015). RdCVF regulates glucose uptake and, thus, reduced rdCVF levels due to rod death might result in decreased glucose uptake and cone starvation (Krol and Roska 2015) (Figure 3).

Building on these hypotheses, we opted in the course of our work to simulate secondary cone degeneration associated with retinitis pigmentosa in human retinal organoids through glucose starvation.

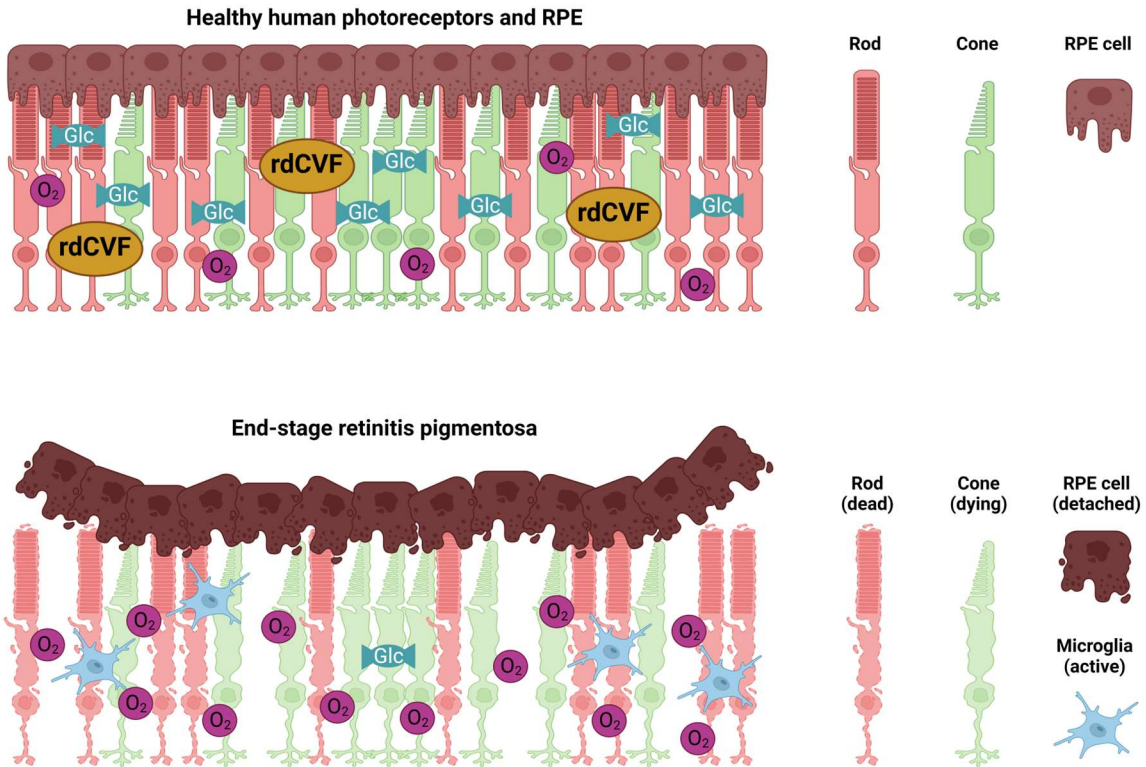


**Figure 3: Potential mechanisms of secondary cone death in retinitis pigmentosa.** Top: Schematic illustration of healthy human photoreceptors and the retinal pigment epithelium (RPE). Bottom: Schematic illustration of human photoreceptors and RPE in end-stage retinitis pigmentosa. RPE, retinal pigment epithelium; rdCVF, rod-derived cone viability factor; Glc, glucose; O<sub>2</sub>, oxygen.

## **2.6 Human retinal organoids to study retinal degeneration**

In terms of cell type complexity, structural organization, and functional mimicry, retinal organoids are particularly notable compared to other organoid types. They develop all major neuronal cell classes, including cones, rods, bipolar cells, amacrine cells, and ganglion cells, and also contain Müller glia cells. These cell types are organized into five layers that mirror the structure of adult human retina and have been shown to respond to light (Zhong et al. 2014; Cowan et al. 2020; Saha et al. 2022).

Retinal organoids are primarily used for studying retinal development and diseases, or as a cell source for transplantation studies (Sharma et al. 2020). Progress in both areas has refined generation techniques, culminating in protocols for the mass-production of these organoids (Spirig and Renner 2023).

Most research on retinal dystrophies has been carried out using animal models. Although this has significantly advanced our understanding of the retina and potential disease mechanisms, treatment options for most retinal diseases are still limited or absent. Furthermore, therapies developed in animal models have frequently failed to translate to clinical settings (Slijkerman et al. 2015). Given their close resemblance to the human retina, human retinal organoids offer a new and promising avenue to study retinal degenerative diseases and to test potential therapies (Aasen and Vergara 2020).

Researchers have already modeled retinal diseases using human retinal organoids with varying degrees of success. Organoids have been generated that harbor a disease-specific mutation and result in a range of phenotypes. Typically, these phenotypes are quite mild and require complex analysis for detection (Lane et al. 2020; Mayerl et al. 2022). Conversely, human retinal organoids carrying a mutation associated with Stargardt disease, or Usher syndrome-associated retinitis pigmentosa that leads to photoreceptor degeneration, exhibit virtually no degenerative phenotype (Leong et al. 2022; Muller et al. 2023).

This thesis aims to address the scarcity of easily identifiable phenotypes and the lack of expertise in mass-producing retinal organoids that have impeded the application of retinal organoids in large-scale screenings and drug discovery.

### **3 Aim of this thesis**

Human organoids are innovative model systems that can be produced on a large scale while adhering to ethical standards and they are thus viable candidates for high-throughput drug-discovery screenings. Despite this potential, such extensive screens remain a barely explored territory. In this thesis, we conducted a screen of 2,707 compounds with annotated targets across 20,000 human retinal organoids.

Cone degeneration is a devastating event in various ocular diseases, including AMD and retinitis pigmentosa. Numerous research endeavors and therapy developments are underway, but a treatment that significantly decelerates vision loss remains elusive. We employed human retinal organoids to model cone death through glucose deprivation, aiming to identify compounds that either slow down or accelerate cone degeneration. Compounds demonstrating protective effects on cones in organoids could pave the way to new interventions to curb cone loss. Conversely, compounds accelerating cone death, along with their associated targets, hold value for safety evaluation of novel compounds destined for clinical trials. Leveraging a library of compounds with known targets, our goal was to unveil protein targets or pathways instrumental in modulating cone degeneration.



## 4 Manuscript information

The following manuscript was published on the preprint server bioRxiv on October 11, 2023:

Spirig, Stefan E., et al. "Cell type-focused compound screen in human organoids reveals molecules and pathways controlling cone photoreceptor death." bioRxiv (2023).

In addition, the manuscript has been submitted to a peer-reviewed journal and is currently under review.

### 4.1 Detailed author contributions

The following manuscript was a collaborative effort and a designated author-contribution section is detailed therein. The manuscript was jointly written by Stefan E. Spirig and Botond Roska with occasional input and revisions from others. The figures were primarily prepared by Stefan E. Spirig except for Figures 1C, 2A, 3A, and 4A, which were designed by Valeria Arteaga-Moreta, Figures 6B-D by Susana Posada-Cespedes, and Figure S10 by Svitlana Malysheva. These figures were later refined by Stefan E. Spirig.

Stefan E. Spirig participated and led all experiments outlined in the manuscript, except for those presented in Figures S1A, S9A and S9B (see author contributions in the manuscript for details). Data analysis was a collective endeavor. Manual quantifications and simple image processing were done by Stefan E. Spirig. Zoltan Raics performed automated cell counting for all live-imaging segments. After quantification, subsequent analysis was carried out by Stefan E. Spirig under the guidance of Botond Roska and Marco Cattaneo. An exception is the analysis presented in Figure S8E that was largely completed by Steffen Renner, and the RNA-sequencing analysis (Figure 6) that was principally conducted by Susana Posada-Cespedes, with occasional contributions from Stefan E. Spirig.

The remainder of this thesis, excluding the manuscript, was written solely by Stefan E. Spirig, with English corrections by Patrick King. All figures not included in the manuscript were created by Stefan E. Spirig with BioRender.com.

## 5 Manuscript

### Cell type-focused compound screen in human organoids reveals molecules and pathways controlling cone photoreceptor death

Stefan E. Spirig<sup>1,2</sup>, Valeria J. Arteaga-Moreta<sup>1</sup>, Zoltan Raics<sup>1</sup>, Susana Posada-Céspedes<sup>1</sup>, Stephanie Chreng<sup>3</sup>, Olaf Galuba<sup>3</sup>, Inga Galuba<sup>3</sup>, Isabelle Claerr<sup>3</sup>, Steffen Renner<sup>3</sup>, P. Timo Kleindienst<sup>1</sup>, Adrienn Volak<sup>1</sup>, Jannick Imbach<sup>1</sup>, Svitlana Malysheva<sup>1,4</sup>, Rebecca A. Siwicki<sup>1</sup>, Vincent Hahaut<sup>1</sup>, Yanyan Hou<sup>1</sup>, Simone Picelli<sup>1</sup>, Marco Cattaneo<sup>1,5</sup>, Josephine Jüttner<sup>1</sup>, Cameron S. Cowan<sup>1</sup>, Myriam Duckely<sup>3</sup>, Daniel K. Baeschlin<sup>3</sup>, Magdalena Renner<sup>1</sup>, Vincent Unterreiner<sup>3</sup>, Botond Roska<sup>1,2,&</sup>

<sup>1</sup>*Institute of Molecular and Clinical Ophthalmology Basel, 4031 Basel, Switzerland*

<sup>2</sup>*Department of Ophthalmology, University of Basel, 4031 Basel, Switzerland*

<sup>3</sup>*Novartis Biomedical Research, 4056 Basel, Switzerland*

<sup>4</sup>*Biozentrum, University of Basel, 4056 Basel, Switzerland*

<sup>5</sup>*Department of Clinical Research, University of Basel, 4031 Basel, Switzerland*

<sup>&</sup>*Corresponding author. Email: botond.roska@iob.ch.*

## **SUMMARY**

**Human organoids that mirror their corresponding organs in cell-type diversity present an opportunity to perform large-scale screens for compounds that protect disease-affected or damage healthy cell types. However, such screens have not yet been performed. Here, we generated 20,000 human retinal organoids with GFP-labeled cone photoreceptors. Since degeneration of cones is a leading cause of blindness, we induced cone death and screened 2,707 compounds with known targets, for those that saved cones or those that further damaged cones. We identified kinase inhibitors that protected cones in both the short and longer term, HSP90 inhibitors that saved cones in the short term but damaged them in the longer term, and broad HDAC inhibition by many compounds that significantly damaged cones. This resource provides a database for cone-damaging compounds, and it describes compounds that can be starting points to develop neuroprotection for cones in diseases such as macular degeneration.**

## **KEYWORDS**

Human organoid, compound screen, retinal organoid, photoreceptor, rod, cone, cone degeneration, rod degeneration, retinitis pigmentosa, age-related macular degeneration, macular degeneration, neuroprotection, glucose starvation, selective vulnerability, mode of action library, kinase inhibitor, HDAC inhibition, HSP90 inhibition

## INTRODUCTION

Human organoids are three-dimensional (3D) cellular assemblies grown from stem cells. They mimic the cellular architecture, cell-type diversity, and in some cases, the functionality of their corresponding organs<sup>1,2</sup>. A wide range of organoids have been generated that model organs such as the brain, retina, thyroid, heart, vasculature, lung, liver, gastrointestinal tract, pancreas, kidney, female reproductive tract, placenta, prostate, and testis<sup>3-6</sup>. These organoids, derived from both healthy and disease-affected individuals, serve multiple purposes such as unraveling the fundamental biology of organ development and deciphering the mechanisms of genetic diseases<sup>2</sup>.

Two other potential uses of human organoids are to screen for compounds that can improve or reverse a disease phenotype<sup>7,8</sup> and, in toxicology, to screen for compounds with potential side effects on specific organs<sup>9</sup>. These two objectives rely on efficient and large-scale production of human organoids, as well as the comprehensive recording and analysis of phenotypic changes within 3D tissues. Noteworthy progress has been made in screening for compounds using mouse intestinal organoids<sup>10</sup> and dissociated cells from mouse retinal organoids<sup>11</sup>, contributing to our understanding of organ biology and allowing for potential therapy development. However, therapies developed in mice do not always translate to humans due to variation in cell types and molecular pathways between the two species<sup>12-14</sup>. Screening of compounds in human organoids has only been done on a small scale, using fewer than sixty compounds and has been limited to cancer organoids<sup>7,8</sup>. Large-scale screening in human organoids for compounds that can alleviate disease phenotypes or cause harmful side effects, has not been described.

The brain, including the retina, is composed of numerous cell types<sup>15-17</sup> and a fundamental characteristic of brain diseases is ‘selective vulnerability’, where the pathology predominantly affects specific cell types<sup>18</sup>. For instance, in Parkinson's disease, the motor symptoms are primarily caused by targeted loss of dopaminergic neurons in the ventral substantia nigra pars compacta<sup>19</sup>. Similarly, in Huntington's disease, medium spiny GABAergic neurons in the striatum are particularly affected<sup>20</sup>. Given the selective vulnerability of specific cell types in various brain diseases, compound screening to find drugs that mitigate disease phenotypes in brain or retinal

organoids will be most effective when they focus specifically on the cell types affected by the disease.

The human retina is part of the brain<sup>21</sup> and contains diverse cell types arranged in five layers<sup>22-24</sup>. Photoreceptors sense light and transmit information to about ten different types of bipolar cells. In turn, the bipolar cells further transmit visual information to an even greater variety of ganglion cells. Ganglion cells are the output neurons of the retina, with their axons forming the optic nerve through which information is broadcast to the rest of the brain. The transmission of information from photoreceptors to bipolar cells is influenced by horizontal cells, while transmission from bipolar cells to ganglion cells is modulated by a multitude of amacrine cell types<sup>21</sup>.

Photoreceptors in the retina are of two types: rods and cones. Rods are utilized in low-light conditions, such as at dusk, and lack of rod function results only in mild or no vision impairment<sup>25</sup>. Cones are primarily responsible for image formation in daylight and enable the high-resolution vision that allows reading and face recognition. The loss of cones or their functionality, mainly due to age-related macular degeneration or end-stage retinitis pigmentosa, results in blindness and affects over 200 million individuals worldwide<sup>26,27</sup>. In age-related macular degeneration, the dysfunction or death of cones is either a direct consequence of the disease or secondary to the dysfunction of the retinal pigment epithelium<sup>28</sup>. Retinitis pigmentosa, a group of monogenic retinal diseases, primarily affects rods<sup>29,30</sup> and cones degenerate as a secondary consequence of rod death<sup>31</sup>. The reasons behind cone degeneration in age-related macular degeneration and retinitis pigmentosa are extensively studied but are not fully understood, and several approaches are being developed to halt the degeneration process<sup>32-49</sup>. However, slowing down cone degeneration in patients has so far not been achieved. Given the critical importance of cones for human vision, preserving their viability remains a significant objective in medicine.

Retinal organoids were among the earliest organoids to be established<sup>50,51</sup>. Since then, the technology for developing human retinal organoids has advanced rapidly and allows for the generation of complex, five-layered organoids that are light sensitive and consist of multiple cell types resembling those found in the adult human retina<sup>52,22,53</sup>. Cones in human retinal organoids

exhibit a close similarity to their counterparts in the adult human retina in terms of gene expression, morphology, and function<sup>22,53</sup> and, thus, present a unique opportunity to study cone degeneration.

Here, we aimed to find compounds that either slow down or induce the death of cones. Compounds that can preserve cones in organoids may pave the way for therapies that mitigate cone loss in conditions such as macular degeneration and retinitis pigmentosa. Compounds that induce cone death and their targets can be valuable for assessing the safety of new compounds planned for clinical trials. We produced ~20,000 human retinal organoids each 30 weeks old, which is a time when organoid cone transcriptomes are similar to those of adult human retina<sup>22</sup>. We targeted GFP expression specifically to cones using adeno associated viral vectors (AAVs) carrying a cone-specific promoter<sup>14</sup> and then induced cone death by glucose starvation. We conducted 3D imaging of the organoids before and after the starvation process, at a time when approximately 40% of cones were lost. We then evaluated a library of 2,707 compounds with known targets<sup>54</sup>. This screening identified compounds that exacerbated cone death as well as compounds that counteracted the degeneration induced by glucose starvation. Analysis of the targets of the compounds revealed that broad inhibition of class I or II histone deacetylases (HDACs I/II) by various compounds resulted in significant damage to cone photoreceptors. Heat shock protein 90 (HSP90) inhibition countered cone degeneration for a few days but proved detrimental after a week. Remarkably, we also discovered two kinase inhibitors that consistently preserved cones over a prolonged period. One of these compounds also preserved rods. Through RNA sequencing of separately sorted organoid cones and rods, we showed that one of the cone-saving kinase inhibitors caused minor but cell type-specific changes in the transcriptomes of cones and rods, while HSP90 inhibition led to changes in the expression of hundreds of genes in both cones and rods. Taken together, we describe here a technology to perform cell type-focused screening in human organoids, and a publicly available resource of 2,707 compounds and their targets, together with their positive or negative effects on human cone survival (<https://ConeTargetedCompoundScreen.iob.ch>). Furthermore, we identify two kinase inhibitors that could be starting points to develop medicine that counters cone degeneration.

## RESULTS

### *Specific and rapid live-labeling of cones in human retinal organoids*

We modified the Agarose Multiwell Array Seeding and Scraping (AMASS) method<sup>22</sup> to generate ~20,000 five-layered human retinal organoids that were grown for 30 weeks (Figures 1A, 1B). These organoids contain the major cell classes and various cell types found in the human retina<sup>22</sup> (Figure S1). They also exhibit functional cone photoreceptors with light-sensitive outer segments<sup>22,53</sup>, inner segments, cell bodies, and axons. Moreover, the transcriptomic profile of the cones in the organoids resembles that of adult human cones<sup>22</sup>.

To visualize living cones, we transduced organoids with AAVs expressing GFP under control of the cone-specific promoter ProA7<sup>14</sup> (Figure 1C and 1D). We tested five different capsid variants and found that AAVs with the AAV9-PHP.eB capsid<sup>55</sup> provided the highest number of labeled cones within four weeks. The cone labeling specificity in organoids was 97±1% (n=5), while the efficacy was 64±8% (n=5) (Figure 1E). We performed AAV transduction in cell culture flasks that allowed simultaneous labelling of ~130 organoids, which were subsequently positioned into 96-well plates for 3D imaging (Figure 1F). As a result, we achieved GFP labeling of cones in a large number of organoids with high specificity, efficacy and uniformity.

### *Glucose starvation induces cone death*

To induce cone death, we cultured organoids individually in 96-well plates using low glucose medium<sup>56</sup>. We recorded cell death by monitoring the disappearance of cytosolic GFP as a reliable and rapid indicator of cell death<sup>57-59</sup>. This was realized by 3D confocal imaging of GFP in each well of the 96-well plate. The organoids were imaged for two weeks without a change of the medium to avoid any displacement of the organoids. Additionally, we included organoids in normal glucose medium in the same 96-well plate as controls (Figure 1G).

We developed three different cell-counting algorithms to determine the number of cones in each organoid (Figure 1G). The first (referred to as '3D-additive-count') quantifies cones image-by-image from a 3D confocal image stack. The second ('3D-count') counts cones from the entire 3D stack. The third ('MIP-count') counts cones from the maximum intensity projection of the 3D stack.

While the primary measure of cone numbers was based on the 3D-additive-count, we also verified the results using the 3D-count and MIP-count methods.

We measured glucose concentration in the low and normal glucose media during organoid imaging without exchanging the media. Initially, glucose levels in the low glucose medium were 9% of those in the normal glucose medium. With time, glucose levels decreased in both the low and the normal glucose media, becoming undetectable after two days in the low glucose medium and seven days in the normal glucose medium (Figure S1).

Next, we examined number of cones over the two-week period in both types of media. In the low glucose medium, the organoids began losing cones after two days of starvation, and this cone loss continued over the two weeks. Conversely, cone numbers in the control organoids in normal glucose medium remained constant until day seven, after which they declined (Figures 1G, 1H, and S1). Therefore, we conducted further experiments for a duration of seven days. Within this time frame, the glucose-deprived organoids lost ~40% of their cones, leading to a significant difference in cone numbers in the low and normal glucose conditions (low glucose, n=26; normal glucose, n=6,  $p < 0.001$ , Mann–Whitney U test, Figure 1H). Cone cell death occurred predominantly in the central region of the organoid rather than at the edges (Figure 1G). This spatial variation is likely attributable to the additional stress experienced by cells in contact with the bottom of the well. The finding that about half of the cones were lost and half survived at the end of seven days in the low glucose medium enabled us to screen for compounds that slow down cone death as well as those that accelerate it.

We then performed two compound screens. In the primary screen, we tested all compounds at the same concentration of 10  $\mu\text{M}$ . In the secondary screen, we selected compounds based on the results of the primary screen and retested them at multiple concentrations.



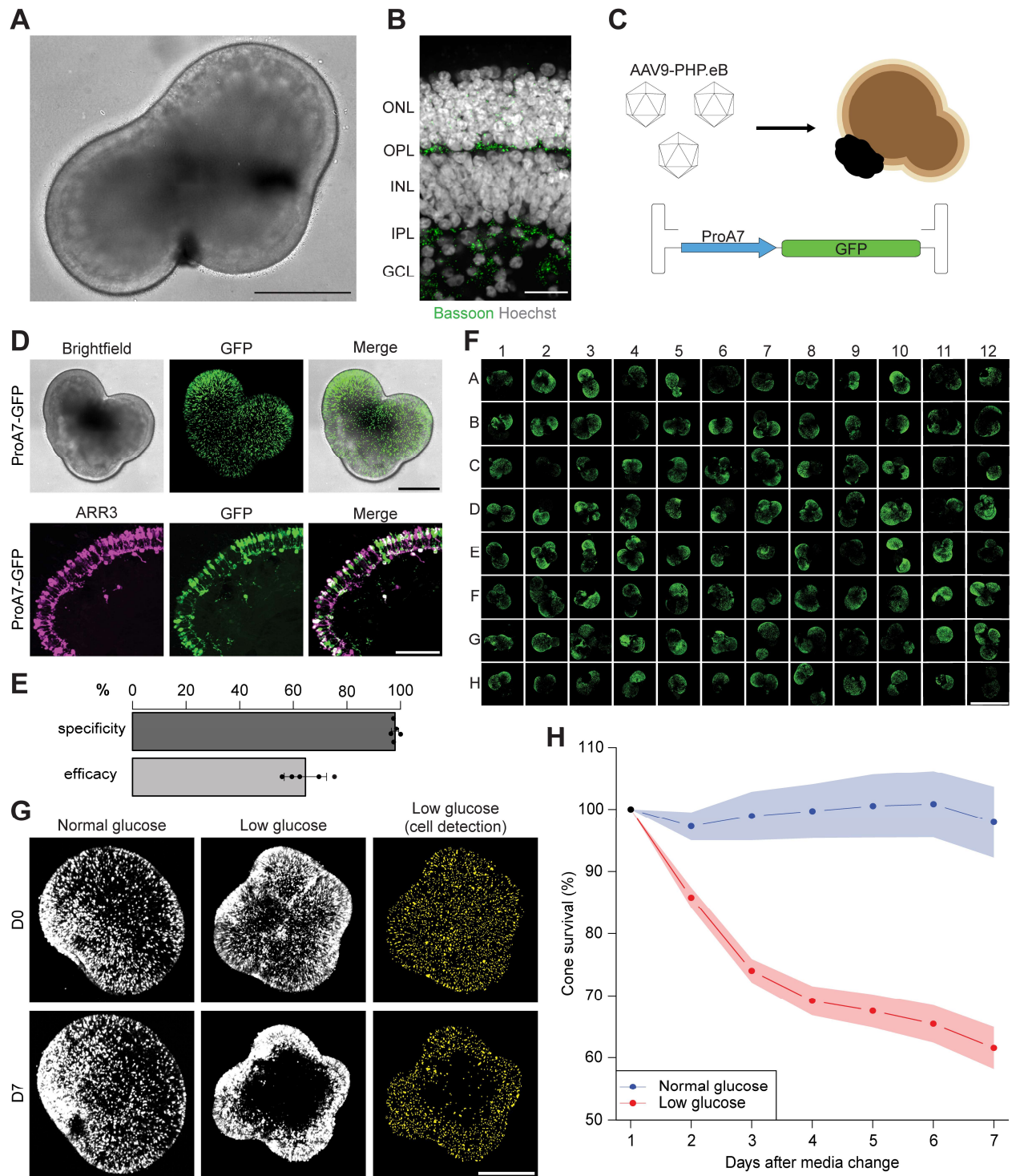


**Figure 1: Glucose starvation induces rapid death of cones in human retinal organoids.**

**A:** Brightfield live image of a human retinal organoid (scale bar, 500  $\mu\text{m}$ ). **B:** Confocal image of a sectioned and stained human retinal organoid (scale bar, 25  $\mu\text{m}$ ). Bassoon, green; Hoechst, white. ONL: outer nuclear layer, OPL: outer plexiform layer, INL: inner nuclear layer, IPL: inner plexiform layer, GCL: ganglion cell layer. **C:** Schematic illustrating the transduction strategy for

organoids. **D:** Top: live images of a ProA7-GFP AAV-transduced human retinal organoid (scale bar, 500  $\mu\text{m}$ ). Bottom: confocal image of a sectioned and stained ProA7-GFP AAV-transduced human retinal organoid (scale bar, 100  $\mu\text{m}$ ). ARR3, magenta; GFP, green. **E:** Quantification of the specificity and efficacy of cone labeling by ProA7-GFP AAV. Results are shown as mean  $\pm$  sd. **F:** Representative image of a 96-well plate containing ProA7-GFP AAV-transduced human retinal organoids (scale bar, 2 mm). **G:** Left: representative live images of human retinal organoids at day 0 (D0) and day 7 (D7) in either normal or low glucose medium. Right: detected cones in organoids in low glucose. GFP, white. Detected cells, yellow. **H:** Quantification of cone survival in human retinal organoid in both normal and low glucose conditions over seven days. The quantification was performed using the 3D-additive-count algorithm. The results are shown as mean  $\pm$  se.

### ***Primary compound screen***

In the primary screen, we used  $\sim$ 15,000 organoids distributed across 175 separate 96-well plates. Each 96-well plate included eight control wells, consistently positioned. Four of these control wells contained organoids in normal glucose medium with dimethyl sulfoxide (DMSO, 0.1%) but no compounds. The other four contained organoids in low glucose medium (DMSO, 0.1%) without compounds. Each remaining individual well (88 wells) within a 96-well plate contained a unique compound, and each compound was present in five different plates, resulting in five replicates of each compound in the screen (Figure 2A). All compounds were stored in DMSO as the solvent. Although the compounds were stored in 384-well plates, we conducted the screening in 96-well plates because the human retinal organoids were too large to be cultured in 384-well plates.

In preparation for the screen, we transferred compounds from a 384-well plate to their designated locations on 96-well plates and then dissolved them in low glucose medium. To initiate the screen, we first moved organoids from flasks containing normal glucose medium to 96-well plates and washed them there in low glucose medium. We then removed the low glucose medium from the 96-well plates containing the organoids and added the compounds dissolved in low glucose medium. We conducted a 3D confocal scan of organoids with GFP-labeled cones in each well of the 96-well plates at the beginning of the screen and again at the end, seven days later. We then used the three algorithms to quantify the number of cones at day zero (D0) and day seven (D7), defining the ratio of counts at D7 and D0 as the measure of cone survival (Figure 2A).

We screened a compound library of 2,707 compounds for their impact on cone survival upon glucose deprivation. The compound library, called ‘Mode of Action library’ (MOA library)

contained compounds with known protein targets<sup>54</sup>. Some compounds had multiple targets, while others had only one (Figure 2B). Similarly, certain targets were affected by multiple compounds, while others were affected by only one compound (Figure 2C). The MOA library had a total of 1,662 targets that are involved in a wide range of biological processes (Figure 2D).

To exclude accidentally empty wells or organoids with little or no labeled cones, we applied a threshold on the D0 cone count and removed wells with lower D0 counts from the dataset (Figure S2). This was necessary since the ratio of D7 and D0 counts is sensitive to low D0 counts. Furthermore, we observed that the survival of cones was determined not only by the compounds but also by the initial cone count. There was a log-linear relationship between the D0 count and cone survival at D7 in low glucose ( $n=14,529$ ,  $R^2=0.12$ ,  $p<0.001$ , 3D-additive-count) with all three cell-counting algorithms (Figures 2E and S2). To account for this relationship, we adjusted the values of cone survival using a linear transformation yielding the quantity ‘adjusted cone survival’. Adjusted cone survival therefore does not depend on the cone count at D0.

The locations of organoids on the 96-well plates did not influence cone survival: the mean adjusted survival at all positions (8.8% maximum difference between positions) remained within one standard deviation of that of the position exhibiting the least variation (12.9%), excluding the normal glucose well positions (Figure S2).

To investigate additional potential batch effects in the screen, we examined the distribution of the mean adjusted cone survival of the eight control organoids: four in normal and four in low glucose; first across the 175 separate 96-well plates (Figures 2F and S2), second across the 35 experiments, each consisting of five 96-well plates with the same compound (Figure S2), and third, across the six independent organoid productions used for the primary screen (Figures 2G and S2). We found no major differences between batches at any level. The mean adjusted cone survival of normal and low glucose control organoids was significantly different across all 35 experiments and across all six organoid productions, using all three cell-counting algorithms ( $p$ -values $<0.001$ , Mann–Whitney U test, Figures 2G-H and S2). Cone survival values showed strong and significant correlations across the three cell counting algorithms ( $R=0.92-0.97$ ,  $p$ -values $<0.001$ , Pearson

correlation, Figure S3), suggesting that the quantification of cone survival is robust across the different algorithms.

After accounting for potential confounding variables and batch effects, we proceeded to analyze the outcome of the primary screen. The mean adjusted cone survival of most compounds was not significantly different from the mean adjusted cone survival of the low glucose control. However, one set of compounds significantly impacted cone survival negatively ('cone-damaging compounds',  $p$ -values $<0.05$ , ANCOVA with Benjamini Hochberg correction for multiple testing), while another set of compounds showed a beneficial effect on cone survival ('cone-saving compounds') (Figure 2I, and S3).

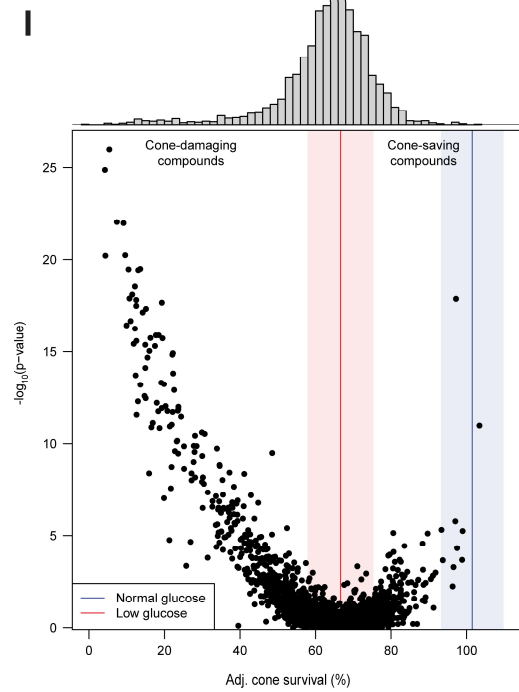
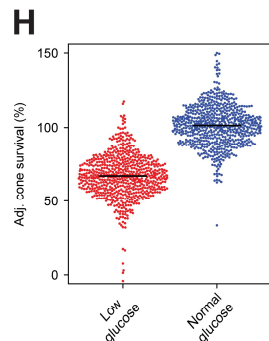
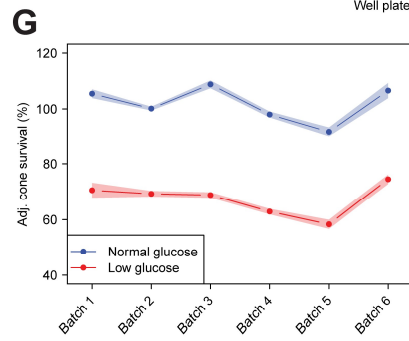
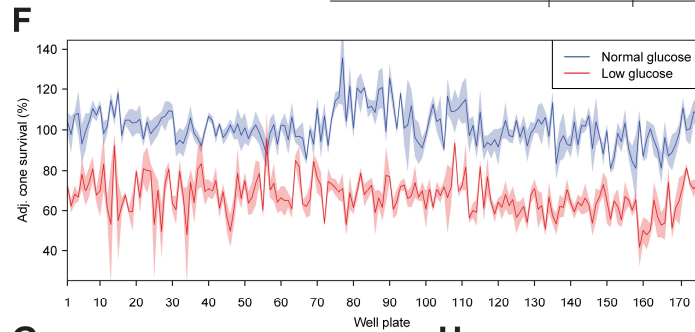
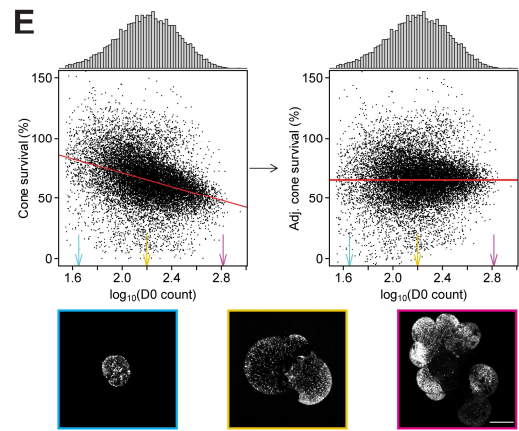
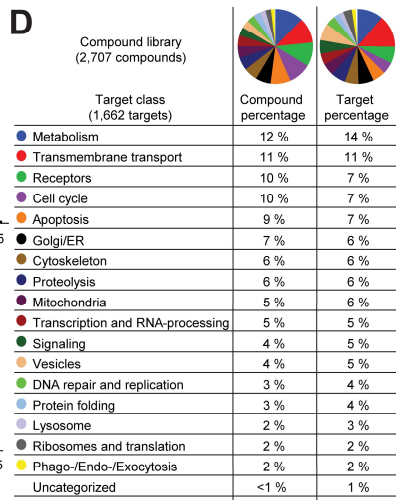
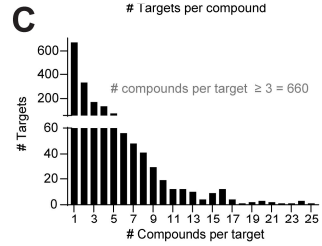
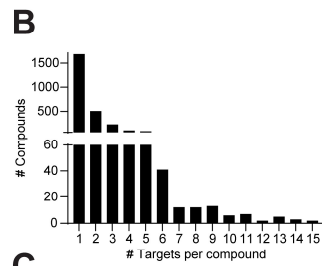
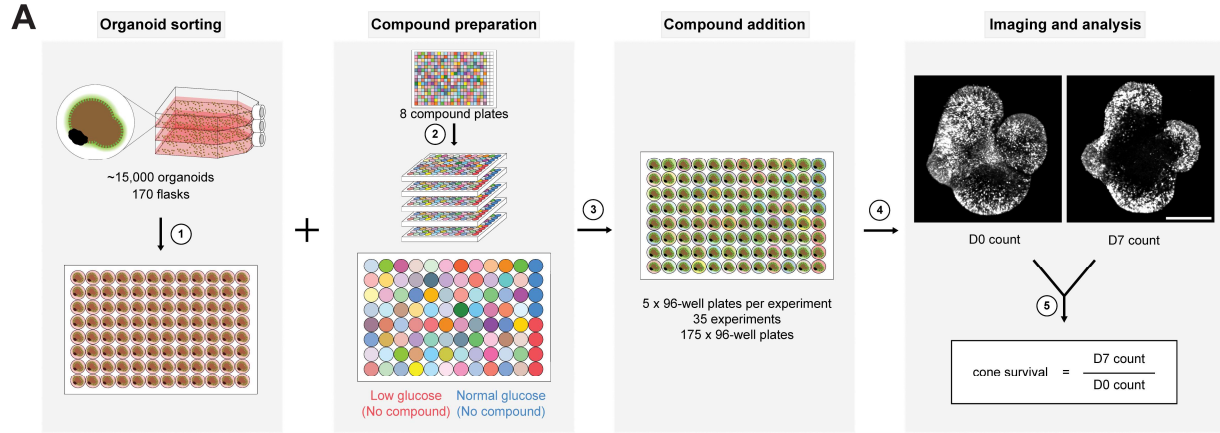


**Figure 2: Primary screen of compounds that damage or save cones.**

**A:** Schematic illustration of the primary screen. 1. Transfer of human retinal organoids from cell culture flasks to 96-well plates. 2. Compound distribution from 384- to 96-well plates with five replicates of each compound. Low glucose controls, red. Normal glucose controls, blue. 3. Addition of compounds to human retinal organoids. 4. Human retinal organoid imaging. 5. Quantification of cones from the same human retinal organoid at D0 and D7. GFP, white. **B:** Bar chart showing the number of compounds with a given number of targets. **C:** Bar chart showing the number of targets with a given number of compounds per target. **D:** Categorization of targets and compounds of the compound library. **E:** Dependence of cone survival on the D0 cone count. Top left: cone survival as a function of the logarithm of the cone count at D0, with a fitted linear model; the regression line is shown in red. The distribution of D0 counts is shown above. Top right: adjusted cone survival as a function of the logarithm of the cone count at D0 with the transformed regression line in red. The distribution of D0 counts is shown above. Bottom: example images with different D0 cone counts (scale bar, 500  $\mu\text{m}$ ). Colored arrows and frames around images indicate corresponding D0 cone counts. GFP, white. **F-G:** Adjusted cone survival of normal and low glucose controls for individual well plates (**F**) and organoid batches (**G**) using the 3D-additive-count algorithm, mean  $\pm$  se. **H:** Adjusted cone survival of all normal and low glucose control human retinal organoids. **I:** Effect of compounds on cone survival in the primary screen. Each dot corresponds to the effect of one compound, with the median of the adjusted cone survival of five human retinal organoids on the x-axis and the p-value comparing the cone survival between the compound and the low glucose controls on the y-axis. The median (line) and the interquartile range (shaded area) of normal (blue) and low (red) glucose controls are indicated. Top: the distribution of median adjusted cone survival for compounds. Results were obtained using the 3D-additive-count algorithm.

**Secondary screen: cone-damaging compounds**

In order to validate the cone-damaging and cone-saving compounds detected in the primary screen and to assess the concentration dependence of their actions, we proceeded to secondary screens.

First, we revisited the 33 most damaging compounds selected from a set of 146 compounds that caused significant damage beyond that induced by the low glucose medium in the primary screen ( $n=5$  for each compound,  $p\text{-values}<0.05$ , ANCOVA with Benjamini Hochberg correction for multiple testing, Table S1). We investigated these compounds at four concentrations (0.01, 0.1, 1, 10  $\mu\text{M}$ ) in five replicates using normal glucose medium. We used normal glucose medium to confirm the damaging effects of these compounds on cones of healthy organoids. Furthermore, each 96-well plate included four wells with only DMSO in normal glucose medium, serving as a negative control (Figure 3A). As for the positive control, we utilized Staurosporine, a nonselective ATP-competitive kinase inhibitor known for inducing apoptosis<sup>60,61</sup>. This was tested also in five replicates at each of the four concentrations.

Most compounds (29 out of 33) again induced a significant decrease in the number of cones compared to the negative control (n=5 for each compound and concentration, minimum p-value<0.05, ANOVA with Benjamini Hochberg correction for multiple testing, Figure 3B). Of these compounds, nine caused a more significant decrease in cone numbers than the positive control Staurosporine, which reduced cone numbers by 76%. The remaining compounds had effect sizes of at least 38% (Figures 3B, S4, and S5, Table S2).

We observed a variety of dose-response curves for cone-damaging compounds used in the secondary screen that could be clustered into four groups. The first cluster included compounds that led to cone death only at the highest concentration (10  $\mu$ M), such as an ITK kinase inhibitor and a Beta catenin inhibitor. The second cluster of curves had an action threshold of 1  $\mu$ M and included a BCL2L1 inhibitor, an AP-1 inhibitor, an immunoproteasome inhibitor, and an AAA ATPase p97 inhibitor. The third cluster of curves had an action threshold of 0.1  $\mu$ M, for example a sodium ionophore had such a curve. For the fourth cluster of curves, cone death increased linearly with the logarithm of compound concentration. Most of these curves belonged to HDAC I/II inhibitors (Figures 3C, 3D and S5).

Of the 146 compounds that caused significant damage to cones in the primary screen (p-values<0.05, ANCOVA with Benjamini Hochberg correction for multiple testing), 19 were identified as HDAC I/II inhibitors (Figure 3E and Table S1). Furthermore, in the secondary screen, seven of the 28 compounds that significantly damaged cones were HDAC I/II inhibitors (Figures 3B and S4). To determine whether this high number of HDAC I/II inhibitors is a result of bias in the MOA library towards HDAC I/II inhibitors or whether HDAC I/II inhibitors tend to damage cones more frequently, we reanalyzed the results of the primary screen. We calculated the probability that the mean adjusted cone survival for a randomly selected set of 45 compounds is lower than the mean adjusted cone survival for the 45 different HDAC I/II inhibitors in the MOA library. This probability was smaller than 0.0001, implying that, on average, the 45 HDAC I/II inhibitors in the MOA library cause more damage to cones than a random selection of the same number of other compounds.

To systematically investigate whether modulating any specific target is significantly more harmful to cones than modulating other targets, we first selected targets that had a minimum of three compounds listed in the MOA library. We identified a total of 660 such targets (Figure 2C). Next, we calculated the probability of observing a lower mean adjusted cone survival when randomly selecting the same number of compounds, in comparison to the compounds associated with the target. We identified 10 targets with a p-value of less than 0.0001 and less than 0.05 after Benjamini Hochberg correction for multiple testing. These targets belonged exclusively to class I/II HDACs (Figure 3F). Furthermore, when evaluating the percentage of compounds that led to significant cone damage among all compounds targeting each specific target, HDACs had the highest values (Figure S4). Each HDAC I/II target was associated with 9-29 distinct compounds, out of which 44-67% induced significant damage to cones. Interestingly, compounds that acted on Sirtuins, which are class III HDACs, had no influence on cone survival (Figures 3E, 3F and S4). HDAC I/II inhibitors often affect multiple HDAC I/II targets and we found a significant negative correlation between the number of HDAC I/II targets of a specific inhibitor and adjusted cone survival ( $p < 0.001$ ,  $R = -0.6$ , Spearman correlation). Therefore, cones are specifically sensitive to HDAC I/II inhibition, and HDAC I/II inhibitors with a wide range of targets are more likely to result in cone damage than those that are more selective (Figures 3G and 3H).

Cones were also highly sensitive to the inhibition of tubulins (Figures 3E, 3F and S4). The probability that the mean adjusted cone survival for a random set of 10 compounds was lower than that of the 10 distinct tubulin inhibitors in the MOA library was 0.002. Of the 10 tubulin-targeting compounds, four resulted in a significant decrease in cone numbers. Notably, three of these compounds had a broad target range, affecting 19-20 different tubulins.



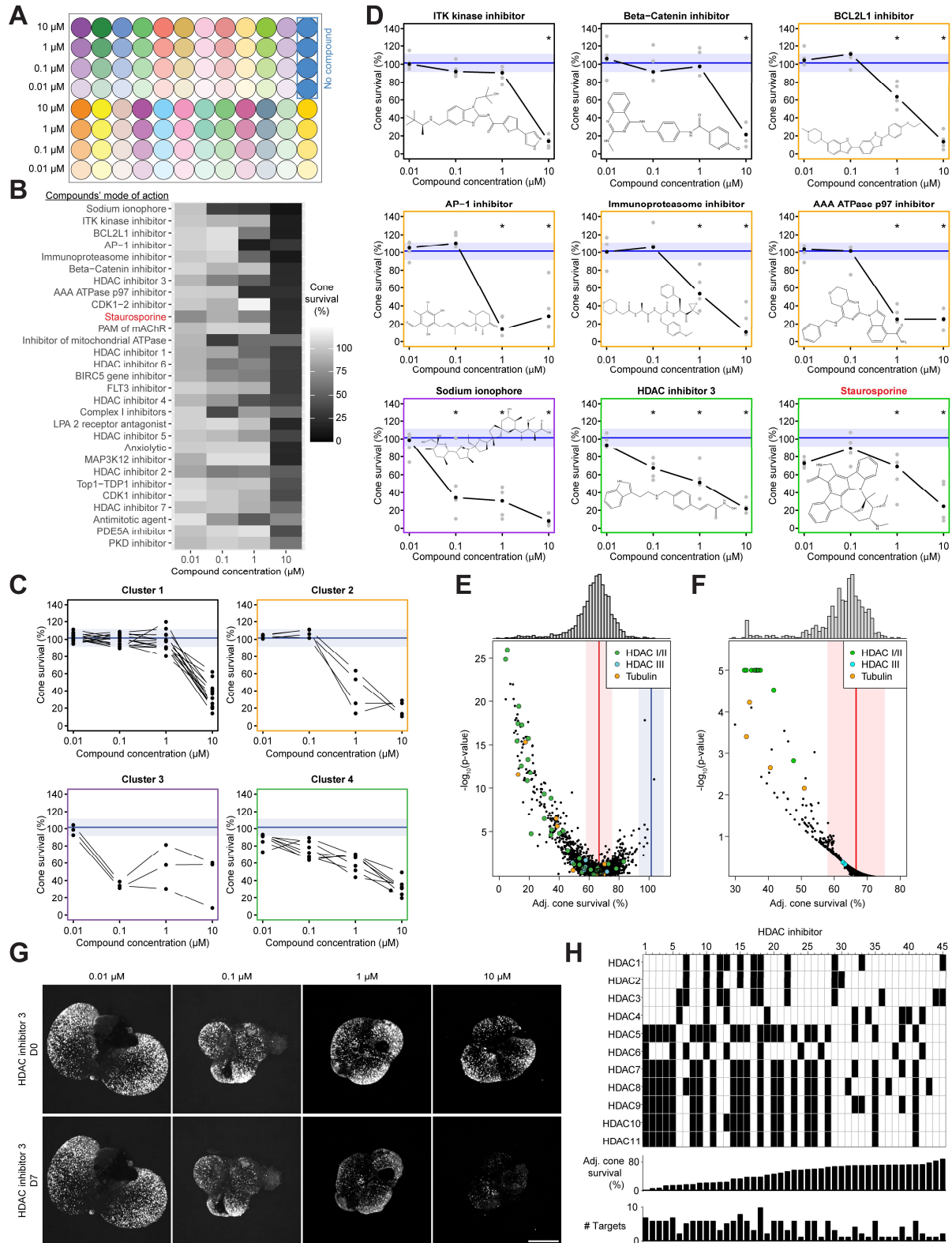


**Figure 3: Secondary screen of cone-damaging compounds.**

**A:** Schematic illustration of the plate layout in the secondary screen for cone-damaging compounds. Different colors represent distinct compounds. No compound control, blue. **B:** Summary of compound effects for significant cone-damaging compounds ( $p < 0.05$  for at least one concentration after Benjamini Hochberg correction for multiple testing). The positive control Staurosporine is indicated in red. Compounds are ordered by minimum p-value per concentration, with the smallest p-value at the top. **C:** Dose-responses for significant compounds within the same cluster. Dots represent the median of cone survival at the indicated concentrations. The median (line) and the interquartile range (shaded area) of normal (blue) glucose controls are indicated. **D:** Dose-response curves of eight compounds with the lowest p-values (at any concentration) and Staurosporine (red) with their corresponding cluster indicated. The median and the interquartile range are labeled as in (C). The colored frame indicates the corresponding cluster from (C). The structure of each compound is shown in the plot. Significant compounds and concentrations are marked with \*, denoting a  $p$ -value  $< 0.05$  (after Benjamini Hochberg correction for multiple testing). **E:** Adjusted cone survival and p-values in the primary screen. HDAC I/II (green), HDAC III (cyan), and tubulin (orange) inhibitors are labeled. The median (line) and the interquartile range (shaded area) of normal (blue) and low (red) glucose controls are indicated. **F:** Target analysis of primary screen. The means of the median adjusted cone survival for each target are shown, along with their p-values. Compound targets are labeled. HDAC I/II, green; HDAC III, cyan; tubulin, orange. The median (line) and the interquartile range (shaded area) of low (red) glucose controls are indicated. **G:** Example images of human retinal organoids before (D0) and after (D7) treatment with different concentrations of HDAC inhibitor 3 (scale bar, 500  $\mu$ m). GFP, white. **H:** Top: different HDAC I/II inhibitors (numbered from 1 to 45) with their targets (black shaded areas). Compounds are sorted from left to right based on median adjusted cone survival. Middle: Adjusted cone survival for each of the 45 compounds. Bottom: Number of HDAC I/II targets of the 45 compounds.

**Secondary screen: cone-saving compounds**

We proceeded with the analysis of the 31 compounds that had the greatest effect in protecting cones during glucose deprivation in the primary screen. These compounds were tested at four different concentrations (0.01, 0.1, 1, and 10  $\mu$ M) in five replicates in low glucose medium. Each 96-well plate included four wells containing only DMSO in normal glucose medium as a positive control, and four wells containing only DMSO in low glucose medium as a negative control (Figure 4A).

We confirmed that four out of the 31 compounds tested in the secondary screen have a significant positive impact on cone survival after correction for multiple testing ( $n=5$  for each compound and concentration, minimum  $p$ -values  $< 0.05$ , ANCOVA with Benjamini Hochberg correction for multiple testing, Figures 4B, 4C, S6, S7 and Table S3). These four compounds include an inhibitor of HSP90AA1 ('HSP90 inhibitor 1'), an inhibitor of both HSP90AA1 and HSP90AB1 ('HSP90 inhibitor 2'), an inhibitor of MTOR, PIK3CA, PIK3CB, and PIK3CD ('MTOR inhibitor 1'), and

an inhibitor of PDGFRA and PDGFRB ('PDGFR inhibitor 1'). The two HSP90 inhibitors demonstrated stronger activity at lower concentrations (0.1 or 1  $\mu$ M) and less activity at a concentration of 10  $\mu$ M (Figure 4B). The dose-response curves of the MTOR inhibitor and the PDGFR inhibitor showed similar patterns, being effective only at the highest concentration of 10  $\mu$ M (Figures 4B and 4C).

To understand the relationship between the four compounds and their targets in the context of cone protection, we re-analyzed the results of the primary screen, focusing on the targets of the four inhibitors that were confirmed to protect cones (HSP90AA1, HSP90AB1, MTOR, PIK3CA, PIK3CB, PIK3CD, PDGFRA, and PDGFRB). We found five compounds in the MOA library that target HSP90AA1, four of which resulted in adjusted cone survival higher than 80% (although some of these were not significant in the primary screen). For all other targets, the percentages of compounds with a positive effect on cone survival were only between 11 and 33% (Figures 4D and S8). These results suggest that HSP90AA1 is the target of HSP90 inhibitors 1 and 2 in cones. Additionally, they suggest that the other two compounds (MTOR inhibitor 1 and PDGFR inhibitor 1), which are both kinase inhibitors, have different causal targets in human cones than those originally listed in the MOA library.

To systematically examine whether modulating particular targets has a greater positive impact on cones compared to other targets, we conducted an analysis focusing on 660 targets that had at least three partner compounds listed in the MOA library. To rank targets in their ability to protect cones, we calculated the probability of observing a higher mean adjusted cone survival in the primary screen when randomly selecting the same number of compounds in comparison to the compounds associated with the target. HSP90AA1 emerged as one of the top-ranked targets ( $p < 0.00001$  and  $p < 0.01$  after Benjamini Hochberg correction for multiple testing). Targets such as HSP90AB1, MTOR, PIK3CA, PIK3CB, PIK3CD, PDGFRA, and PDGFRB were not significant because a large proportion of compounds acting on these targets had no impact on cone survival (Figure 4D, 4E and S8). TP53 was a further significant target ( $p < 0.00001$  and  $p < 0.01$  after Benjamini Hochberg correction for multiple testing), for which there were three compounds in the library, two inhibitors and one expression enhancer. However, both inhibitors and the expression enhancer increased cone

survival in the primary screen, and the enhancer had no significant effect after retesting, suggesting that TP53 is not a target for cone protection.

To further explore the connection between the four validated compounds that protect cones and their targets, we compared available data on IC<sub>50</sub> (the concentration at which a compound shows 50% of its maximum inhibitory effect) with the effect on cone survival of inhibitors of HSP90AA1, HSP90AB1, MTOR, PIK3CA, PIK3CB, PIK3CD, PDGFRA, and PDGFRB. We found a significant negative correlation between the reported IC<sub>50</sub>s and the adjusted cone survival for the inhibitors of HSP90AA1 ( $R=-0.7$ , Spearman correlation,  $p=0.03$ , Figure S8). This suggests that compounds with lower IC<sub>50</sub> values (indicating greater potency) are linked to higher adjusted cone survival. However, the IC<sub>50</sub>s for the inhibitors of HSP90AB1, MTOR, PIK3CA, PIK3CB, PIK3CD, PDGFRA, and PDGFRB were not significantly correlated with cone survival. These findings further confirm that HSP90AA1 is a target that, when inhibited, effectively protects cones from the effects of glucose starvation at day seven. Therefore, we have renamed HSP90 inhibitor 1 as ‘HSP90AA1I-1’ and HSP90 inhibitor 2 as ‘HSP90AA1I-2’. On the other hand, HSP90AB1, MTOR, PIK3CA, PIK3CB, PIK3CD, PDGFRA, and PDGFRB are not causal targets that affect organoid cone survival. Since MTOR inhibitor 1 and PDGFR inhibitor 1 are kinase inhibitors, we renamed them as ‘Cone-Saving Kinase inhibitor 1’ (CS-KI-1), and as ‘Cone-Saving Kinase inhibitor 2’ (CS-KI-2), respectively (Figure 4F).

So far, we investigated the impact of different compounds on the survival of cones over a seven-day period. To understand the dynamics of the action of the compounds and whether some compounds can protect cones over a longer period, we conducted additional tests on the three compounds HSP90AA1I-1, CS-KI-1, and CS-KI-2 over a 14-day period. We administered these compounds in the concentrations that showed the strongest effect during the secondary screen: 1  $\mu$ M for HSP90AA1I-1 and 10  $\mu$ M for CS-KI-1 and CS-KI-2 (Figure 4B). We treated organoids with these compounds in low glucose medium and conducted daily imaging for 14 days. We used both normal glucose and low glucose media with DMSO (without the compounds) as negative and positive controls, respectively (Figures 4G-I).

HSP90AA1I-1 showed significant and almost complete protection of cones from death in the first seven days but became detrimental to cones after 10 days. The adjusted cone survival in the presence of HSP90AA1I-1 after 10 days was significantly lower than the low glucose control (low glucose, n=12; HSP90AA1I-1, n=9,  $p < 0.001$ , Mann–Whitney U test, Figure 4G). In contrast, CS-KI-1 and CS-KI-2 had minimal impact on cone survival during the first few days but, as time progressed, they started to show a significant positive effect on cone survival compared to the low glucose control, and this effect persisted until the end of the 14-day experiment (low glucose, n=12; CS-KI-1, n=9,  $p = 0.001$ ; CS-KI-2, n=9,  $p = 0.01$ , Mann–Whitney U test, Figures 4H and 4I). These findings suggest that HSP90AA1 inhibition is detrimental to cone survival in the long term and that the protective effect of CS-KI-1 and CS-KI-2 on cones is of long duration.

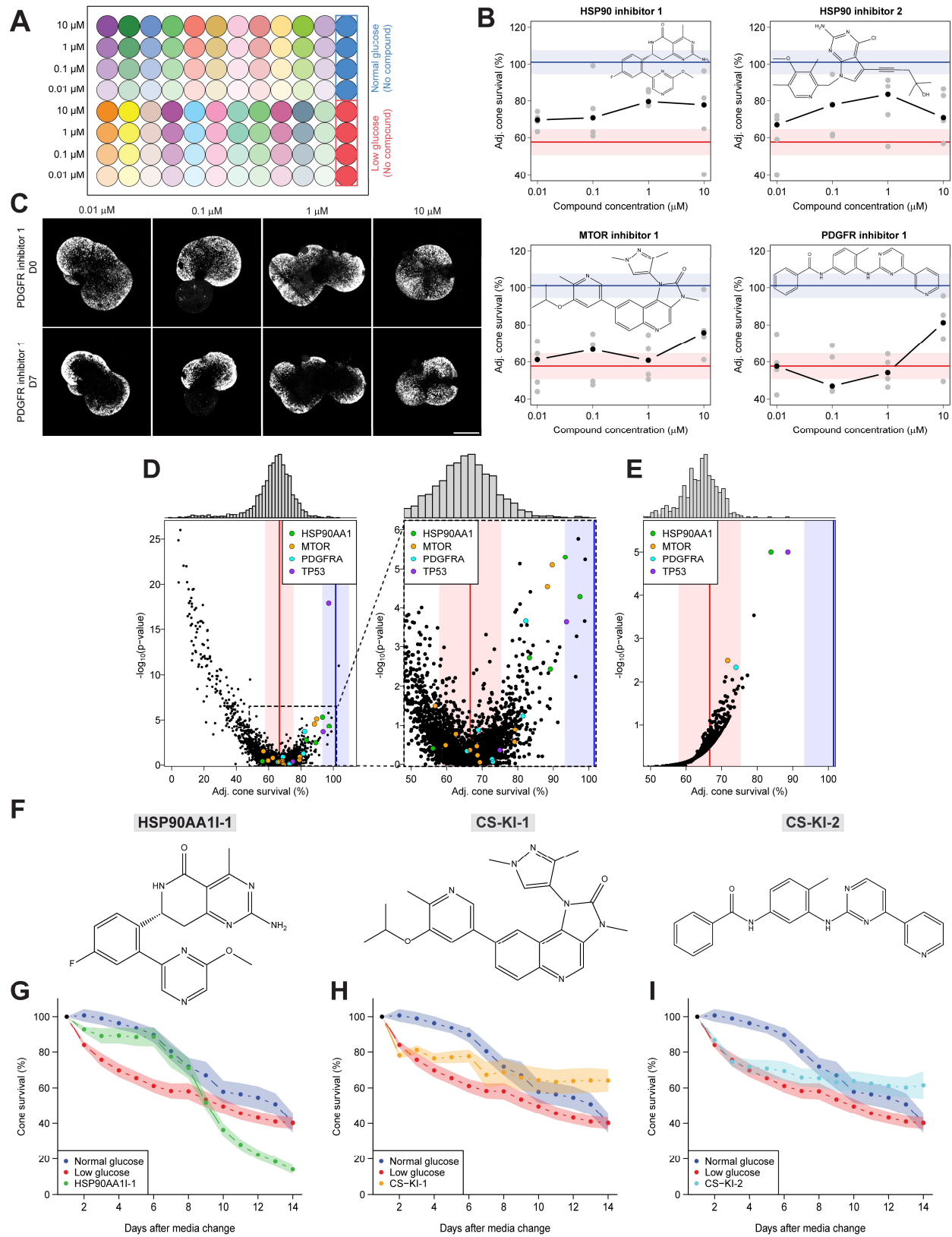


**Figure 4: Secondary screen of cone-saving compounds.**

**A:** Schematic illustration of plate layout in the secondary screen for cone-saving compounds. Different colors indicate distinct compounds. Low glucose controls, red. Normal glucose controls, blue. **B:** Dose-response curves of the four significant compounds. Black dots, median adjusted cone survival; gray dots, individual adjusted cone survival values. The median (line) and the interquartile range (shaded area) of normal (blue) and low (red) glucose controls are indicated. The structure of each compound is shown in the plot and the annotated target is indicated on top. **C:** Example images of human retinal organoids at D0 and D7 with different concentrations of PDGFR inhibitor 1 (scale bar, 500  $\mu\text{m}$ ). GFP, white. **D:** Left: adjusted cone survival and p-values in the primary screen. Compound targets are labeled. HSP90AA1, green; MTOR, orange; PDGFRA, cyan; TP53, purple. The median and the interquartile range are labeled as in (B). Right: Zoom-in of plot on the left. **E:** Target analysis of the primary screen. The means of the median adjusted cone survivals for each target are shown, along with their p-values. HSP90AA1, green; MTOR, orange; PDGFRA, cyan; TP53, purple. The median and the interquartile range are labeled as in (B). **F:** Chemical structures and new names of the indicated compounds. **G-I:** Time course of cone survival in glucose-starved human retinal organoids with the indicated compounds for 14 days. Results are shown as mean  $\pm$  se.

**Effect of HSP90AA1I-1, CS-KI-1, and CS-KI-2 on rod photoreceptor death**

HSP90AA1I-1, CS-KI-1, and CS-KI-2 each had a protective effect on cones after seven days of glucose starvation and we examined whether they would offer a similar protection to rods. To do this, we developed the promoter ProA330, which targeted rods in human retinal organoids. When we introduced AAV9-PHP.eB capsid-coated AAVs that expressed GFP under the control of the ProA330 into human retinal organoids, we observed GFP expression in rods with a specificity of  $98 \pm 3\%$  (n=6) and an efficacy of  $38 \pm 3\%$  (n=6) (Figures 5A and 5B). ProA330 also drove specific expression in rods of mouse retina *in vivo* with a specificity of  $99.7\% \pm 0.5\%$  and an efficacy of  $41 \pm 7\%$  (n=3 retinas, 2 mice, Figure S9).

Similar to cones, the rods also died during glucose starvation, with a survival by day seven of 45% in low glucose and 70% in normal glucose. The number of remaining rods was significantly different in low and normal glucose (low glucose, n=9, normal glucose, n=6,  $p < 0.001$ , Mann–Whitney U test, Figures 5C and 5D). Rod survival dropped further after 14 days to 39 % in low glucose and 61% in normal glucose (low glucose, n=9, normal glucose, n=6,  $p = 0.003$ , Mann–Whitney U test).

Treatment with either 1  $\mu\text{M}$  HSP90AA1I-1, 10  $\mu\text{M}$  CS-KI-1, or 10  $\mu\text{M}$  CS-KI-2 led to an increase in rod survival after seven and 14 days of starvation (Figures 5D). However, this was only

significant for CS-KI-2 (seven days: low glucose, n=9; HSP90AA1I-1, n=9, p=0.1; CS-KI-1, n=9, p=0.3; CS-KI-2, n=9, p=0.01; 14 days: low glucose, n=9; HSP90AA1I-1, n=9, p=0.1; CS-KI-1, n=9, p=0.5; CS-KI-2, n=9, p=0.004, Mann–Whitney U test). In contrast to cones, we did not detect a detrimental effect of HSP90AA1I-1 on rod photoreceptors at any time.

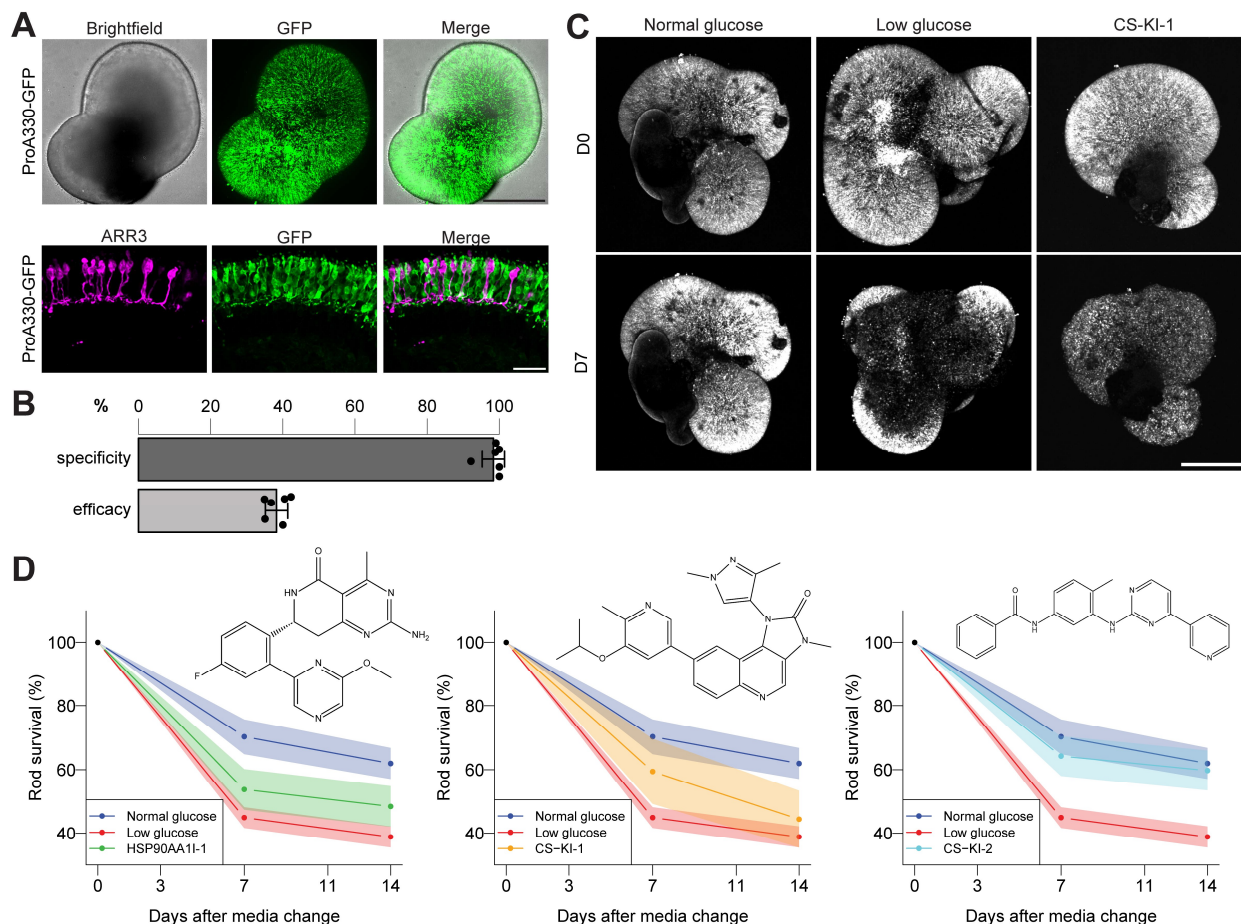


**Figure 5: Effect of cone-saving compounds on rods.**

**A:** ProA330-GFP AAV transduction of human retinal organoids. Top: live image of a ProA330-GFP-transduced human retinal organoid (scale bar, 500  $\mu$ m). Bottom: Confocal image of sectioned and stained transduced human retinal organoid (scale bar, 25  $\mu$ m). Rods were identified as being present in the photoreceptor layer but negative for the cone-marker ARR3. ARR3, magenta; GFP, green. **B:** Quantification of the specificity and efficacy of rod labeling by ProA330-GFP AAV. Results are shown as mean  $\pm$  sd. **C:** Example images of ProA330-GFP AAV-transduced human retinal organoids at D0 and D7 in either normal glucose, low glucose, or low glucose with CS-KI-1. GFP, white. **D-F:** Time course of rod survival in glucose-starved human retinal organoids with the indicated compounds for 14 days. Results are shown as mean  $\pm$  se. Structures of the compounds are shown.



### ***The transcriptomic state of cones and rods in low glucose, HSP90AA1I-1, and CS-KI-1***

A compound that protects cones would be more beneficial if it does not cause a major change in the transcriptomic state of cones. To evaluate this, we studied the transcriptomes of cones and rods in control organoids and in organoids exposed to seven days of glucose starvation in the presence or absence of HSP90AA1I-1 or CS-KI-1. We generated dual color retinal organoids with green-fluorescent cones and red-fluorescent rods by transducing them with AAV9-PHP.eB capsid-coated ProA7-GFP and ProA330-tdTomato AAVs simultaneously (Figure 6A). This allowed us to isolate cones and rods from the same organoids using fluorescence-activated cell sorting. Subsequently, we analyzed their transcriptomes separately using bulk RNA-sequencing (Figure S10).

Cells that were GFP positive expressed marker genes for cones, while tdTomato-positive cells expressed marker genes for rods. This was observed in both the normal and the low-glucose conditions, indicating, on the one hand, the effective isolation of the two cell types and, on the other hand, that the transcriptomic identity of cones and rods was not affected by glucose starvation (Figure 6B).

The annotated target genes of HSP90AA1I-1, namely *HSP90AA1* and *HSP90AB1*, were highly expressed in both cones and rods. Furthermore, when treated with HSP90AA1I-1, the expression of *HSP90AB1* increased significantly in both cones and rods (cones,  $p=0.01$ ; rods,  $p<0.001$ ). Expression of the annotated target genes of CS-KI-1, including *MTOR*, *PIK3CA*, *PIK3CB*, and *PIK3CD*, was low. Moreover, the annotated target genes of CS-KI-2, *PDGFRA* and *PDGFRB*, were not expressed in cones and rods (Figure 6C). These findings further support the notion that HSP90AA1 and HSP90AB1 are targets of HSP90AA1I-1 in cones, while neither PDGFRA nor PDGFRB are targets of CS-KI-2 in cones and rods.

Principal component analysis showed that the transcriptome of cones in low glucose was close to the transcriptome of cones in normal glucose. This was also true for rods. Treatment with HSP90AA1I-1 induced a significant shift in the transcriptomes of both cones and rods ( $p<0.001$ , Wilcoxon Signed-Rank Test, Figure 6D). However, cones treated with CS-KI-1 had transcriptomes similar to untreated cones ( $p=0.4$ , Wilcoxon Signed-Rank Test), while treated rods

differed significantly from untreated rods ( $p < 0.001$ , Wilcoxon Signed-Rank Test, Figure 6D). In agreement with the principal component analysis, we found only a limited number of differentially expressed genes between the normal and low glucose controls: four genes were upregulated and one gene was downregulated in cones when comparing normal glucose to low glucose conditions. Furthermore, only one gene was upregulated in rods (Figure 6E). After treatment with HSP90AA1I-1, 699 genes showed differential expression in cones, with 163 genes upregulated and 536 genes downregulated. In rods, 1200 genes showed differential expression, with 258 upregulated and 942 downregulated (Figure 6E). In the case of CS-KI-1 treatment, only 35 genes showed differential expression in cones, with 27 genes upregulated and 8 genes downregulated. In rods, 107 genes exhibited differential expression, consisting of 7 upregulated and 100 downregulated genes. These results suggest that treatment with HSP90AA1I-1 leads to a major change in the transcriptomes of cones and rods, while the effect of CS-KI-1 is smaller in rods and not significant in cones. Furthermore, CS-KI-1 treatment alters significantly different genes between cones and rods ( $p < 0.001$ , McNemar's test).

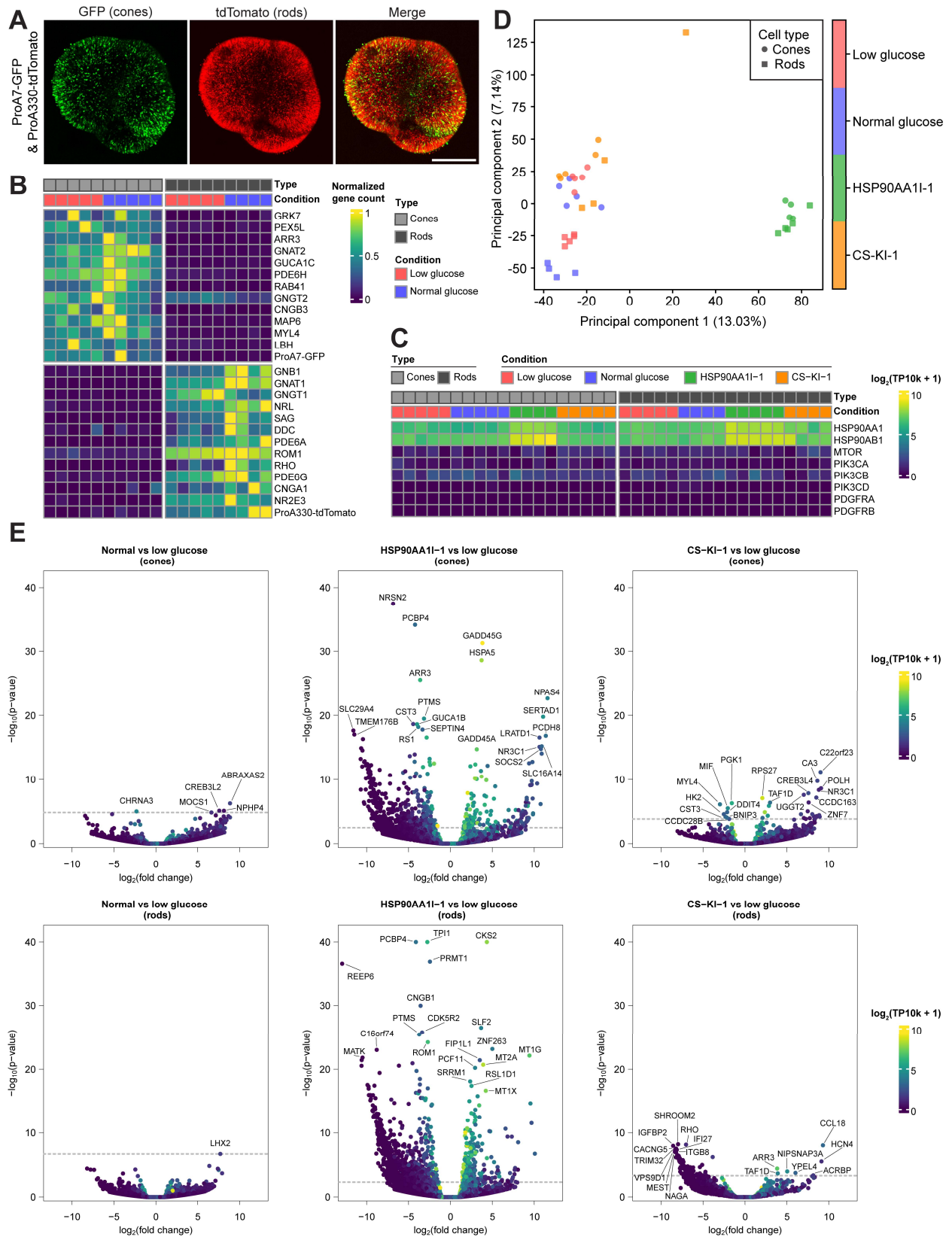


**Figure 6: Transcriptomes of photoreceptors treated with cone-saving compounds.**

**A:** Human retinal organoids transduced with ProA7-GFP (green) and ProA330-tdTomato (red, scale bar, 500  $\mu\text{m}$ ). **B:** Expression of cone (top) and rod (bottom) markers. Heatmap colors correspond to gene expression normalized to the row-wise maximum. Normal and low glucose conditions are indicated at the top. **C:** Expression of genes encoding annotated compound targets. Colors at top indicate cell types and conditions. Color scale indicates gene expression levels. TP10k, transcript counts per 10,000. **D:** Principal component analysis of transcriptomes under the indicated conditions. **E:** Differential gene expression comparing human retinal organoids in normal glucose (left), low glucose with HSP90AA11-1 (middle), or low glucose with CS-KI-1 (right) to human retinal organoids in low glucose for both cones (top) and rods (bottom). Dotted line indicates the significance threshold of  $p < 0.05$  after Benjamini-Hochberg correction for multiple testing. Colors indicate average gene expression. The 10 most significantly up- or down-regulated genes are labeled. TP10k, transcript counts per 10,000.

## DISCUSSION

### *Large-scale compound screen in human organoids*

We have performed a cell type-focused compound screen in  $\sim 20,000$  human organoids using 2,707 compounds with annotated targets. Here we used a modified AMASS method<sup>22</sup> to produce replicable, multilayered human retinal organoids in large quantities. We induced the death of cones by lowering glucose for seven days and monitored cell death by imaging GFP that was expressed specifically in cones. We identified compounds that protected cones, compounds that damaged cones, and compounds that had no effect. The results of the primary screen, including the names and unique identifiers of all the compounds, their annotated targets, and their effect on cone survival are publicly available at <https://ConeTargetedCompoundScreen.iob.ch>.

Among the photoreceptors, we have focused on cones since the dysfunction of cones leads to blindness, while rod dysfunction leads to no or minor visual disabilities<sup>25</sup>. We labeled cones with AAVs carrying a cone-specific promoter<sup>14</sup>. The use of AAVs has the advantage over using organoids with genetically labeled cell types in that the target cell type can be rapidly changed across organoids with the same genetic background. Different genetic backgrounds can lead to variation in the structure and cell-type composition of retinal organoids<sup>22</sup>. AAV-based labeling allowed us to test some of the compounds on rods of organoids grown from the same induced pluripotent cell line, using AAVs carrying a rod-specific promoter.

To find molecules that either protect or damage cones, the screen had to satisfy several conditions. First, that we could compare the number of cones before and after the induction of death in each organoid. This is important since the number of cones varies across individual organoids. Second, that the time period in which death happens is short, within days. The reason for this is practical: it allows the testing of more organoids and compounds. Furthermore, organoids do not need a medium exchange within a few days, thus allowing live-imaging of the same organoids in the same positions. The short time period to detect cone death required that the degeneration of cones is induced synchronously and progresses rapidly within and across organoids. An alternative would have been the use of patient-derived or CRISPR-engineered human organoids with either primary or secondary cone degeneration. However, cone degeneration in such organoids has so far not been observed. If it is observed in the future, it is likely to happen over a long period of time and asynchronously. Third, that during the period in which cone death occurs, organoids should reach a state in which about half of the cones die and half remain alive, thus allowing a search for compounds that protect cones and those that damage cones. Fourth, the use of a large number of organoids. On the one hand, this allows for the screening of many compounds; on the other hand, the large numbers allow study of potentially confounding variables that affect cone death. Such a confounding variable was the number of cones before starvation: the percentage of cones dying in the low glucose condition is lower in small organoids with fewer cones. Interestingly, the fact that human retinal organoids need to grow for ca. 30 weeks to yield developed cones did not hinder the screen. Since batch-to-batch variability in cone survival was not detected, different batches of organoids could be initiated in a short time period, one after the other, and thus many organoids could be produced semi-parallel.

We developed three cell-counting algorithms for counting cones from the stack of images taken of each organoid. Each image stack was ~260 MB and the entire dataset was ~5 TB. We used the 3D-additive-count as the primary measure, since MIP-count loses information on the edges of the organoids, where different cones are merged in the maximum intensity projection, and since the 3D-count is computationally time consuming.

In the course of this work, we developed a promoter, ProA330, that allows specific labeling of rods in human organoids. Thus, we could mark cones and rods in the same organoid using ProA7-

driven GFP and ProA330-driven tdTomato from two different AAVs. In the future, these dual color organoids will enable human retinal organoid screens focused on rods and cones simultaneously.

Since most organoids have more than one cell type, and in many organs diseases affect specific cell types, the methods of and the lessons learned from the cell type-focused screen we conducted in human retinal organoids are likely to be useful for performing large-scale screens in other types of human organoids.

### ***Compounds that damage cones and HDAC inhibition***

We identified 146 compounds that caused significant damage to cones in human retinal organoids. A previous study demonstrated that six compounds known to damage retina of human subjects also have detrimental effects on photoreceptors in human retinal organoids<sup>9</sup>. Hence, it is probable that a number of these compounds would also harm cones in human subjects.

We found that HDAC I/II inhibitors with a wide range of targets lead to significant damage to cone photoreceptors. This damaging effect is proportional to the logarithm of the compound concentration. However, the use of more selective HDAC inhibitors results in lower negative impacts on cones in human organoids. It was shown that inhibiting HDACs broadly in the developing mouse retina using trichostatin-A reduces the expression of transcription factors, including *Otx2*, *Nrl*, and *Crx*, which are important for rod development. Additionally, inhibiting HDACs in mouse retinal explant cultures resulted in a complete loss of rod photoreceptors<sup>62</sup>. Conversely, overexpression of *Hdac4* in a mouse model of retinal degeneration extended the survival of photoreceptors<sup>63</sup>. Taken together, this work on cones of human retinal organoids together with the work on rods in mouse retina<sup>62,63</sup> suggests that broad HDAC-inhibition is damaging to both cone and rod photoreceptors. This is particularly relevant because various HDAC inhibitors are currently being tested in clinical trials or have already been approved for cancer treatment<sup>64</sup>. Therefore, it will be important to monitor the structure and function of the retina in patients receiving these treatments.

Interestingly, some studies have found that broad inhibition of HDACs by trichostatin-A in mouse models of retinal degeneration can have positive effects on cones<sup>47,48</sup>, and another study has suggested that targeted inhibition of HDAC 6 positively impacts the cones of mice<sup>49</sup>. Currently, it is unclear why the impact of broad HDAC inhibition on cone cells differs between humans and mice.

### ***Compounds that protect human cones***

Considerable effort has been made to find ways to protect cones in animal models of retinal degeneration<sup>32-46</sup> and some identified modifiers of cone death are currently being evaluated in clinical trials<sup>65</sup>. However, no treatment for protecting cones in photoreceptor diseases such as macular degeneration or retinitis pigmentosa has yet received approval for use in humans.

In this study, we adopted a complementary approach by screening compounds based on their ability to enhance human cone survival in organoids. We induced cone death using glucose starvation not only because it induces synchronous and rapid cone death but also because it was shown that cone photoreceptors undergo starvation-induced death in photoreceptor diseases<sup>32,38,66-68</sup>. We isolated four compounds that demonstrated a significant protective effect on cones after seven days of glucose starvation.

Two of the four compounds that protected cones, HSP90AA1I-1 and HSP90AA1I-2, target the same protein, HSP90. An earlier study demonstrated that a single dose of an HSP90 inhibitor improved visual function and delayed photoreceptor degeneration in a P23H transgenic rat model<sup>69</sup>. Despite the protective effects on photoreceptors observed in both human organoids and rats, we argue that inhibiting HSP90 is not suitable for preserving human cones. First, inhibiting HSP90 caused significant damage to cones in human organoids after 14 days of treatment. Second, HSP90 inhibition resulted in major alterations in the transcriptomes of both cone and rod photoreceptors in human organoids. Third, administering HSP90 inhibitors systemically to dogs was found to induce damage to photoreceptors and to impair vision<sup>70</sup>.

The other two compounds that protected cones, CS-KI-1 and CS-KI-2, are kinase inhibitors. Three pieces of evidence suggest that the currently labeled targets are not responsible for the effects of CS-KI-1 and CS-KI-2 in cones. First, many inhibitors targeting the same labeled targets had no impact on the survival of cones. Second, the IC50 values of different inhibitors were not correlated with the magnitude of the protective effect on cones. Third, the targets of CS-KI-2 (PDGFRA and PDGFRB) are not expressed in organoid cones. However, our experiments indicate that these two compounds or modification of their causal targets have the potential to protect human cones, and possibly also rods. First, both CS-KI-1 and CS-KI-2 demonstrated protective effects on cones in human retinal organoids after longer periods of time. Second, CS-KI-2 was also protective for human rods. Third, CS-KI-1 did not cause major changes in the gene expression profiles of human cones. In the future, identifying the specific targets of CS-KI-1 and CS-KI-2 in cones could pave the way to the discovery of more potent compounds acting on the same targets, as well as other means of interfering with these targets specifically in cones.

### ***Differential effect of starvation and compounds on cones and rods***

Other cell types in human retinal organoids must also be affected by glucose deprivation. However, the rationale for quantifying cones in the primary screen was that the gene expression patterns of different cell types are significantly different and therefore the effect of glucose deprivation and the effect of compounds that protect or damage different cell types can be different. Our strategy was therefore to first identify compounds that affect cones and then test them on other cell types, such as rods.

Despite cones and rods being closely related cell types, the effects of some compounds on the survival and the transcriptomes of cones and rods were different. First, HSP90AA1 inhibition by HSP90AA1I-1 led to cone damage after 10 days of incubation. This was not observed in rods. Second, CS-KI-1 application led to a significantly different effect on gene expression in cones and rods. Therefore, focusing compound screens on the specific cell type of interest in a given disease will likely result in more appropriate molecules than those found by cell type-agnostic screens.



## **ACKNOWLEDGMENTS**

We thank V. Moreno-Juan, A. Muller, Á. Herrero-Navarro, T. M. Rodriguez, A. Fratzl, L. Utz, T. Dalmay and P. King for comments on the manuscript. We thank other members of the Roska laboratory for their discussions on the manuscript. The project was supported by a European Research Council advanced grant (HURET N°883781), Swiss National Science Foundation Synergia grant (CRSII3\_141801), Swiss National Science Foundation grant (310030\_212186), a Louis-Jeantet Foundation award, a Körber Foundation award, and the NCCR Molecular Systems Engineering grant to B.R.

## **AUTHOR CONTRIBUTIONS**

S.E.S. designed and conducted experiments, including the primary and secondary screens, cultured and prepared organoids, including dissociations, analyzed and interpreted data, including the screening data, and wrote the paper. V.J.A.M. conducted experiments, including the primary and secondary screens, cultured and prepared organoids, including dissociations, and designed illustrations. Z.R. developed the cone and rod counting algorithms and analyzed data. S.P.C. analyzed and interpreted RNA-seq data. S.C., O.G., I.G. and I.C. designed and conducted screening experiments and interpreted data. S.R. analyzed and interpreted screening data. P.T.K. conducted experiments for ProA330 discovery. A.V. and J.I. produced AAVs. S.M. performed FASC-sorting. R.A.S. and V.H. conducted RNA isolation and sequencing. Y.H. performed staining and imaging on organoid sections. S.P. supervised RNA-seq experiments. M.C. analyzed data. J.J. supervised AAV production and experiments for ProA330 discovery. C.S.C. supervised RNA-seq analysis. M.D. supervised screening experiments. D.K.B. supervised screening experiments and analysis, M.R. supervised organoid production and screening experiments, V.U. supervised screening experiments, B.R supervised experiments, analyzed and interpreted data, and wrote the paper.

## **DECLARATION OF INTERESTS**

The authors declare no competing interests.

## **MATERIALS AND METHODS**

### ***Generation of retinal organoids***

Retinal organoids were generated as previously described<sup>22</sup>, with the modifications given below. All experiments in this study were performed using organoids that were 30- to 32 weeks old.

### ***Induced pluripotent stem cell culture***

Organoids were derived from the induced pluripotent stem cell line 01F49i-N-B7<sup>22</sup>. The cells were cultured at 37°C and 5% CO<sub>2</sub> in a humidified incubator, using mTesR1 medium (STEMCELL Technologies, #85850) on Matrigel-coated (Corning, #356230) 6-well plates (Corning, #3516). The culture medium was replaced daily and cells were passaged weekly using 0.5 mM EDTA (Invitrogen, #15575020) in PBS without CaCl<sub>2</sub>/MgCl<sub>2</sub> applied for 3-5 min to facilitate detachment of cells as small clumps for subsequent seeding.

### ***Embryoid body formation and culture***

Induced pluripotent stem cells were detached and a single-cell suspension was created using 0.5 mM EDTA (Invitrogen, #15575020) for 3 min, followed by a 3-min Accutase (Thermo Fisher Scientific, #00-4555-56) treatment at 37°C. Embryoid body formation took place in 256 microwell-hydrogels with ~250-300 cells seeded per microwell. The hydrogels were generated using a MicroTissues 3D Petri Dish micro-mold (Sigma Aldrich, Z764000) and 2% agarose (Thermo Fisher Scientific, #R0491). Each hydrogel was cultured in a 12-well plate (Corning, #3513) in neural induction medium DMEM / F12 (GIBCO, #31331-028), 1% N2 Supplement (GIBCO, #17502-048), 1% NEAA Solution (Sigma, #M7145) and 2 mg/mL heparin (Sigma, #H3149-50KU) for one week with daily medium exchanges. Embryoid bodies that formed in one 256 microwell-hydrogel were detached from the hydrogel and distributed evenly across three wells of a Matrigel (Corning, #356230)-coated 6-well plate (Corning, #430166).

### ***Early organoid culture and checkerboard scraping***

Organoids in 6-well plates cultured with daily medium exchanges started to form 2D confluent structures. For the first 16 days, they were cultured in neural induction medium. The medium was subsequently changed to 3 parts DMEM (GIBCO, #10569-010): 1 part F12 medium (GIBCO,

#31765–027) ('3:1 medium'), supplemented with 2% B27 without vitamin A (GIBCO, #12587010), 1% NEAA Solution (MERCK, #M7145), and 1% penicillin / streptomycin (GIBCO, #15140–122). Checkerboard scraping was performed between days 28 and 30 of culture as described previously<sup>22</sup>.

### ***3D-organoid culture***

Aggregates from four wells of a 6-well plate were transferred to one 175 cm<sup>2</sup> tissue culture flask (Thermo Scientific, #159926) previously treated with an anti-adherence solution (StemCell Technologies, #07010). Flasks containing organoids were filled with 35 - 45 mL of medium, which was replaced 1-3 times per week. The flasks were maintained in 3:1 medium for 6 weeks of culture. The medium was supplemented subsequently with an additional 10% FBS (Millipore, # ES-009-B) and 100 µM Taurine (Sigma, #T0625–25G) until week 10. Until week 14, the medium was further supplemented with 1 µM retinoic acid (Sigma, #R2625). After this period, the retinoic acid concentration was reduced to 0.5 µM and the B27 supplement was replaced with N2 supplement (GIBCO, #17502–048) for the remaining duration of the culture. For easy access to organoids for experiments, they were transferred to round cell culture dishes (Thermo Fischer, #101VR20). Aggregates lacking neuroepithelium were removed just before the experiments.

### ***Organoid fixation, sectioning and staining***

Organoids were fixed in paraformaldehyde for 4 h at 4°C and washed three times for 10 min each in PBS. They were then submerged in PBS containing 30% sucrose for cryopreservation. Fixed organoids were stored at -80°C.

For sectioning, the organoids were embedded in a solution of 7.5% gelatine and 10% sucrose in PBS. The embedded samples were then frozen and sectioned into 25-µm-thick slices using a cryostat (MICROM International, #HM560).

Immunostaining was carried out as described previously<sup>22</sup>. Briefly, slides were dried for 30 min at room temperature, then rehydrated in PBS for 5-10 min. They were then blocked with a solution containing 10% normal donkey serum (Sigma, #S30–100ML), 1% BSA (Sigma, #05482–25G), 0.5% Triton X-100 (Sigma, #T9284500ML), and 0.02% sodium azide (Sigma, #S2002–25G) at

room temperature for 1 h. Sections were then treated with primary antibodies (listed in Table S4) in a similar blocking solution but with 3% normal donkey serum for 24 h. After three washes in PBS with 0.1% TWEEN 20 (Sigma, #P9416100ML) for 10 min each, the slides were exposed to secondary antibodies (Thermo Fisher Scientific, donkey secondary antibodies conjugated to Alexa Fluor 488, 568, or 647) diluted 1:500 and Hoechst 33342 (Thermo Fisher, #62249) diluted 1:10,000 in the same buffer as the primary antibodies for 2 h. This was followed by two 10-min washes in PBS with 0.1% Tween and a 15-min wash in PBS. Slides were finalized with ProLong Gold (Thermo Fisher Scientific, #P36934) before sealing.

### ***Imaging stained cryosections***

Images of representative regions of the organoids were captured using a spinning disc confocal microscope (Olympus IXplore SpinSR). The microscope was adjusted to either 20x or 40x magnification and images were taken across multiple Z-planes. All captured images are shown as maximum intensity projections.

### ***AAV production***

Adherent HEK293T cells (ATCC, #CRL3216) were cultured in a 5-layer CellSTACK (3,180 cm<sup>2</sup>; Corning, # CLS3319) for AAV vector production. These cells were co-transfected with an AAV transgene plasmid, an AAV helper plasmid encoding the AAV Rep2 and Cap proteins for the selected AAV9-PHP.eB capsid<sup>55</sup>, and the pHGT1-Adeno1 helper plasmid carrying adenoviral genes (kindly provided by C. Cepko, Harvard Medical School, Boston, USA) using PEIMAX (Polyscience, #POL24765-1). Plasmids were mixed in 98 mL DMEM (Thermo Fischer, #11965-092) and incubated for 5 min. PEIMAX was then added to the DMEM-diluted DNA. After an additional 10-min incubation, the DNA-PEIMAX complex was added to the cells. After 60 h, the culture medium was supplemented with 250 mL fresh DMEM containing 1% Pen-Strep (Thermo Fischer, #15140-122). AAV vectors present in cells and the culture medium were harvested approximately 5 days post-transfection.

### ***Purification of AAVs***

AAVs were purified either from cell culture medium alone or from both cells and cell culture medium. The cell culture supernatant was first cleared by centrifugation at 1400 x g for 15 min

(5920R; Eppendorf) and then filtered through a 0.45- $\mu$ m PES filter (Merck Millipore, #S2GPU02RE). The cell pellet was resuspended in 11 mL lysis buffer (150 mM NaCl, 20 mM Tris-HCl pH 8.0) and subjected to three freeze-thaw cycles. To remove cell debris, the cell lysate was centrifuged at 4,000 x g for 30 min and the resulting supernatant filtered through a 0.45- $\mu$ m filter.

Both the filtered cell culture medium and the cell lysate were treated with Turbonuclease (Accelagen, #N0103L) at 50 U/mL for 1 h at 37°C. The sample was then loaded onto an affinity column (POROS CaptureSelect AAVX; ThermoFisher, #A36652) and eluted with a solution of 0.1M glycine (Merck, #1.04201.1000), 0.25M arginine (Sigma, A5006), 0.2 M NaCl (pH 2.7; Sigma, 31434), following an extensive wash with 20 times the column volume of 500 mM NaCl, 50 mM Tris at pH 7.3 (Merck, 93350), and 0.01% Pluronic F-68 (Thermo, #24040032). The eluted AAVs were immediately neutralized with 1/11 volume of 1 M Tris-HCl pH 10. The purified AAV vectors were then concentrated as needed in sterile PBS + 0.001% Pluronic F-68 using a spin filter (Amicon Ultra Centrifugal Filter Units; Millipore Sigma, UFC910096; molecular cutoff 100 kDa).

### ***AAV titration***

Encapsidated viral DNA was quantified using TaqMan RT-PCR (Thermo Fischer, #4444557) targeting the ITR sequences (forward primer: GGAACCCCTAGTGATGGAGTT; reverse primer: CGGCCTCAGTGAGCGA; probe: [6FAM]CACTCCCTCTCTGCGCGCTCG[BHQ1]) relative to a linearized ITR-containing plasmid as a standard. Prior to quantification, AAV particles were denatured using Proteinase K (Thermo Fischer, #11501515). The titers were then calculated and expressed as genome copies per mL.

### ***AAV transduction of organoids in 96-well plates***

For small-scale experiments (Figures 5, 6 and S10), individual organoids were transferred to a single well of an ultra-low attachment U-bottom 96-well plate (Corning, #7007) after 25 to 26 weeks of maturation. AAVs were diluted in culture medium to a concentration of  $3.3 \times 10^{12}$  genome copies per mL. The existing medium in the wells was removed from the organoids and replaced with 30  $\mu$ L of the AAV solution. After an incubation period of 4-5 h, an additional 70  $\mu$ L of medium was added per well. After 24 h, 100  $\mu$ L of medium was added on top per well. After a

further 24 h, 150  $\mu$ L of medium was replaced per well. Transduced organoids were then cultured for 4 to 5 weeks at 37°C and 5% CO<sub>2</sub> before the onset of further experiments. During this period, the medium (150  $\mu$ L per well) was replaced 3 times per week.

### ***Bulk AAV transduction of organoids***

For large-scale experiments (Figures 1-5 and S1-S9), organoids were transduced with AAVs in their original flask (Sigma Aldrich, #Z764000). AAVs were diluted in culture medium to a concentration of  $1 \times 10^{13}$  to  $2.5 \times 10^{13}$  genome copies per mL. The flasks were placed upright and the medium aspirated from the organoids. AAV solution was then added at 8 mL per flask and the flasks incubated in the upright position for 24 h. Following this, 32 mL of medium was added to each flask and the flasks were then laid flat. After a further 24 h, the medium was exchanged completely. The transduced organoids were cultured for an additional 4-5 weeks at 37°C and 5% CO<sub>2</sub> with a medium exchanged once a week.

### ***Low-throughput imaging***

All non-screening imaging (Figures 1, 4G-I, 5, and 6A) was conducted using a spinning disk confocal microscope (Olympus IXplore SpinSR) with a 4x or a 10x objective. For live imaging, organoids were kept in a humidified chamber maintained at 37°C with 5% CO<sub>2</sub>. The contrast and brightness settings for images captured from the same organoid across different timepoints were the same.

### ***Glucose starvation***

After 30 weeks of maturation and four weeks after AAV transduction, organoids were transferred into an ultra-low attachment U-bottom 96-well plate (Corning, #7007) with 150-200  $\mu$ L medium. The remaining medium was then reduced to approximately 60  $\mu$ L per well.

The low glucose starvation medium was composed of 3:1 medium supplemented with an additional 10% heat-inactivated FBS (Millipore, #es-009-b), N2 supplement (GIBCO, #17502-048), 100  $\mu$ M taurine (Sigma, #T0625-25G), and 0.5  $\mu$ M retinoic acid. Instead of the standard DMEM, DMEM with no glucose (Thermo Fisher, #11966025) was used. The normal glucose medium was prepared similarly but with regular DMEM containing 25 mM glucose (Thermo

Fisher, #10569010). The low glucose medium still contained a small amount of glucose due to the F12 medium (GIBCO, #31765–027) and possibly the FBS.

Prior to the addition of the respective experimental conditions, organoids including the normal glucose controls were washed twice with 120  $\mu$ L of low glucose medium. This process was conducted manually or, for screening experiments, with a 96-well head Selma pipettor (Cybio, #OL7001-26-212) fitted with 60- $\mu$ L tips (Cybio, #OL3800-25-735-P).

### ***Glucose consumption measurement***

Organoids were transferred to an ultra-low attachment U-bottom 96-well plate (Corning, #7007) and subjected to glucose starvation. On each measurement day, 5  $\mu$ L of medium was collected from the 180  $\mu$ L of medium for each of the 10 organoids per condition. For the initial measurement, which involved only medium without organoids, three replicates were taken. The glucose concentration was subsequently determined using a Glucose Colorimetric Detection Kit (Invitrogen, #EIAGLUC). The assay results were read using a Hidex Sense Microplate Reader.

### ***Compound preparation, dilution, and addition***

A set of 2,707 annotated compounds selected for screening on retinal organoids was sourced from the Mode-of-action (MOA) compound library<sup>54</sup>. The compounds, originally at a stock concentration of 10 mM in 100% DMSO, were plated in 384-well low dead volume plates (Labcyte, #LP-0200). Using the ECHO acoustic liquid handler (Labcyte, #Echo 555), 225 nL of the compounds was transferred into sterile 96-well polypropylene U-bottom microplates (Greiner, #65026). These plates were stored overnight at 4°C in a confined environment to prevent evaporation.

The following day, the plates were brought to room temperature and the compounds diluted 666 times by adding 150  $\mu$ L of low glucose medium with the multidrop combi dispenser (Thermo Scientific, #5840300). Using a 96-well head Selma pipettor (Cybio, #OL7001-26-212) equipped with 60- $\mu$ L tips (Cybio, #OL3800-25-735-P), 120  $\mu$ L of culture medium was removed from the ultra-low attachment U-bottom 96-well assay microplates (Corning, #7007) containing the organoids. Then, using the same pipettor, 120  $\mu$ L of compounds diluted in medium were pipetted

from the intermediate 96-well plates into the plates containing the retinal organoids. The assay plates were then incubated (5% CO<sub>2</sub>; 37°C; humidified environment) in an automated incubator (Thermo, #incubator Cytomat 10 C 450) until imaging. Each compound was tested in five replicates at a final concentration of 10 μM. All vehicle controls were 0.1 % DMSO in low glucose or normal glucose medium. In the secondary screens, the compounds were tested at four different concentrations (10; 1; 0.1 and 0.01 μM) using the compound transfer process as in the primary screen.

HSP90AA1I-1 together with CS-KI-1 (Figures 4G-H, 5C-D and 6) were newly synthesized by Enamine. CS-KI-2 was purchased from MolPort (Figures 4I, 5D). These were dissolved in 90% DMSO prior to manual dilution in low glucose medium. The vehicle controls for these experiments involved 0.09% DMSO. HSP90AA1I-1 was added at a concentration of 1 μM and CS-KI-1 and CS-KI-2 at a concentration of 10 μM.

### ***Automated imaging***

Confocal images for all screening experiments were captured using a 4x objective lens (Olympus UPLSAPO, NA=0.16) on an automated spinning disk confocal microscope equipped with a sCMOS camera (Yokogawa, CV7000). The samples were maintained in a 5% CO<sub>2</sub> and 37°C environment during acquisition. Images were acquired at 24 different confocal planes, each separated by a 34-μm interval, to cover the entire organoid. This was followed by the acquisition of a stack of seven brightfield images at 100-μm intervals. After image acquisition, each plate was incubated (5% CO<sub>2</sub>; 37°C; humidified environment) for seven days and then re-imaged using the same procedure.

### ***Promoter ProA330***

The general design and the testing of ProA series promoters have been described previously<sup>14</sup>. The AAV serotypes used were AAV9-PHP.eB<sup>55</sup> for human retinal organoids and AAV8-BP2<sup>71</sup> for mouse injections. This new promoter has the following sequence:

```
AACCCAAGAAATTACAGGCTGAAACCAGAAAAGAACACATTAAAGCACCAAGAGAA
AGTTGGAGTGGGTTGAAGGGAAACAGATTTTTAAAGTTAAGGCTCTGTGAAATGGGT
AGAATTA ACTACAGGT TAAAAATAAAATGTTAACTAAAGGTTGCCTCTGAGTAACAGG
```



ATTATGGGTGATTTTAATTGTCTTCTTTGTGTATGTTCAACAGTGACTATAATATGTATTA  
CTTTTGAATAAAGGAAAACCTGAAAGGTGTGTTGTTTTATAAGGGCCCTTAGGTTGC  
CAAAATTAGAGTCATTGAAATCTAAAGCTGATAAAAACCTTTAGTGCAAAGATTGTGAC  
ATGGGAGACTACACATACCAGATCCATAATGTACATGAGGACAGTAGGCCGAGGGGC  
CCTGCACATTGAAAGCCCACATGGGAGAAGCCCTTGGGAAGGGGAGTGGAAGGATG  
AGGCAAGGGGCCGGGGGGATGCAGAGGCTGGCAGGCAGTCATTTCTCAGCTTCAGC  
CATTCCCGCCATGGGGGAATGTGGACAGAGAAGCCAAACAAATCTCCTAACAGTAA  
ATGTCAGTCTTCTGTGTCAGATATTTAAGAAAACCTAACAGAGGTCAGAGAAGACACA  
CCTACAGCAAGTAGACTGTCCCTGTGCTGCCTTTTTGCAACCCCTGCTTTGGCAGTGC  
TCAAGCCCACCTCCTGCTCTGTGCAGACATCTCTTCTTTGCTCTTACTAGACCAAGGT  
GAAAGAAAACCTCTCACCTTCTCCCATCTGGCCCCACAGCATCTGGAACACACTGATC  
CTCATAATCCTTGTTCTTGAGAAATATTAATGACTTAATCTCCCAAGCTTGCTCCCTCTC  
CTGTGCAGGCCATCTCAGTATGTTTTGCAGACAAGACCCAGAGAAGTCCAGACTGGA  
CTTGTTGCAGACTGCAAAACTGCCATTGGAAGGCCTCCGTCCCAGTCCTTCTACAGA  
GTAGCCAGTGGGATTCCCAGCC

### ***Organoid dissociation and FACS-sorting for RNA-seq***

For bulk RNA sequencing, organoids at week 26 were co-transduced with a ProA7-GFP<sup>14</sup> construct (cone-specific promoter driving GFP expression) and ProA330-tdTomato (rod-specific promoter driving tdTomato expression). Four weeks post-transduction, organoids were subjected to their corresponding treatments (normal glucose, low glucose, and low glucose with either HSP90AA1I-1 or CS-KI-1) in 96-well plates. After seven days of treatment, individual organoids were dissociated using the reagents from the Neural Tissue Dissociation Kit (P) (Miltenyi Biotec, #130-092-628).

Each organoid was transferred to a 1.5-mL Eppendorf tube, washed once with 1 mL PBS, and then with 1 mL of provided Buffer X. Subsequently, 25  $\mu$ L of provided Enzyme P solution was diluted in 1 mL Buffer X and added to the organoids. Organoids were then incubated in the enzyme solution at 37°C with agitation at 900 rpm for 25 min. During this incubation period, the organoids were pipetted up and down using a 1-mL pipette every 5 min to assist dissociation. Then 5  $\mu$ L of Enzyme A together with 10  $\mu$ L of Buffer Y were added to the partially dissociated organoids,

followed by a 15-min incubation at 37°C without shaking. Thereafter the cells from the fully dissociated organoids were handled on ice. The dissociated cells were centrifuged at 300 x g for 5 min at 4°C to pellet the cells and remove residual enzyme solution. The cell pellet was then resuspended in 250 µL PBS and passed through a 70-µm filter (pluriSelect, 43-10070). Prior to FACS-sorting, Hoechst 33342 (Thermo Fisher, 62249) was added to the cell suspension at a 1:10,000 dilution. This was done to allow exclusion of debris from nucleated cells during FACS.

FACS-sorting was performed using a FACSAria (BD Biosciences). Fluorescent cones and rods were sorted directly into RLT-Buffer from the RNeasy kit (Qiagen, #74104) for subsequent RNA extraction.

### ***Bulk RNA-sequencing***

RNA was extracted from FACS-sorted cells using an RNeasy Mini column-based isolation according to the manufacturer's instructions (Qiagen, #74104). Following extraction, 1 µL of RNA was used to prepare RNA libraries using a bulk input optimized FLASH-seq protocol<sup>72,73</sup>. Briefly, RNA was converted to cDNA fragments using Superscript IV (Thermo Fisher Scientific, #18090200) and amplified with KAPA HiFi HotStart (Roche, #KK2602,). The cDNA was then cleaned using a 0.8x ratio of homebrew SeraMag beads in 18% PEG (CytiviaTm, #GE24152105050250). cDNA concentration and quality were measured using Qubit (Thermo Fisher Scientific, #Q33231) and an Agilent Bioanalyzer (Agilent, #5067-4626). The cDNA was normalized to 200 pg/µL before tagmentation using 0.2 µM of homemade Tn5. Tn5 transposase was produced by the EPFL Protein Facility (Lausanne, Switzerland). The reaction was halted with 0.2% SDS. An indexing PCR was performed to add Nextera index adapters (1 µM, Integrated DNA Technology) using KAPA HiFi reagents (Roche, #KK2102). Libraries were pooled in equal volumes and a final 0.8x cleanup performed with homebrew SeraMag beads before measuring sample concentration and quality. The library pool was normalized and sequenced on Illumina NextSeq MO flowcell (75-8-8-75) at approximately 1 million reads/sample. Basecalling and demultiplexing were performed with bcl2fastq (v2.20, Illumina Inc.).

### ***Quantification and statistical analysis***

All quantifications, statistical analyses, and plots were executed using R, Python, ImageJ or GraphpadPrism. All illustrations were created using Adobe Illustrator, while chemical structures were rendered with ChemDraw.

If not stated otherwise, ‘n’ always refers to the number of organoids per condition. The p-values depicted in the figures are not corrected for multiple testing. A summary of the primary screen dataset can be found at <https://ConeTargetedCompoundScreen.iob.ch>.

### ***Promoter specificity and efficacy analysis***

Promoter specificity and efficacy quantification was performed using ImageJ. Maximum intensity projections were calculated and cells were then manually counted using the ImageJ plugin, Cell Counter.

For the ProA7-GFP construct (Figure 1E), five different organoids were analyzed. The specificity was determined by calculating the percentage of all GFP-positive cells that were also ARR3-positive. Efficacy was determined by calculating the percentage of all ARR3-positive cells that were also GFP-positive.

For the ProA330-GFP construct (Figure 5B), three different organoids were analyzed using the methods used for ProA7-GFP. Specificity was determined by calculating the ratio of all GFP-positive cells located in the outer nuclear layer that were not ARR3-positive. Efficacy was determined by calculating the percentage of GFP-positive and ARR3-negative cells among all cells of the outer nuclear layer counted by Hoechst staining. The specificity and efficacy in mice were evaluated in a similar manner, using three retinas from two mice (Figure S9). Specificities and efficacies in the results section are displayed as mean  $\pm$  sd.

### ***Cell counting algorithms***

To assess cone survival in organoids, an algorithm was designed that locates and counts local maxima in pixel intensity values corresponding to GFP-expressing cells. Three distinct counting approaches were employed: counting was done image-by-image from a 3D confocal stack

(referred to as ‘3D-additive-count’), from the entire 3D stack (referred to as ‘3D-count’), and from the maximum intensity projection of the 3D stack (referred to as ‘MIP-count’).

Initially, Gaussian filtering was applied to each image to minimize background noise. Following this, local maxima in pixel intensity were identified within each image using the `peak_local_max` function from the `Skicit-image` package in Python. Any detected local maxima that fell below 1.25 times the frame's average pixel value were disregarded. This was performed in 3D for the 3D-count. These detected local maxima were then subjected to a three-step filtering process to ensure they accurately represented cone cells.

In the first step of filtering, local maxima of low contrast were removed by applying Otsu thresholding to a local Region of Interest (ROI) around the local maximum. If active pixels were detected at the ROI edges, the window size was expanded. This iterative process continued until only inactive pixels were found at the ROI edges. Local maxima corresponding to ROIs exceeding a size of 70 x 70 pixels (113.75 x 113.75  $\mu\text{m}$ ) were excluded. The second filtering step aimed to separate objects that were closely situated. Objects with a diameter ranging from 8.1 to 65  $\mu\text{m}$  and with a perimeter-to-area ratio between 4 and 6.5 were selected for a process known as binary erosion, which effectively separated such adjacent or touching objects.

In the final filtering step, attributes like object diameter, perimeter-to-area ratio, and the contrast between object foreground and background were analyzed. Only objects with diameters between 6 and 100  $\mu\text{m}$  and a perimeter-to-area ratio between 0.1 and 4 were retained. Low-contrast objects, defined as those for which the foreground was no more than 1.2 times brighter than the background, were also excluded.

All filtering steps for the 3D-count were done in 2D on the z-plane where each local maximum was identified.

In some experiments where noise levels were high, cell candidates where all pixels were below 150 were excluded (Figure 1H, S1 and 4G-4I). The cell counts obtained were normalized to the initial cell count yielding relative cone survival values.

For counting rod photoreceptors (Figure 5D), slight modifications were made to the parameters of the cone-counting algorithm. For rod photoreceptors, the maximum intensity projections were quantified. The image resolution was enhanced fourfold via cubic interpolation. The minimum allowable diameter for cell candidates was also reduced from 4  $\mu\text{m}$  to 2  $\mu\text{m}$ , and any candidates where all pixels were below an intensity of 200 were excluded.

If not stated otherwise cone-survival was calculated using the counts from the 3D-additive-count algorithm.

### ***Target categorization***

Categorizer software<sup>74</sup> was used to categorize the targets of the MOA compound library. Target categories were assigned to their respective compounds. If a compound had multiple targets, the most common category found among the targets was assigned.

### ***Cone count thresholding***

For the primary screen, thresholds were determined after visually inspecting images with the lowest reported D0 counts, ensuring the inclusion of as many data points as possible. These thresholds were set uniquely for each quantification algorithm (Figure S2). The threshold for the secondary screens were the same as for the primary screen (Figures S4 and S6).

### ***Adjusted cone survival***

To compensate for the effect of initial cone counts on the survival of glucose deprivation, we calculated an adjusted version of the cone survival. For this, a linear model was fitted using the complete primary screen dataset to explain the cone survival with the logarithm of the scaled cone counts at D0. The obtained regression coefficient was then multiplied with the scaled logarithm of the D0 cone counts. Subtracting this term from the original cone survival yielded the adjusted values. This was done separately for all three cone counting algorithms (Figures 2E and S2).

This adjustment sometimes led to values higher than 100% and very rarely to values lower than 0%.

Since the cone-damaging secondary screen was done in normal glucose, we analyzed separately the relationship between cone survival and D0 counts in a newly calculated linear model. While we found a linear model that significantly explains this relationship, it only accounted for a marginal amount of the explained variation for all three quantification algorithms (n=711,  $R^2=0.007-0.018$ , p-values<0.001, Figure S6). Therefore, we did not generate adjusted cone survival values for this dataset.

For the cone-saving secondary screen dataset, we used the linear model originally generated from the primary screen to compute the adjusted values. This primary screen model accurately predicted the D0 to cone survival relationship in the secondary screen (n=673-681,  $R^2=0.17-0.22$ , p<0.001, Figure S6).

#### ***Well position bias analysis***

To account for any potential influence on the results of well position within the 96-well plate, an analysis was performed on the mean adjusted cone survival for each well position, based on the primary screen dataset with the 3D-additive-count. This procedure assumes that most of the compounds under study do not exert a significant effect on cone survival. These mean values were then compared. If the differences between the means were found to fall within the range of the minimum standard deviation observed for the least variable well, it was determined that the well position did not have a significant impact on the outcome. Excluding the positions of the normal glucose control wells, cone survival was not influenced by any of the well positions (Figure S2).

#### ***Analysis of primary screen data***

To compare cone survival across various compound conditions while controlling for the initial count at D0, an Analysis of Covariance (ANCOVA) was conducted. In this analysis, the dependent variable was the unadjusted cone survival, and the independent variable was the compound condition (low glucose control vs. compound 1 vs. compound 2, etc.). The raw count at D0 served as the covariate in the model. P-values were calculated for a two-sided test comparing each compound to the low glucose controls. To identify significant hits from the primary screen, a statistical threshold of p<0.05 was set. The Benjamini-Hochberg correction was employed to account for multiple testing. Consequently, only compounds with an adjusted p-value less than

0.05 were considered significant. The compounds selected for secondary screening were determined based on their p-values and after visual inspection of images.

### ***Mode of action names***

The mode of action for each compound was sourced from Canham et al.<sup>54</sup>. For compounds subjected to secondary screens, a concise version of their modes of action was manually generated (Figures 3, 4, S4, S5, S6 and S7).

### ***Analysis of the secondary screen cone-damaging dataset***

To assess the impact of different conditions compared to the control, an Analysis of Variance (ANOVA) was conducted that compared all different compound conditions to the normal glucose control. The resulting p-values were subsequently adjusted for multiple comparisons using Benjamini-Hochberg correction for all compounds and concentrations. P-values were calculated for a one-sided test. Compounds and concentrations with adjusted p-values less than 0.05 were deemed statistically significant. Controls are also displayed in Figure S4.

### ***Clustering cone-damaging compounds from the secondary screen***

To categorize compounds from the secondary screen based on cone survivals at four different concentrations, hierarchical clustering was performed using medians of the cone survival values of all significant cone-damaging compounds. The Elbow Method was employed to identify the optimal number of clusters, involving a plot of the total within-cluster sum of squares (WSS) against the number of potential clusters. WSS values were computed for all possible solutions, ranging from 1 to 34 clusters, and an elbow in the curve was observed at four clusters. The resulting clusters were then assigned to all compounds, as depicted in Figure 3C. One outlier was removed from cluster 3 and one from cluster 4 in Figure 3C.

### ***Definition of target classes***

HDAC1, HDAC2, HDAC3, HDAC4, HDAC5, HDAC6, HDAC7, HDAC8, HDAC9, HDAC10 and HDAC11 were categorized as HDAC I/IIs. SIRT1, SIRT2, SIRT3 and SIRT 6 were categorized as HDAC IIIs. TUBA1A, TUBA1B, TUBA1C, TUBA3C, TUBA3D, TUBA3E, TUBA4A, TUBA8, TUBB, TUBB1, TUBB2A, TUBB2B, TUBB3, TUBB4A, TUBB4B, TUBB6,

TUBB8, TUBD1, TUBG1, and TUBG2 were categorized as tubulins. These target classes were used in Figures 3E, 3F and S4.

#### ***Analysis of the secondary screen cone-saving dataset***

The secondary screen cone-saving dataset was analyzed in the same way as the primary dataset using an ANCOVA with the D0 count as covariate, comparing compound effects to the low glucose controls. The resulting p-values were subsequently adjusted using a Benjamini-Hochberg correction for multiple testing for all compounds and concentrations (Figure S6). The p-values were calculated for a one-sided test. Controls are shown in Figure S6.

#### ***Analysis of target effects in the primary screen dataset***

In the analysis of the impact of compound targets on cone survival, targets with three or more listed compounds were initially selected (Figure 2C). For each of these targets, the average of the median adjusted cone survival across all targeting compounds was determined. This average was then compared to a distribution generated by randomly drawing an equal number of compounds and calculating their mean of the median adjusted cone survival.

This process of random drawing was performed 10,000 times initially to create a distribution of mean values. In the analysis of cone-saving targets, the number of these randomly generated means that were higher than the observed mean was determined (Figures 4E and S8). Conversely, for the cone-damaging targets, the number that were lower was determined (Figure 3F).

If less than 10 of the random means were found to be higher (or lower, depending on the analysis), the process was repeated with 100,000 random draws to ensure robustness. The p-value for each target was then estimated as the fraction of random means that were found to be higher (or lower) than the observed mean, plus one, divided by the total number of random draws.

Finally, to account for multiple comparisons, these p-values were corrected using the Benjamini-Hochberg method and a significance threshold set at 0.05. However, in Figures 3F, 4E and S6 the unadjusted p-values are displayed.



### *Analysis of IC50*

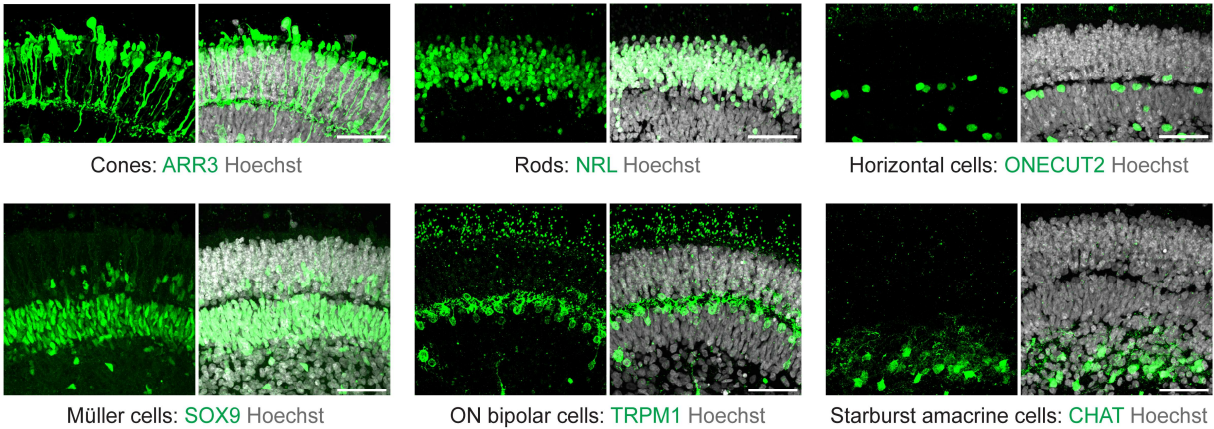
IC50 values for all compounds in the library targeting HSP90AA1, HSP90AB1, MTOR, PIK3CA, PIK3CB, PIK3CD, PDGFRA, and PDGFRB, were sourced from the ChEMBL database<sup>75</sup>. This dataset encompassed reported IC50s, even for compound-target pairs not present in the MOA library. In instances where multiple IC50 values were noted for a specific compound-target combination, the median of these values was used for subsequent analysis. Spearman correlation coefficients were determined by correlating the median-adjusted cone survival with median IC50 values.

### *Analysis of transcriptomes*

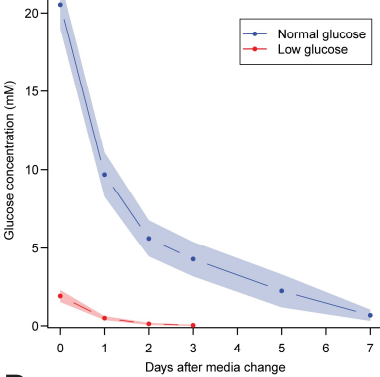
Sequencing reads were processed into gene counts using Snakemake (v7.21.0), a workflow management system. The workflow consisted of two main steps: read alignment and differential gene expression analysis. Reads were aligned against the GRCh38 (Ensembl release 109) reference genome using STAR (v2.7.10b). Both the number of reads per gene (--quantMode GeneCounts) and alignments translated into transcripts coordinates (--quantMode TranscriptomeSAM) were set as outputs. The reference genome was augmented to include sequences from two transgenes (ProA7-GFP and ProA330-tdTomato) used in cell sorting. Read counts per gene and per sample were aggregated using custom Python scripts, and samples with the total number of expressed genes falling below two standard deviations from the average were filtered out, along with genes expressed in fewer than 5% of the samples. DESeq2 (v1.38) was then employed to identify differentially expressed genes, using a log fold change threshold of 1 and a 5% significance level after Benjamini-Hochberg correction for multiple hypothesis testing. Principal component analysis was performed using scikit-learn (v.1.2.2) on normalized and standardized gene counts. Data were normalized to transcript counts per 10,000 adjusted for non-overlapping exon lengths (TP10k), where lengths were estimated using the R package GenomicFeatures (v1.50.2). Marker genes were identified based on an available adult human peripheral retina atlas (<https://data.iob.ch>), by using scanpy's rank\_genes\_groups function. To compare transcriptomes, the average gene expression was analyzed for all genes using a Wilcoxon Signed-Rank Test. In Figure 6E, if a p-value is smaller than  $10^{-40}$ , it is depicted as  $10^{-40}$ .

## SUPPLEMENTARY FIGURES AND SUPPLEMENTARY FIGURE LEGENDS

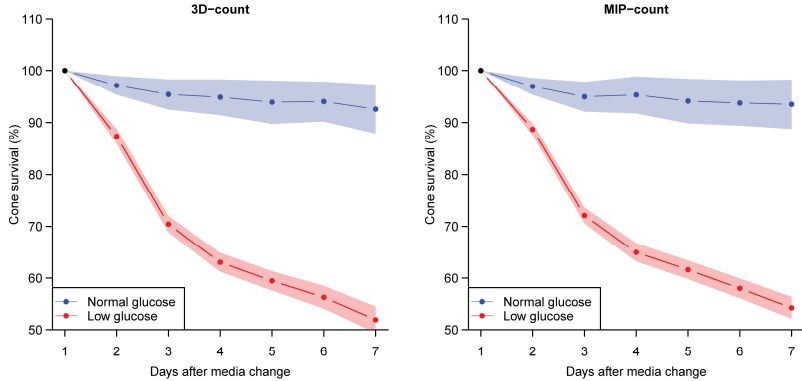
**A**



**B**



**C**



**D**

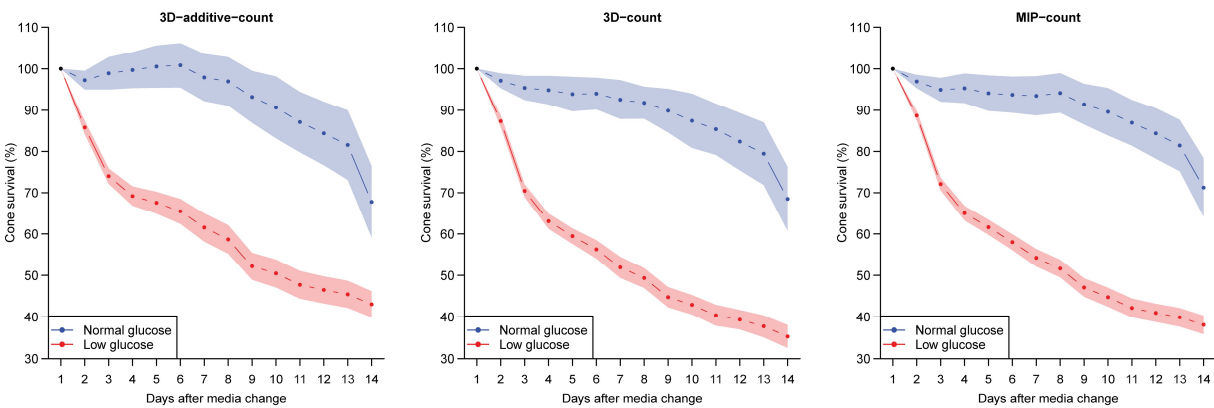


**Figure S1: Cell types of mature human retinal organoids and glucose starvation.**

**A:** Marker gene expression of cell types in human retinal organoids. Confocal images of sectioned and stained human retinal organoids at week 30 of maturation with indicated staining (scale bar, 25  $\mu$ m). **B:** Glucose consumption assay of human retinal organoids. Mean  $\pm$  se from 10 human retinal organoids. **C:** Quantification of cone survival in human retinal organoids in normal and low glucose over seven days. Quantification with either 3D-count (left) or MIP-count (right). Mean  $\pm$  se. Low glucose, n=26; normal glucose, n=6. **D:** Same as (C) but for 14 days using all three quantification algorithms (3D-additive-count, 3D-count, and MIP-count).

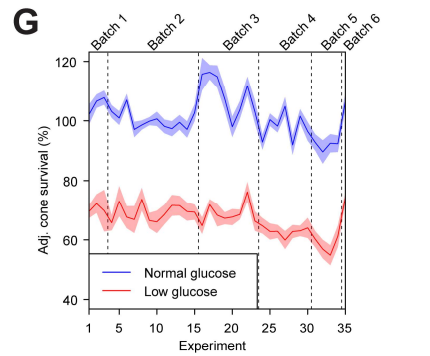
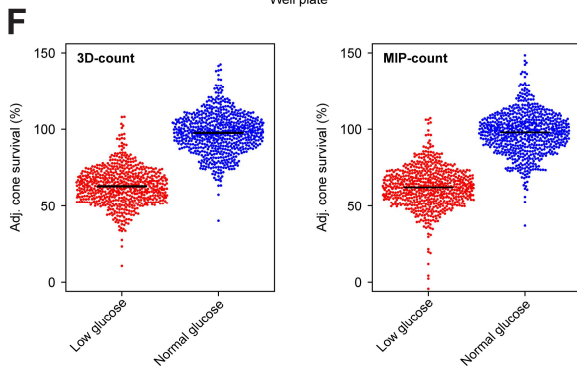
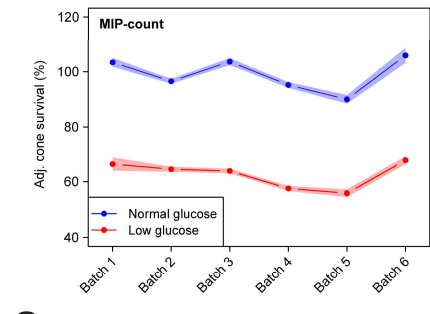
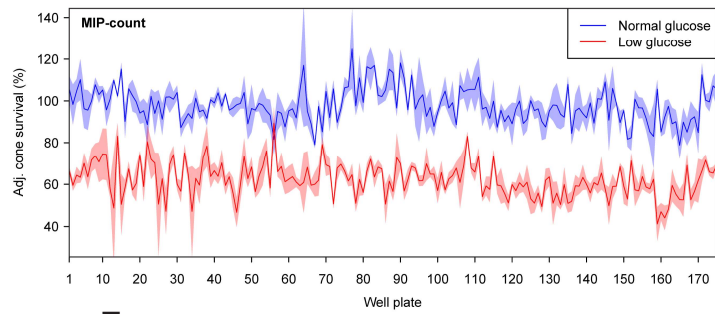
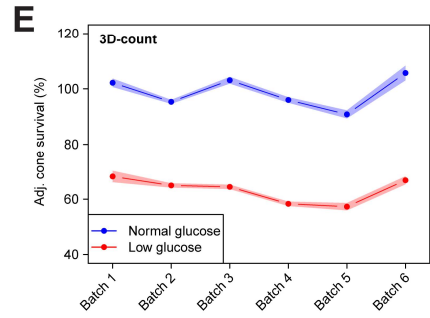
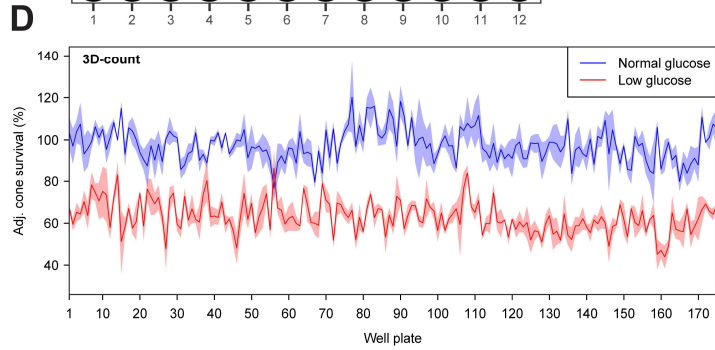
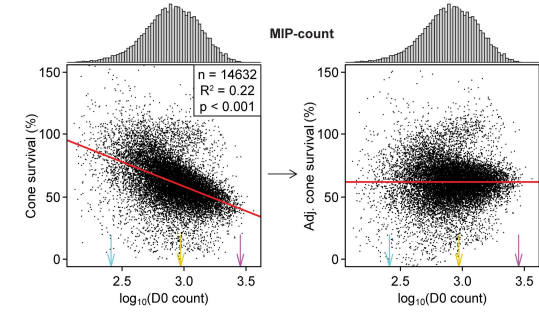
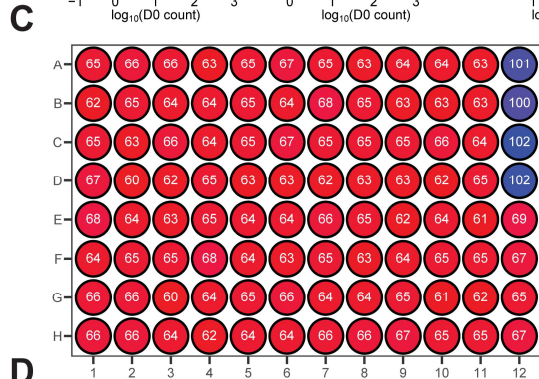
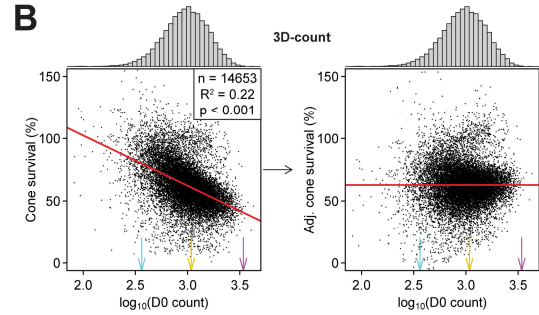
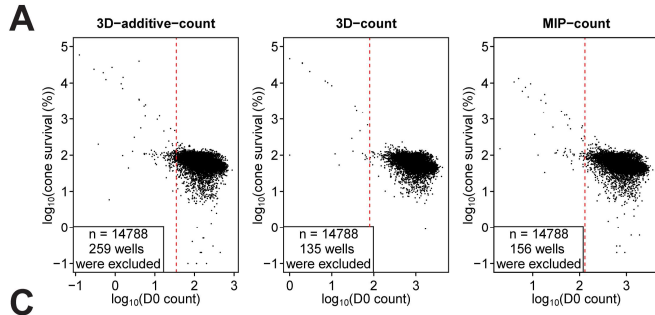


**Figure S2: Primary screen: analysis.**

**A:** Data thresholding based on counts at D0 for all quantification algorithms. The dotted red line indicates the threshold beyond which wells are included in the analysis. **B:** Adjustment of cone survival values based on the D0 count. Top: 3D-count. Bottom: MIP-count. Left: cone survival and the logarithm of the cone count at D0, fitted with a linear model. Regression line, red; summary statistics, top right corner of each panel. Right: adjusted cone survival and the logarithm of the cone count at D0 with the transformed regression line. Colored arrows correspond to D0 counts of example images in Figure 2E. **C:** Well position bias analysis. The means of adjusted cone survival for all wells of the primary screen data are depicted. **D-E:** Adjusted cone survival of normal and low glucose controls for individual well plates (**D**) and organoid batches (**E**), mean  $\pm$  se. Top: 3D-count. Bottom: MIP-count. **F:** Adjusted cone survival of all normal and low glucose controls. Left: 3D-count. Right: MIP-count. **G:** Adjusted cone survival of normal and low glucose controls for individual experiments (groups of 5 well plates containing all replicates for compounds) using the 3D-additive-count algorithm, mean  $\pm$  se.

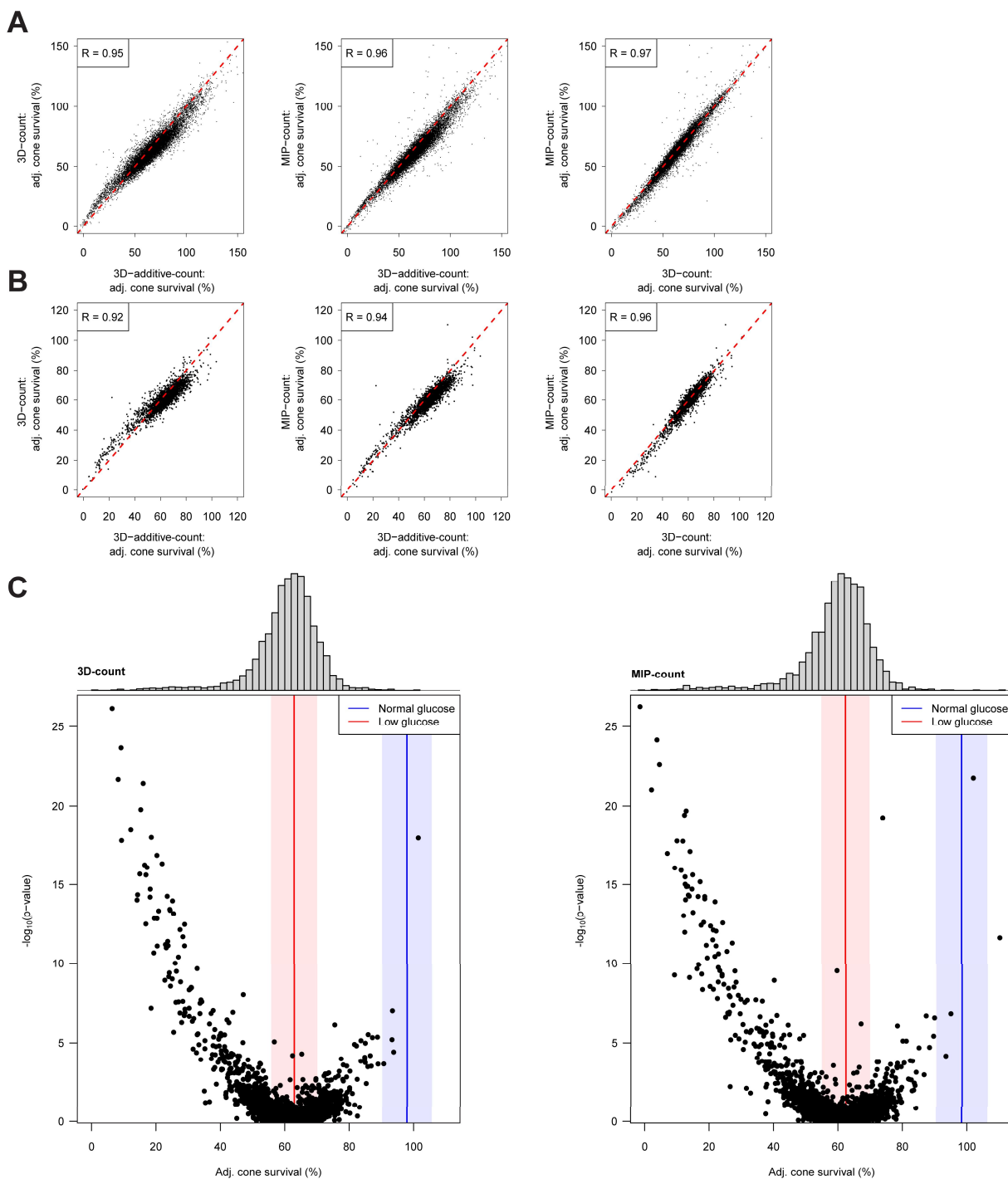


**Figure S3: Primary screen: comparison of different quantifications.**

**A-B:** Comparison of different quantification methods. Comparing either adjusted cone survival values of individual organoids (**A**) or the median of adjusted cone survival values for individual compounds (**B**). The dotted red line represents the unity line and ‘R’ denotes the Pearson’s correlation coefficient. **C:** Effect of compounds on cone survival in the primary screen. Left: 3D-count. Right: MIP-count. Each dot corresponds to the effect of one compound, with the median of the adjusted cone survival of five human retinal organoids on the x-axis and the p-value comparing the cone survival in the compound and in low glucose on the y-axis. The

median (line) and the interquartile range (shaded area) of normal (blue) and low (red) glucose controls are indicated. Top: the distribution of median adjusted cone survival for the compounds.

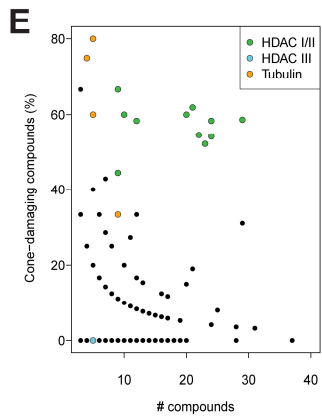
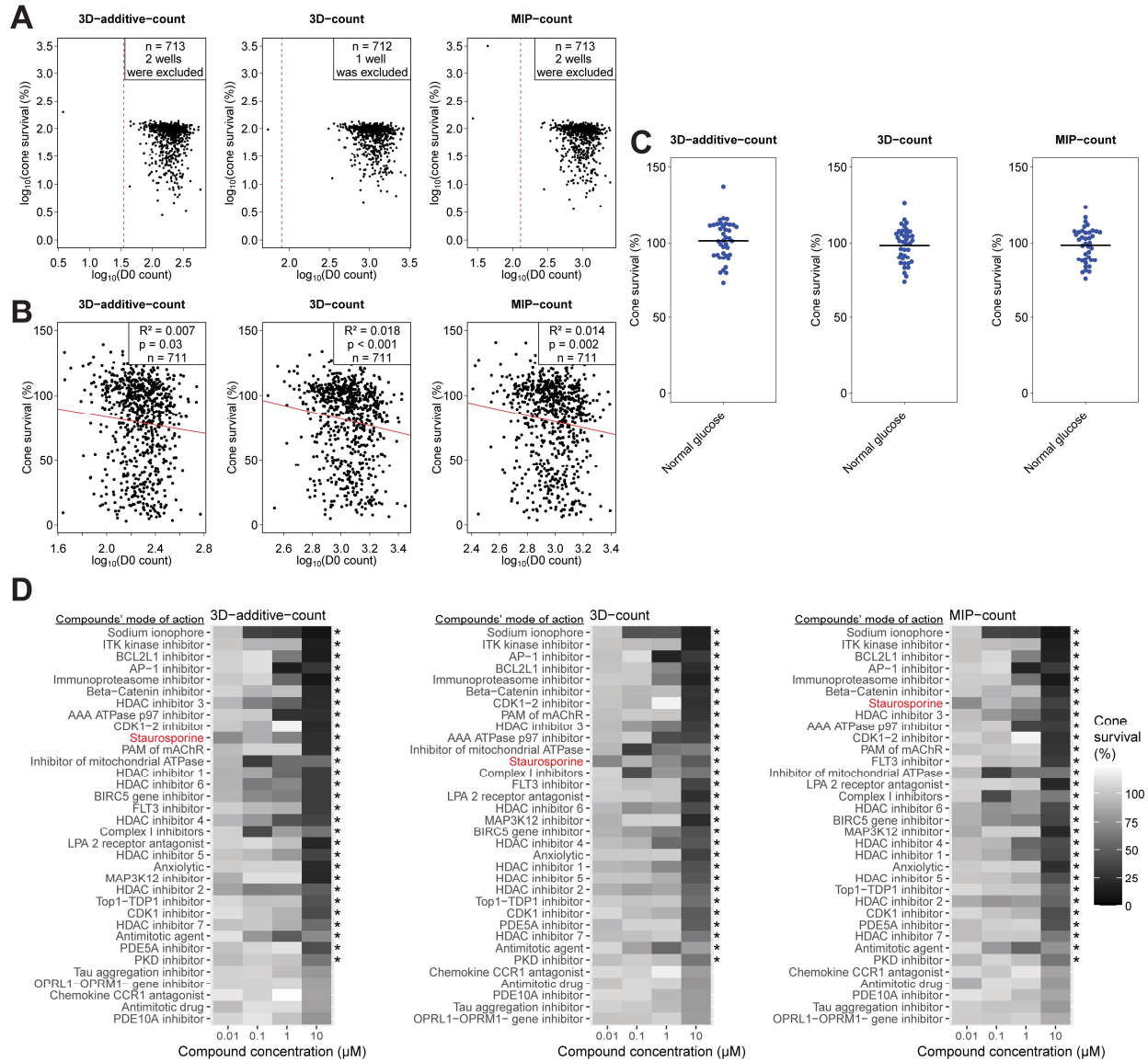


**Figure S4: Secondary screen for cone-damaging compounds: analysis.**

**A:** Thresholding of data for the secondary screen of cone-damaging compounds based on counts at D0 for all quantification methods. The dotted red line indicates the threshold beyond which wells are included in the analysis. **B:** Effect of D0 count. Cone survival and the logarithm of the cone count at D0, fitted with a linear model. The regression line is shown in red and the summary statistics are displayed at top right. **C:** Normal glucose controls with indicated means for all three quantification methods. **D:** Summary of the effects of all cone-damaging compounds tested in the secondary screen. The positive control Staurosporine is indicated in red. Compounds are sorted by the minimum p-value across all concentrations, with the smallest p-value at the top. Significant compounds (at any concentration) are marked with \*, denoting a p-value < 0.05 (after Benjamini Hochberg correction for multiple testing). **E:** Target analysis showing the number of compounds against the fraction of compounds having a significant cone-damaging effect (p-values < 0.05, after Benjamini Hochberg correction for multiple testing) for all targets with more than two compounds.



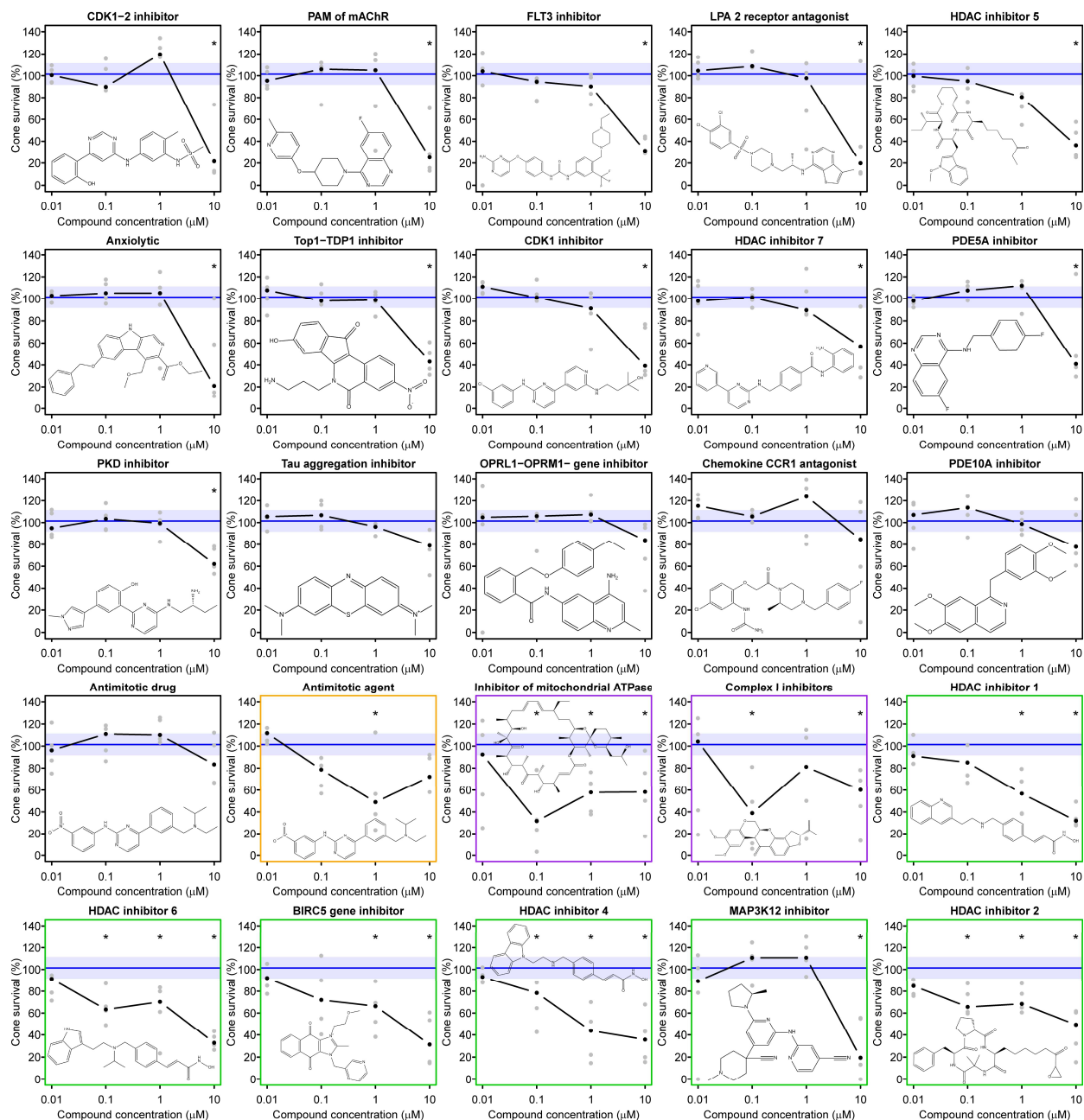


**Figure S5: Secondary screen for cone-damaging compounds: dose-response curves.**

Dose-response curves of all secondary screen cone-damaging compounds, excluding those depicted in Figure 3D. The compounds are ordered based on their respective clusters from Figure 3C and minimum p-values. Black dots denote median cone survival, gray dots represent individual values. The blue line and area indicate median and interquartile range of the normal glucose controls, respectively. The colored frame corresponds to the clusters from Figure 3C. The structure of each compound is illustrated within the plot. Significant compounds and concentrations are marked with \* denoting a  $p$ -value  $< 0.05$  (after Benjamini Hochberg correction for multiple testing).

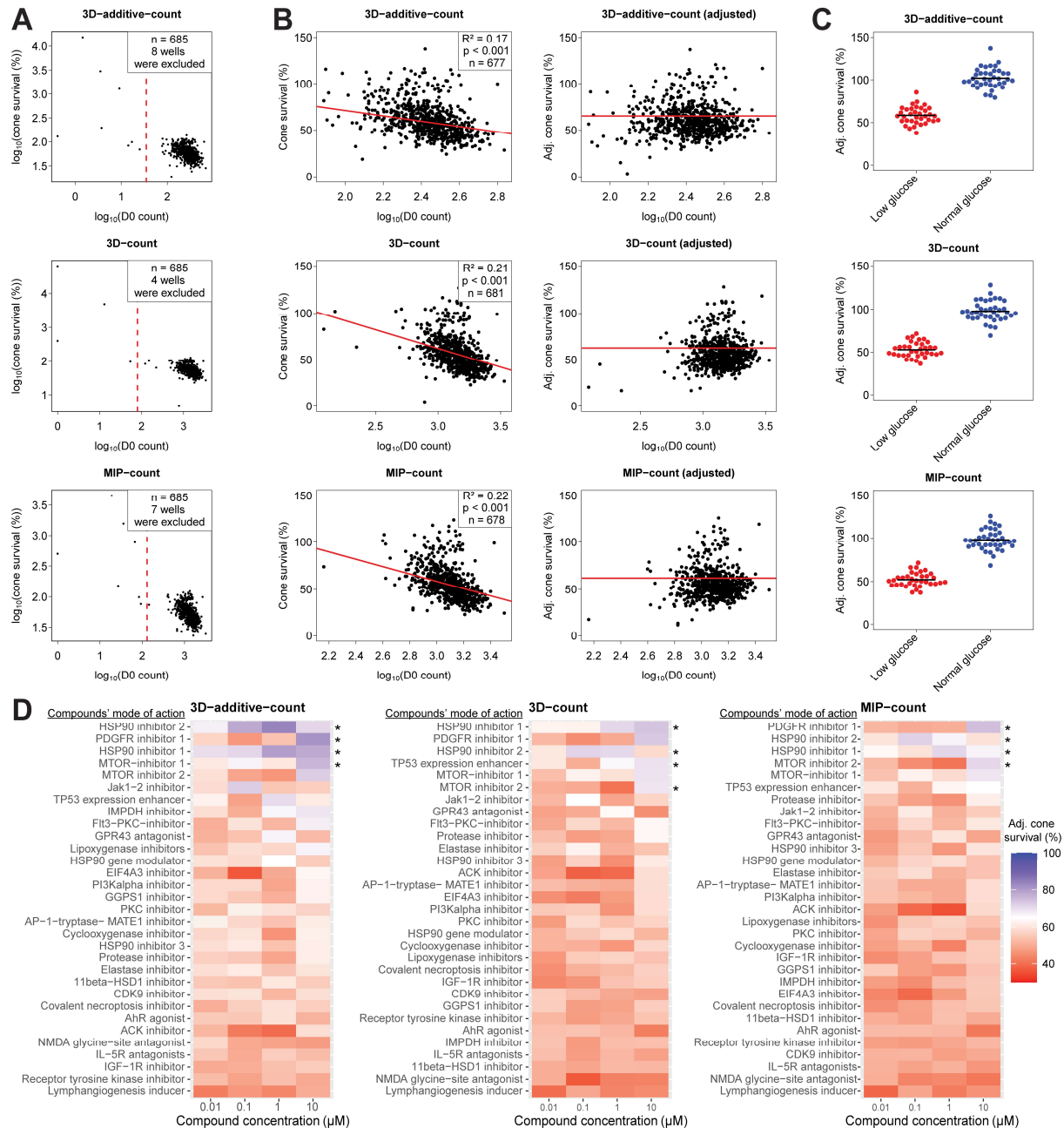


**Figure S6: Secondary screen for cone-saving compounds: analysis.**

**A:** Thresholding of data for the secondary screen of cone-saving compounds based on counts at D0 for all quantification methods. The dotted red line indicates the threshold beyond which wells are included in the analysis. **B:** Adjustment of cone survival values based on D0 counts for all quantification methods. Left: cone survival and the logarithm of the cone counts at D0, fitted with a linear model. Regression line, red; summary statistics, top right corner of each panel. Right: adjusted cone survival and the logarithm of the cone counts at D0 with the transformed regression line. **C:** Adjusted cone survival of all normal and low glucose controls for all quantification methods. **D:** Summary the effects of cone-saving compounds. Compounds are sorted by the maximum median adjusted cone survival. Results are shown for all three quantification methods. Significant compounds are marked with \*, denoting a  $p$ -value  $< 0.05$  (after Benjamini Hochberg correction for multiple testing).

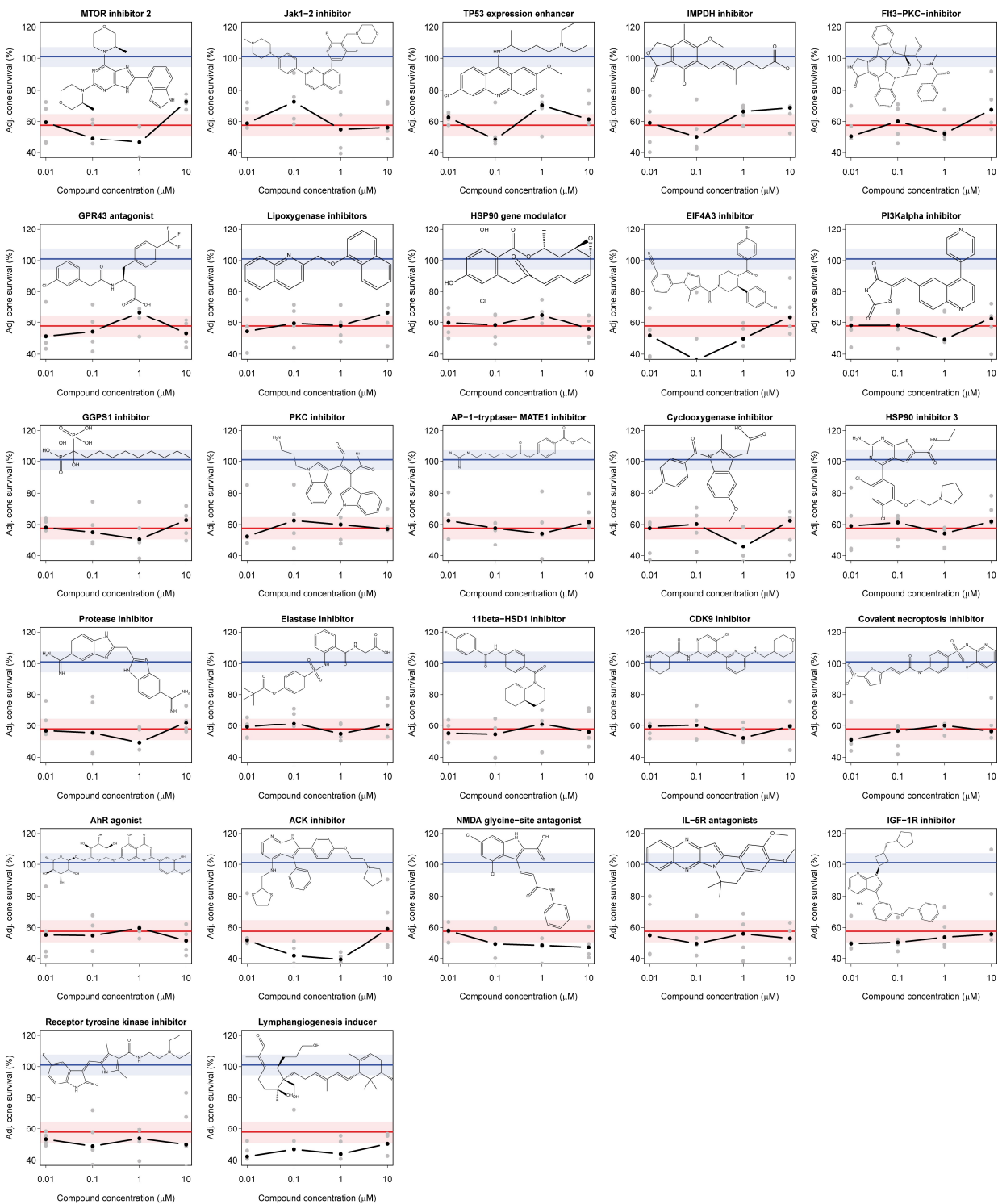


**Figure S7: Secondary screen for cone-saving compounds: dose-response curves.**

Dose-response curves of all secondary screen cone-saving compounds, excluding those depicted in Figure 4B. Compounds are ordered by their maximum adjusted cone survival (most effective concentration). Black dots denote median cone survival, gray dots represent individual values. The median (line) and the interquartile range (shaded area) of normal (blue) and low (red) glucose controls are indicated. The structure of each compound is illustrated within the plot.

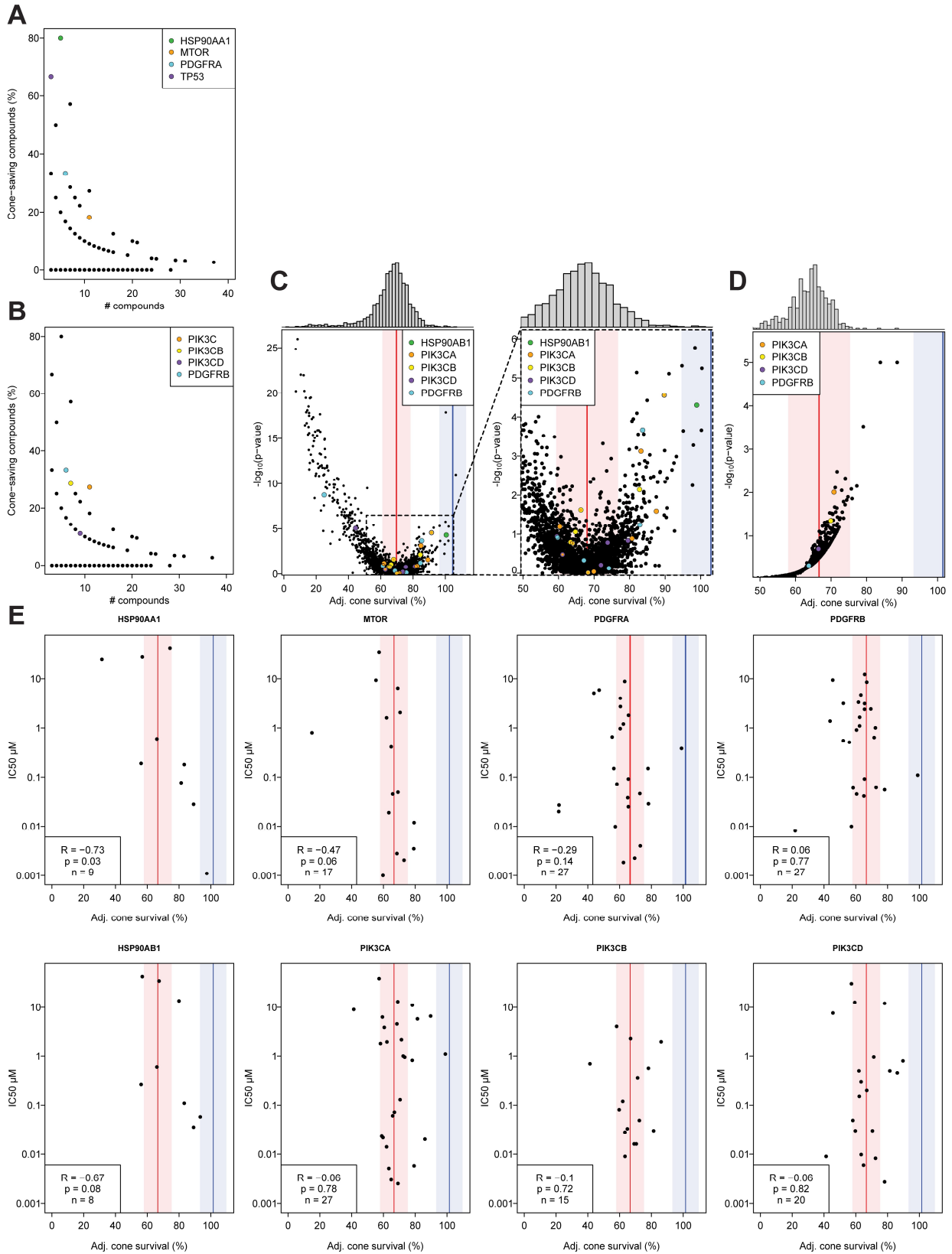


**Figure S8: Target analysis and IC50s.**

**A-B:** Number of compounds and fractions of compounds having a median adjusted cone survival >80% for all targets (with more than two compounds). Indicated targets colored. **C:** Left: adjusted cone survival and p-values in the primary screen. Compound targets are indicated and colored. The median (line) and the interquartile range (shaded area) of normal (blue) and low (red) glucose controls are indicated. Right: zoom-in of plot on the left. **D:** Target analysis of primary screen. The means of the median adjusted cone survival for each target are shown, along with their p-values. Specific targets are indicated. The median and the interquartile range are labeled as in (C). **E:** Median IC50 values for compounds that bind the annotated targets (labeled on top) of cone-saving compounds and their median adjusted cone survival. The median and the interquartile range are labeled as in (C).

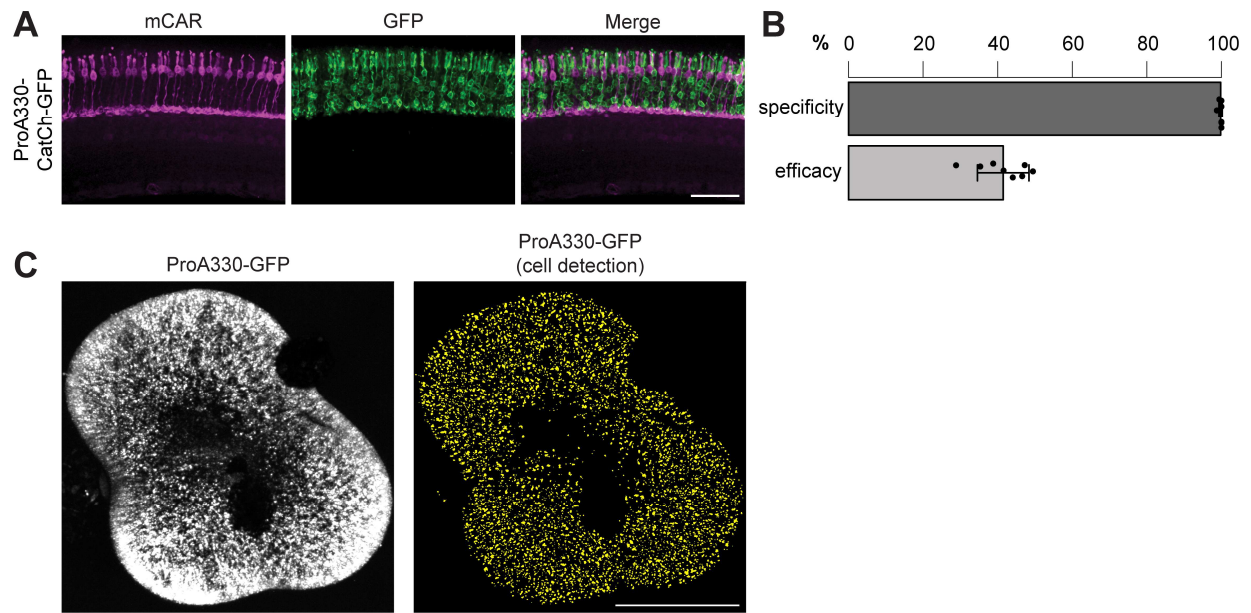


**Figure S9: Rod promoter.**

**A:** Confocal image of sectioned and stained transduced mouse retina (scale bar, 50  $\mu$ m). mCAR, magenta; CatCh-GFP, green. **B:** Quantification of the specificity and efficacy of rod labeling in mice by ProA330-CatCh-GFP AAV. Rods were identified as being present in the photoreceptor layer but negative for the cone-marker mCAR. Results are shown as mean  $\pm$  sd. **C:** Left: example image of a ProA330-GFP AAV-transduced human retinal organoid. GFP, white. Right: Detected rods of an example human retinal organoid. Detected cells, yellow.

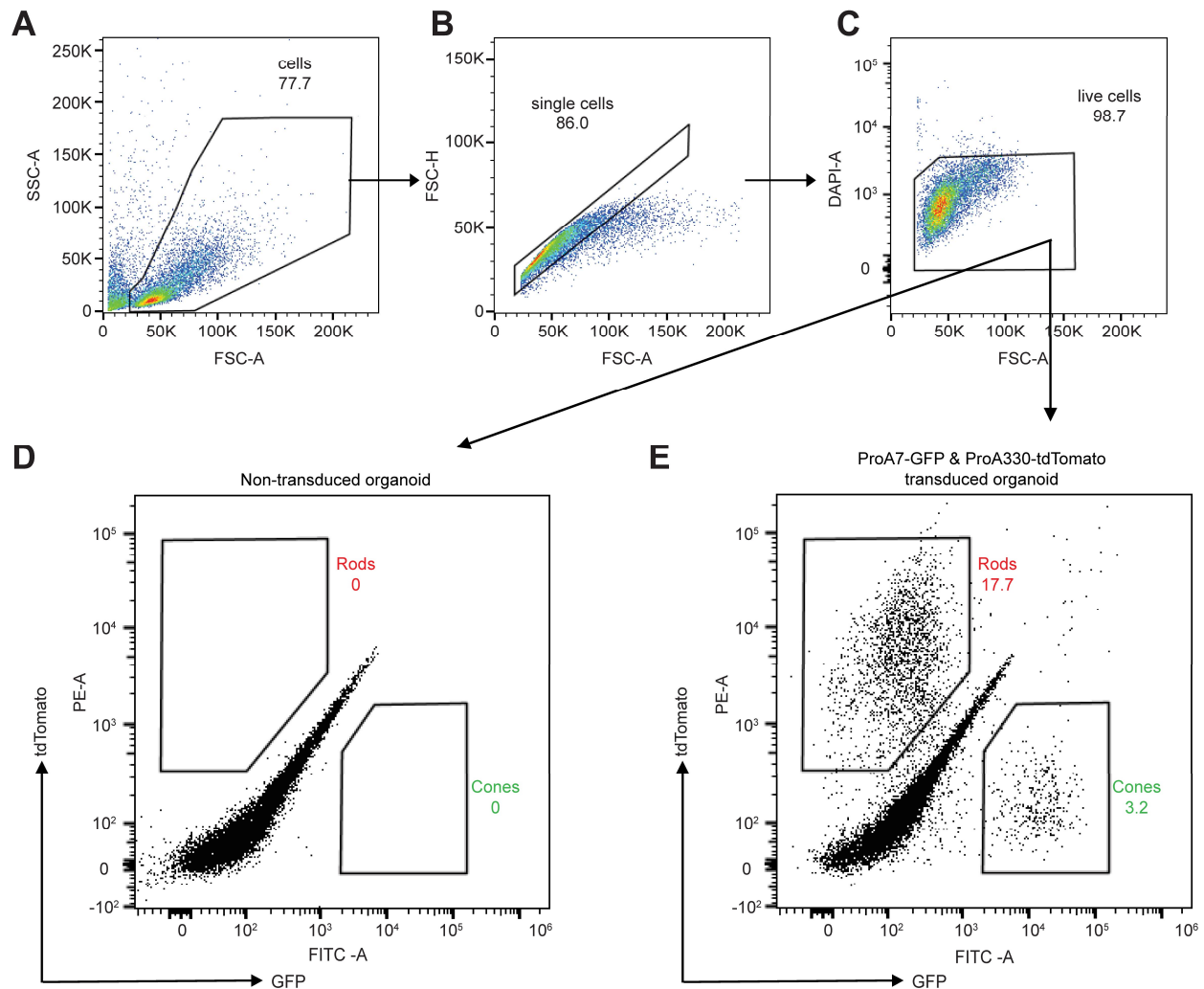


**Figure S10: Fluorescence activated cell sorting (FACS) of photoreceptors.**

Representative FACS density plots from a human retinal organoid co-transduced with ProA7-GFP and ProA330-tdTomato. All numbers are percentages of gated cells. **A:** Forward scatter area (FSC-A) and side scatter area (SSC-A) to filter cells from debris. **B:** FSC-A and forward scatter height (FSC-H) to filter single cells from aggregates. **C:** FSC-A and Hoechst channel (DAPI-A) to sort out living cells. **D-E:** GFP (cone) and tdTomato (rod) positive cells from either non-transduced (D) or co-transduced (E) human retinal organoids.

## REFERENCES

1. Lancaster, M.A., and Knoblich, J.A. (2014). Organogenesis in a dish: Modeling development and disease using organoid technologies. *Science* 345, 1247125. 10.1126/science.1247125.
2. Clevers, H. (2016). Modeling Development and Disease with Organoids. *Cell* 165, 1586–1597. 10.1016/j.cell.2016.05.082.
3. Rossi, G., Manfrin, A., and Lutolf, M.P. (2018). Progress and potential in organoid research. *Nat. Rev. Genet.* 19, 671–687. 10.1038/s41576-018-0051-9.
4. Tang, X.-Y., Wu, S., Wang, D., Chu, C., Hong, Y., Tao, M., Hu, H., Xu, M., Guo, X., and Liu, Y. (2022). Human organoids in basic research and clinical applications. *Signal Transduct. Target. Ther.* 7, 168. 10.1038/s41392-022-01024-9.
5. Chumduri, C., and Turco, M.Y. (2021). Organoids of the female reproductive tract. *J. Mol. Med. Berl. Ger.* 99, 531–553. 10.1007/s00109-020-02028-0.
6. Patricio, D., Santiago, J., Mano, J.F., and Fardilha, M. (2023). Organoids of the male reproductive system: Challenges, opportunities, and their potential use in fertility research. *WIREs Mech. Dis.* 15, e1590. 10.1002/wsbm.1590.
7. Broutier, L., Mastrogiovanni, G., Verstegen, M.M., Francies, H.E., Gavarró, L.M., Bradshaw, C.R., Allen, G.E., Arnes-Benito, R., Sidorova, O., Gaspersz, M.P., et al. (2017). Human primary liver cancer–derived organoid cultures for disease modeling and drug screening. *Nat. Med.* 23, 1424–1435. 10.1038/nm.4438.
8. Toshimitsu, K., Takano, A., Fujii, M., Togasaki, K., Matano, M., Takahashi, S., Kanai, T., and Sato, T. (2022). Organoid screening reveals epigenetic vulnerabilities in human colorectal cancer. *Nat. Chem. Biol.* 18, 605–614. 10.1038/s41589-022-00984-x.
9. Dorgau, B., Georgiou, M., Chaudhary, A., Moya-Molina, M., Collin, J., Queen, R., Hilgen, G., Davey, T., Hewitt, P., Schmitt, M., et al. (2022). Human Retinal Organoids Provide a Suitable Tool for Toxicological Investigations: A Comprehensive Validation Using Drugs and Compounds Affecting the Retina. *Stem Cells Transl. Med.* 11, 159–177. 10.1093/stcltm/szab010.
10. Lukonin, I., Serra, D., Challet Meylan, L., Volkmann, K., Baaten, J., Zhao, R., Meeusen, S., Colman, K., Maurer, F., Stadler, M.B., et al. (2020). Phenotypic landscape of intestinal organoid regeneration. *Nature* 586, 275–280. 10.1038/s41586-020-2776-9.
11. Chen, H.Y., Swaroop, M., Papal, S., Mondal, A.K., Song, H.B., Campello, L., Tawa, G.J., Regent, F., Shimada, H., Nagashima, K., et al. (2023). Reserpine maintains photoreceptor survival in retinal ciliopathy by resolving proteostasis imbalance and ciliogenesis defects. *eLife* 12, e83205. 10.7554/eLife.83205.
12. Srivastava, P.K. (2000). Immunotherapy of human cancer: lessons from mice. *Nat. Immunol.* 1, 363–366. 10.1038/808795.
13. Rivera, J., and Tessarollo, L. (2008). Genetic Background and the Dilemma of Translating Mouse Studies to Humans. *Immunity* 28, 1–4. 10.1016/j.immuni.2007.12.008.



14. Jüttner, J., Szabo, A., Gross-Scherf, B., Morikawa, R.K., Rompani, S.B., Hantz, P., Szikra, T., Esposti, F., Cowan, C.S., Bharioke, A., et al. (2019). Targeting neuronal and glial cell types with synthetic promoter AAVs in mice, non-human primates and humans. *Nat. Neurosci.* 22, 1345–1356. 10.1038/s41593-019-0431-2.
15. Macosko, E.Z., Basu, A., Satija, R., Nemes, J., Shekhar, K., Goldman, M., Tirosh, I., Bialas, A.R., Kamitaki, N., Martersteck, E.M., et al. (2015). Highly Parallel Genome-wide Expression Profiling of Individual Cells Using Nanoliter Droplets. *Cell* 161, 1202–1214. 10.1016/j.cell.2015.05.002.
16. Zeng, H., and Sanes, J.R. (2017). Neuronal cell-type classification: challenges, opportunities and the path forward. *Nat. Rev. Neurosci.* 18, 530–546. 10.1038/nrn.2017.85.
17. Yao, Z., Van Velthoven, C.T.J., Kunst, M., Zhang, M., McMillen, D., Lee, C., Jung, W., Goldy, J., Abdelhak, A., Baker, P., et al. (2023). A high-resolution transcriptomic and spatial atlas of cell types in the whole mouse brain (Neuroscience) 10.1101/2023.03.06.531121.
18. Fu, H., Hardy, J., and Duff, K.E. (2018). Selective vulnerability in neurodegenerative diseases. *Nat. Neurosci.* 21, 1350–1358. 10.1038/s41593-018-0221-2.
19. Raza, C., Anjum, R., and Shakeel, N.U.A. (2019). Parkinson’s disease: Mechanisms, translational models and management strategies. *Life Sci.* 226, 77–90. 10.1016/j.lfs.2019.03.057.
20. McColgan, P., and Tabrizi, S.J. (2018). Huntington’s disease: a clinical review. *Eur. J. Neurol.* 25, 24–34. 10.1111/ene.13413.
21. Dowling, J.E. (2012). *The Retina: An Approachable Part of the Brain, Revised Edition* 2 edition. (Belknap Press: An Imprint of Harvard University Press).
22. Cowan, C.S., Renner, M., De Gennaro, M., Gross-Scherf, B., Goldblum, D., Hou, Y., Munz, M., Rodrigues, T.M., Krol, J., Szikra, T., et al. (2020). Cell Types of the Human Retina and Its Organoids at Single-Cell Resolution. *Cell* 182, 1623-1640.e34. 10.1016/j.cell.2020.08.013.
23. Yan, W., Peng, Y.-R., van Zyl, T., Regev, A., Shekhar, K., Juric, D., and Sanes, J.R. (2020). Cell Atlas of The Human Fovea and Peripheral Retina. *Sci. Rep.* 10, 9802. 10.1038/s41598-020-66092-9.
24. Grünert, U., and Martin, P.R. (2020). Cell types and cell circuits in human and non-human primate retina. *Prog. Retin. Eye Res.*, 100844. 10.1016/j.preteyeres.2020.100844.
25. Zeitz, C., Robson, A.G., and Audo, I. (2015). Congenital stationary night blindness: An analysis and update of genotype–phenotype correlations and pathogenic mechanisms. *Prog. Retin. Eye Res.* 45, 58–110. 10.1016/j.preteyeres.2014.09.001.
26. Parmeggiani, F. (2011). Clinics, epidemiology and genetics of retinitis pigmentosa. *Curr. Genomics* 12, 236–237. 10.2174/138920211795860080.
27. Vyawahare, H., and Shinde, P. (2022). Age-Related Macular Degeneration: Epidemiology, Pathophysiology, Diagnosis, and Treatment. *Cureus* 14, e29583. 10.7759/cureus.29583.
28. Fleckenstein, M., Keenan, T.D.L., Guymer, R.H., Chakravarthy, U., Schmitz-Valckenberg, S., Klaver, C.C., Wong, W.T., and Chew, E.Y. (2021). Age-related macular degeneration. *Nat. Rev. Dis. Primer* 7, 31. 10.1038/s41572-021-00265-2.

29. Humphries, P., Kenna, P., and Farrar, G. (1992). On the molecular genetics of retinitis pigmentosa. *Science* 256, 804–808. 10.1126/science.1589761.
30. Ferrari, S., Di Iorio, E., Barbaro, V., Ponzin, D., Sorrentino, F.S., and Parmeggiani, F. (2011). Retinitis pigmentosa: genes and disease mechanisms. *Curr. Genomics* 12, 238–249. 10.2174/138920211795860107.
31. Narayan, D.S., Wood, J.P.M., Chidlow, G., and Casson, R.J. (2016). A review of the mechanisms of cone degeneration in retinitis pigmentosa. *Acta Ophthalmol. (Copenh.)* 94, 748–754. 10.1111/aos.13141.
32. Aït-Ali, N., Fridlich, R., Millet-Puel, G., Clérin, E., Delalande, F., Jaillard, C., Blond, F., Perrocheau, L., Reichman, S., Byrne, L.C., et al. (2015). Rod-derived cone viability factor promotes cone survival by stimulating aerobic glycolysis. *Cell* 161, 817–832. 10.1016/j.cell.2015.03.023.
33. Amamoto, R., Wallick, G.K., and Cepko, C.L. (2022). Retinoic acid signaling mediates peripheral cone photoreceptor survival in a mouse model of retina degeneration. *eLife* 11, e76389. 10.7554/eLife.76389.
34. Byrne, L.C., Dalkara, D., Luna, G., Fisher, S.K., Clérin, E., Sahel, J.-A., Lévillard, T., and Flannery, J.G. (2015). Viral-mediated RdCVF and RdCVFL expression protects cone and rod photoreceptors in retinal degeneration. *J. Clin. Invest.* 125, 105–116. 10.1172/JCI65654.
35. Lévillard, T., Mohand-Said, S., Lorentz, O., Hicks, D., Fintz, A.-C., Clérin, E., Simonutti, M., Forster, V., Cavusoglu, N., Chalmel, F., et al. (2004). Identification and characterization of rod-derived cone viability factor. *Nat. Genet.* 36, 755–759. 10.1038/ng1386.
36. Mohand-Said, S., Deudon-Combe, A., Hicks, D., Simonutti, M., Forster, V., Fintz, A.C., Lévillard, T., Dreyfus, H., and Sahel, J.A. (1998). Normal retina releases a diffusible factor stimulating cone survival in the retinal degeneration mouse. *Proc. Natl. Acad. Sci. U. S. A.* 95, 8357–8362. 10.1073/pnas.95.14.8357.
37. Pardue, M.T., and Allen, R.S. (2018). Neuroprotective strategies for retinal disease. *Prog. Retin. Eye Res.* 65, 50–76. 10.1016/j.preteyeres.2018.02.002.
38. Punzo, C., Kornacker, K., and Cepko, C.L. (2009). Stimulation of the insulin/mTOR pathway delays cone death in a mouse model of retinitis pigmentosa. *Nat. Neurosci.* 12, 44–52. 10.1038/nn.2234.
39. Sahel, J.-A., and Lévillard, T. (2018). Maintaining Cone Function in Rod-Cone Dystrophies. *Adv. Exp. Med. Biol.* 1074, 499–509. 10.1007/978-3-319-75402-4\_62.
40. Wang, S.K., Xue, Y., and Cepko, C.L. (2020). Microglia modulation by TGF- $\beta$ 1 protects cones in mouse models of retinal degeneration. *J. Clin. Invest.* 130, 4360–4369. 10.1172/JCI136160.
41. Wang, S.K., Xue, Y., and Cepko, C.L. (2021). Augmentation of CD47/SIRP $\alpha$  signaling protects cones in genetic models of retinal degeneration. *JCI Insight* 6, e150796. 10.1172/jci.insight.150796.
42. Wang, S.K., Xue, Y., Rana, P., Hong, C.M., and Cepko, C.L. (2019). Soluble CX3CL1 gene therapy improves cone survival and function in mouse models of retinitis pigmentosa. *Proc. Natl. Acad. Sci. U. S. A.* 116, 10140–10149. 10.1073/pnas.1901787116.
43. Xue, Y., and Cepko, C.L. (2023). Gene Therapies for Retinitis Pigmentosa that Target Glucose Metabolism. *Cold Spring Harb. Perspect. Med.*, a041289. 10.1101/cshperspect.a041289.

44. Xue, Y., Sun, X., Wang, S.K., Collin, G.B., Kefalov, V.J., and Cepko, C.L. (2023). Chromophore supply modulates cone function and survival in retinitis pigmentosa mouse models. *Proc. Natl. Acad. Sci. U. S. A.* *120*, e2217885120. 10.1073/pnas.2217885120.
45. Xue, Y., Wang, S.K., Rana, P., West, E.R., Hong, C.M., Feng, H., Wu, D.M., and Cepko, C.L. (2021). AAV-Txnip prolongs cone survival and vision in mouse models of retinitis pigmentosa. *eLife* *10*, e66240. 10.7554/eLife.66240.
46. Yang, Y., Mohand-Said, S., Danan, A., Simonutti, M., Fontaine, V., Clerin, E., Picaud, S., Léveillard, T., and Sahel, J.-A. (2009). Functional cone rescue by RdCVF protein in a dominant model of retinitis pigmentosa. *Mol. Ther. J. Am. Soc. Gene Ther.* *17*, 787–795. 10.1038/mt.2009.28.
47. Samardzija, M., Corna, A., Gomez-Sintes, R., Jarboui, M.A., Armento, A., Roger, J.E., Petridou, E., Haq, W., Paquet-Durand, F., Zrenner, E., et al. (2021). HDAC inhibition ameliorates cone survival in retinitis pigmentosa mice. *Cell Death Differ.* *28*, 1317–1332. 10.1038/s41418-020-00653-3.
48. Trifunović, D., Arango-Gonzalez, B., Comitato, A., Barth, M., Del Amo, E.M., Kulkarni, M., Sahaboglu, A., Hauck, S.M., Urti, A., Arsenijevic, Y., et al. (2016). HDAC inhibition in the cpfl1 mouse protects degenerating cone photoreceptors in vivo. *Hum. Mol. Genet.* *25*, 4462–4472. 10.1093/hmg/ddw275.
49. Sundaramurthi, H., Roche, S.L., Grice, G.L., Moran, A., Dillion, E.T., Campiani, G., Nathan, J.A., and Kennedy, B.N. (2020). Selective Histone Deacetylase 6 Inhibitors Restore Cone Photoreceptor Vision or Outer Segment Morphology in Zebrafish and Mouse Models of Retinal Blindness. *Front. Cell Dev. Biol.* *8*, 689. 10.3389/fcell.2020.00689.
50. Eiraku, M., Takata, N., Ishibashi, H., Kawada, M., Sakakura, E., Okuda, S., Sekiguchi, K., Adachi, T., and Sasai, Y. (2011). Self-organizing optic-cup morphogenesis in three-dimensional culture. *Nature* *472*, 51–56. 10.1038/nature09941.
51. Nakano, T., Ando, S., Takata, N., Kawada, M., Muguruma, K., Sekiguchi, K., Saito, K., Yonemura, S., Eiraku, M., and Sasai, Y. (2012). Self-Formation of Optic Cups and Storable Stratified Neural Retina from Human ESCs. *Cell Stem Cell* *10*, 771–785. 10.1016/j.stem.2012.05.009.
52. Zhong, X., Gutierrez, C., Xue, T., Hampton, C., Vergara, M.N., Cao, L.-H., Peters, A., Park, T.S., Zambidis, E.T., Meyer, J.S., et al. (2014). Generation of three-dimensional retinal tissue with functional photoreceptors from human iPSCs. *Nat. Commun.* *5*, 4047. 10.1038/ncomms5047.
53. Saha, A., Capowski, E., Fernandez Zepeda, M.A., Nelson, E.C., Gamm, D.M., and Sinha, R. (2022). Cone photoreceptors in human stem cell-derived retinal organoids demonstrate intrinsic light responses that mimic those of primate fovea. *Cell Stem Cell* *29*, 487–489. 10.1016/j.stem.2022.02.003.
54. Canham, S.M., Wang, Y., Cornett, A., Auld, D.S., Baeschlin, D.K., Patoor, M., Skaanderup, P.R., Honda, A., Llamas, L., Wendel, G., et al. (2020). Systematic Chemogenetic Library Assembly. *Cell Chem. Biol.* *27*, 1124–1129. 10.1016/j.chembiol.2020.07.004.
55. Chan, K.Y., Jang, M.J., Yoo, B.B., Greenbaum, A., Ravi, N., Wu, W.-L., Sánchez-Guardado, L., Lois, C., Mazmanian, S.K., Deverman, B.E., et al. (2017). Engineered AAVs for efficient noninvasive gene delivery to the central and peripheral nervous systems. *Nat. Neurosci.* *20*, 1172–1179. 10.1038/nn.4593.

56. Yeo, J.H.M., Lo, J.C.Y., Nissom, P.M., and Wong, V.V.T. (2006). Glutamine or Glucose Starvation in Hybridoma Cultures Induces Death Receptor and Mitochondrial Apoptotic Pathways. *Biotechnol. Lett.* *28*, 1445–1452. 10.1007/s10529-006-9110-y.
57. Strebel, A., Harr, T., Bachmann, F., Wernli, M., and Erb, P. (2001). Green fluorescent protein as a novel tool to measure apoptosis and necrosis. *Cytometry* *43*, 126–133. 10.1002/1097-0320(20010201)43:2<126::AID-CYTO1027>3.0.CO;2-J.
58. Steff, A.-M., Fortin, M., Arguin, C., and Hugo, P. (2001). Detection of a decrease in green fluorescent protein fluorescence for the monitoring of cell death: An assay amenable to high-throughput screening technologies. *Cytometry* *45*, 237–243. 10.1002/1097-0320(20011201)45:4<237::AID-CYTO10024>3.0.CO;2-J.
59. Fortin, M., Steff, A.-M., and Hugo, P. (2005). High-Throughput Technology: Green Fluorescent Protein to Monitor Cell Death. In *Chemosensitivity* (Humana Press), pp. 121–138. 10.1385/1-59259-869-2:121.
60. Karaman, M.W., Herrgard, S., Treiber, D.K., Gallant, P., Atteridge, C.E., Campbell, B.T., Chan, K.W., Ciceri, P., Davis, M.I., Edeen, P.T., et al. (2008). A quantitative analysis of kinase inhibitor selectivity. *Nat. Biotechnol.* *26*, 127–132. 10.1038/nbt1358.
61. Belmokhtar, C.A., Hillion, J., and Ségal-Bendirdjian, E. (2001). Staurosporine induces apoptosis through both caspase-dependent and caspase-independent mechanisms. *Oncogene* *20*, 3354–3362. 10.1038/sj.onc.1204436.
62. Chen, B., and Cepko, C.L. (2007). Requirement of histone deacetylase activity for the expression of critical photoreceptor genes. *BMC Dev. Biol.* *7*, 78. 10.1186/1471-213X-7-78.
63. Chen, B., and Cepko, C.L. (2009). HDAC4 regulates neuronal survival in normal and diseased retinas. *Science* *323*, 256–259. 10.1126/science.1166226.
64. Eckschlager, T., Plch, J., Stiborova, M., and Hrabeta, J. (2017). Histone Deacetylase Inhibitors as Anticancer Drugs. *Int. J. Mol. Sci.* *18*, 1414. 10.3390/ijms18071414.
65. SparingVision (2023). A Phase I/II Study to Assess the Safety and Tolerability of a Single Subretinal Administration of SPVN06 Gene Therapy in Subjects With Rod-Cone Dystrophy (RCD) Due to a Mutation in the RHO, PDE6A, or PDE6B Gene (clinicaltrials.gov).
66. Whalley, K. (2009). Cones go hungry. *Nat. Rev. Neurosci.* *10*, 84–85. 10.1038/nrn2574.
67. Bovolenta, P., and Cisneros, E. (2009). Retinitis pigmentosa: cone photoreceptors starving to death. *Nat. Neurosci.* *12*, 5–6. 10.1038/nrn0109-5.
68. Krol, J., and Roska, B. (2015). Rods Feed Cones to Keep them Alive. *Cell* *161*, 706–708. 10.1016/j.cell.2015.04.031.
69. Aguilà, M., Bevilacqua, D., McCulley, C., Schwarz, N., Athanasiou, D., Kanuga, N., Novoselov, S.S., Lange, C.A.K., Ali, R.R., Bainbridge, J.W., et al. (2014). Hsp90 inhibition protects against inherited retinal degeneration. *Hum. Mol. Genet.* *23*, 2164–2175. 10.1093/hmg/ddt613.
70. Kanamaru, C., Yamada, Y., Hayashi, S., Matsushita, T., Suda, A., Nagayasu, M., Kimura, K., and Chiba, S. (2014). Retinal toxicity induced by small-molecule Hsp90 inhibitors in beagle dogs. *J. Toxicol. Sci.* *39*, 59–69. 10.2131/jts.39.59.

71. Cronin, T., Vandenberghe, L.H., Hantz, P., Juttner, J., Reimann, A., Kacsó, Á., Huckfeldt, R.M., Busskamp, V., Kohler, H., Lagali, P.S., et al. (2014). Efficient transduction and optogenetic stimulation of retinal bipolar cells by a synthetic adeno-associated virus capsid and promoter. *EMBO Mol. Med.* 6, 1175–1190. 10.15252/emmm.201404077.
72. Hahaut, V., Pavlinic, D., Carbone, W., Schuierer, S., Balmer, P., Quinodoz, M., Renner, M., Roma, G., Cowan, C.S., and Picelli, S. (2022). Fast and highly sensitive full-length single-cell RNA sequencing using FLASH-seq. *Nat. Biotechnol.* 40, 1447–1451. 10.1038/s41587-022-01312-3.
73. Hahaut, V., Picelli, S., Siwicki, RA. (2023). Bulk FLASH-seq. protocols.io <https://dx.doi.org/10.17504/protocols.io.3byl4jynolo5/v1>.
74. Na, D., Son, H., and Gsponer, J. (2014). Categorizer: a tool to categorize genes into user-defined biological groups based on semantic similarity. *BMC Genomics* 15, 1091. 10.1186/1471-2164-15-1091.
75. Mendez, D., Gaulton, A., Bento, A.P., Chambers, J., De Veij, M., Félix, E., Magariños, M.P., Mosquera, J.F., Mutowo, P., Nowotka, M., et al. (2019). ChEMBL: towards direct deposition of bioassay data. *Nucleic Acids Res.* 47, D930–D940. 10.1093/nar/gky1075.

## **6 Discussion and outlook**

This study presents the first large-scale drug screen using human organoids. We hope that the process and results will act as a comprehensive guide for researchers embarking on similar ventures. We conducted this screening specifically to probe into the mechanisms of cone degeneration and have identified compounds that exert protective effects on cones as well as those that exacerbate the damage. Beyond the actual effects of the compounds, the identities of their targets provide valuable insights into the intricate processes of cone degeneration.

### **6.1 Organoids for drug discovery screening**

Numerous organoid systems are currently under development with the central aim to enhance their compatibility with automation and high-throughput screening (Driehuis et al. 2020; Durens et al. 2020; Spirig and Renner 2023). However, the effectiveness and the superiority of organoid-based screens over conventional 2D culture screens remain ambiguous. Typically, organoid cultures entail higher costs, demand more time, require more complex readouts, and yield results with greater variability than 2D cultures. However, the potential superior quality of the results should, with time, justify the inclusion of organoids as a standard component in drug discovery pipelines.

Conventional primary phenotypic drug screens, which can assess thousands of distinct compounds, significantly reduce the pool of potential drug candidates. The selected candidates are subjected subsequently to multiple rounds of retesting and are evaluated in alternative model systems to ensure their efficacy and safety before consideration for clinical application. As a result, the impact of including false positives is less serious than overlooking potential candidates or false negatives. Utilizing more complex 3D models, such as organoids, in the first phase of drug screening would only be advantageous if organoid systems generate fewer false negatives than standard 2D cultures. If this is not the case, then it would be more prudent to incorporate organoids at a later stage in the discovery process. In contrast, the use of organoids is justifiable and advantageous when suitable 2D culture systems for specific cell types are lacking or when specific targets are only expressed in organoids. Although it is plausible to assume that organoids, being closer to the animal

physiology than 2D-cultures, will reveal more relevant drug candidates, future research will show whether such candidates could have been identified in a primary screen using simpler models.

Prior to our study, screenings were conducted with mouse intestinal organoids or cells derived from mouse retinal organoids (Lukonin et al. 2020; Chen et al. 2023). Despite the early availability of human organoid systems, researchers have opted to use mouse organoids due to their faster development (3-4 weeks compared to 6-9 months to reach photoreceptor maturation), ease of handling, and the consequent facilitation of screening procedures (Chen et al. 2016; Cowan et al. 2020). Similar questions emerge when conducting primary screens with mouse rather than human organoids about the comparability of potential hits and the occurrence of false negatives. The differences in drug-screening responses between human and mouse organoids is a critical area for future research.

In the context of the present study, re-evaluation of the identified hits and control negatives using human retinal organoids, followed by testing in corresponding mouse organoid and 2D cell culture assays, would directly clarify the value of primary screens in complex human model systems.

Although primary screenings with organoids may not always offer significant advantages, it is prudent to utilize human organoids in later stages of drug discovery. Typically, preclinical drug candidates are evaluated using animal models and integrating human organ-like structures at this point could reduce failures during clinical trials. However, sole reliance on in vitro human models in preclinical studies is not currently viable. Organoids are still significantly flawed: they are typically not innervated or vascularized and do not interact with other organs. While future progress may address these shortcomings, substantial research is necessary to ascertain whether organoids can accurately forecast patient reaction to a novel treatment. In cancer research, several studies have demonstrated that personalized cancer organoids can predict patient responses to therapy with a high degree of accuracy (de Witte et al. 2020; Yao et al. 2020; Hu et al. 2021). How other organoids predict patient responses should be investigated in the future.

## **6.2 Organoids to predict side effects**

Our study assessed the detrimental effects of compounds on cone photoreceptors. The emergence of retinal and ocular toxicity poses substantial hurdles in the advancement of new medicinal treatments, as vision loss is seldom an acceptable compromise (Handelman et al. 1983). We have identified compounds detrimental to cone photoreceptors and pinpointed their targets. Nevertheless, the specificity of the toxicity of these compounds for cones alone remains uncertain. It is possible that such compounds could cause broader cytotoxic effects that also impact on other cell types. Determining this specificity is not straightforward, although a starting point could involve retesting the outcome of the toxic compounds against a set of inactive controls on diverse cell types.

The degree to which organoid models surpass simpler 2D models and/or animal models in predicting side effects within the drug development process remains uncertain. Just as in drug discovery, comparative studies of these model systems are imperative to assess the relevance of organoids in preclinical safety evaluations. A strategic approach would be to gather information on side effects from clinical data and examine whether these can be anticipated by various model systems, including organoids.

## **6.3 Limitations of human retinal organoids**

Human retinal organoids closely replicate various aspects of their *in vivo* counterparts but significant differences remain. Notably, while most neuronal cell types develop within these organoids, retinal ganglion cells deteriorate and are nearly absent by the time photoreceptors mature at around 30 weeks, likely due to the absence of target tissue for ganglion cell axons (Zhong et al. 2014; Cowan et al. 2020). Efforts to integrate brain organoids with retinal organoids have shown some promise in potentially prolonging ganglion cell viability (Fligor et al. 2021), but current retinal organoids are not comprehensive models of the neuronal retina or the optic nerve.



Furthermore, RPE cells form on top of the organoids but are not positioned to interact directly with photoreceptors and hence do not fully contribute to photoreceptor maintenance. This situation is being approached by the development of organ-on-a-chip models that position retinal organoids over 2D-cultured RPE, which allows limited interaction between photoreceptors and RPE cells (Achberger et al. 2019). However, these integrated systems are still in early stages of optimization and have seen limited application so far. Thus organoids fall short as models of the RPE-photoreceptor interactions that are critical in numerous degenerative conditions.

Retinal organoids also generally lack microglia, which are implicated in photoreceptor degeneration. Methods to incorporate microglia into retinal organoids are pivotal for accurately modeling retinal degenerative diseases and have been achieved with some success (Chichagova et al. 2023). Finally, the inner retinal layers *in vivo* are oxygenated and nourished through their vascular network (Lutty and McLeod 2018), but this feature is not present in retinal organoids and may be critical for studying the biodistribution of compounds within the retina. Ongoing research into vascularizing organoid models may soon extend to include retinal organoids (Sun et al. 2022).

One further consideration with retinal organoids is that they currently replicate the characteristics of fetal or very young retinas (Sridhar et al. 2020). Consequently, this may present challenges in modeling degenerative diseases that typically manifest later in life.

Retinal organoids clearly hold considerable promise as a model system but are not yet optimal. Efforts to enhance organoid cultures to reflect the corresponding *in vivo* organ more accurately are underway and will potentially elevate the value of organoids in preclinical research.

#### **6.4 CS-KI-1 and CS-KI-2 as potential cone-protective agents**

A significant result of the present study is the identification of CS-KI-1 and CS-KI-2 as potential neuroprotective agents for cones. While these compounds show promise in protecting cones, their precise mechanisms of action remain elusive. Our findings substantially contradict the involvement of annotated targets, specifically MTOR, PDGFRA, and PDGFRB, in mediating their therapeutic effects. Deciphering the mode of action by which CS-KI-1 and CS-KI-2 avert cone

cell death could open new avenues for understanding and halting cone degeneration. An intriguing aspect of our primary screening is the detection of structurally similar but inactive molecules that share targets with CS-KI-1 and CS-KI-2. This discrepancy offers a valuable opportunity for further investigation of the differential activity of these compounds, which may shed light on the true targets involved in cone preservation.

## 7 Concluding remarks

This research presents the outcome of the earliest large-scale drug screening using human organoids. This opens novel pathways of investigation in the field and highlights significant issues. Prior to this study, extensive organoid screenings were confined to less complex cancer organoid systems and were deemed to require further technological advancement to be viable. Our findings demonstrate the practicality of such screening, but also underscore the necessity for further research to standardize the early integration of organoids into the drug discovery process. Organoids present distinct phenotypes and they cannot be approached in the same manner as 2D-cell cultures or animal models; each possess unique merits and limitations. The full potential and the methodologies of organoid use in large-scale screens warrant further exploration.

Nevertheless, our study has led to intriguing discoveries that may contribute to future research. These include insights into HDAC inhibition and its relation to cone toxicity, as well as the identification of CS-KI-1 and CS-KI-2 and their cone-protective properties. Overall, our findings not only enhance understanding of the underlying biology but also promise to contribute to the development of novel therapeutic strategies.

## 8 References

- Aasen DM, Vergara MN. 2020. New Drug Discovery Paradigms for Retinal Diseases: A Focus on Retinal Organoids. *J Ocul Pharmacol Ther.* 36(1):18–24. doi:10.1089/jop.2018.0140.
- Achberger K, Probst C, Haderspeck J, Bolz S, Rogal J, Chuchuy J, Nikolova M, Cora V, Antkowiak L, Haq W, et al. 2019. Merging organoid and organ-on-a-chip technology to generate complex multi-layer tissue models in a human retina-on-a-chip platform. *eLife.* 8:e46188. doi:10.7554/eLife.46188.
- Aït-Ali N, Fridlich R, Millet-Puel G, Clérin E, Delalande F, Jaillard C, Blond F, Perrocheau L, Reichman S, Byrne LC, et al. 2015. Rod-derived cone viability factor promotes cone survival by stimulating aerobic glycolysis. *Cell.* 161(4):817–832. doi:10.1016/j.cell.2015.03.023.
- Arshavsky VY, Burns ME. 2012. Photoreceptor Signaling: Supporting Vision across a Wide Range of Light Intensities. *J Biol Chem.* 287(3):1620–1626. doi:10.1074/jbc.R111.305243.
- Basak O, Beumer J, Wiebrands K, Seno H, Van Oudenaarden A, Clevers H. 2017. Induced Quiescence of Lgr5+ Stem Cells in Intestinal Organoids Enables Differentiation of Hormone-Producing Enteroendocrine Cells. *Cell Stem Cell.* 20(2):177–190.e4. doi:10.1016/j.stem.2016.11.001.
- Beumer J, Artegiani B, Post Y, Reimann F, Gribble F, Nguyen TN, Zeng H, Van Den Born M, Van Es JH, Clevers H. 2018. Enteroendocrine cells switch hormone expression along the crypt-to-villus BMP signalling gradient. *Nat Cell Biol.* 20(8):909–916. doi:10.1038/s41556-018-0143-y.
- Blay V, Tolani B, Ho SP, Arkin MR. 2020. High-Throughput Screening: today’s biochemical and cell-based approaches. *Drug Discov Today.* 25(10):1807–1821. doi:10.1016/j.drudis.2020.07.024.
- Broutier L, Mastrogiovanni G, Verstegen MM, Francies HE, Gavarró LM, Bradshaw CR, Allen GE, Arnes-Benito R, Sidorova O, Gaspersz MP, et al. 2017. Human primary liver cancer–derived organoid cultures for disease modeling and drug screening. *Nat Med.* 23(12):1424–1435. doi:10.1038/nm.4438.
- Burrack AL, Martinov T, Fife BT. 2017. T Cell-Mediated Beta Cell Destruction: Autoimmunity and Alloimmunity in the Context of Type 1 Diabetes. *Front Endocrinol.* 8:343. doi:10.3389/fendo.2017.00343.
- Caprara C, Grimm C. 2012. From oxygen to erythropoietin: Relevance of hypoxia for retinal development, health and disease. *Prog Retin Eye Res.* 31(1):89–119. doi:10.1016/j.preteyeres.2011.11.003.
- Chen HY, Kaya KD, Dong L, Swaroop A. 2016. Three-dimensional retinal organoids from mouse pluripotent stem cells mimic in vivo development with enhanced stratification and rod photoreceptor differentiation. *Mol Vis.* 22:1077–1094.
- Chen HY, Swaroop M, Papal S, Mondal AK, Song HB, Campello L, Tawa GJ, Regent F, Shimada H, Nagashima K, et al. 2023. Reserpine maintains photoreceptor survival in retinal ciliopathy by resolving proteostasis imbalance and ciliogenesis defects. *eLife.* 12:e83205. doi:10.7554/eLife.83205.
- Cheung N, Mitchell P, Wong TY. 2010. Diabetic retinopathy. *The Lancet.* 376(9735):124–136. doi:10.1016/S0140-6736(09)62124-3.
- Chichagova V, Georgiou M, Carter M, Dorgau B, Hilgen G, Collin J, Queen R, Chung G, Ajeian J, Moya-Molina M, et al. 2023. Incorporating microglia-like cells in human induced pluripotent stem cell-derived retinal organoids. *J Cell Mol Med.* 27(3):435–445. doi:10.1111/jcmm.17670.

- Choi J, Iich E, Lee J-H. 2016. Organogenesis of adult lung in a dish: Differentiation, disease and therapy. *Dev Biol.* 420(2):278–286. doi:10.1016/j.ydbio.2016.10.002.
- Chumduri C, Turco MY. 2021. Organoids of the female reproductive tract. *J Mol Med.* 99(4):531–553. doi:10.1007/s00109-020-02028-0.
- Clevers H. 2016. Modeling Development and Disease with Organoids. *Cell.* 165(7):1586–1597. doi:10.1016/j.cell.2016.05.082.
- Clevers H, Watt FM. 2018. Defining Adult Stem Cells by Function, not by Phenotype. *Annu Rev Biochem.* 87(1):1015–1027. doi:10.1146/annurev-biochem-062917-012341.
- Cowan CS, Renner M, De Gennaro M, Gross-Scherf B, Goldblum D, Hou Y, Munz M, Rodrigues TM, Krol J, Szikra T, et al. 2020. Cell Types of the Human Retina and Its Organoids at Single-Cell Resolution. *Cell.* 182(6):1623-1640.e34. doi:10.1016/j.cell.2020.08.013.
- D’Amico DJ. 1994. Diseases of the Retina. *N Engl J Med.* 331(2):95–106. doi:10.1056/NEJM199407143310207.
- Dowling JE. 2012. *The Retina: An Approachable Part of the Brain, Revised Edition.* 2 edition. Cambridge, Mass: Belknap Press: An Imprint of Harvard University Press.
- Driehuis E, Kretschmar K, Clevers H. 2020. Establishment of patient-derived cancer organoids for drug-screening applications. *Nat Protoc.* 15(10):3380–3409. doi:10.1038/s41596-020-0379-4.
- Drost J, Clevers H. 2017. Translational applications of adult stem cell-derived organoids. *Development.* 144(6):968–975. doi:10.1242/dev.140566.
- Durens M, Nestor J, Williams M, Herold K, Niescier RF, Lunden JW, Phillips AW, Lin Y-C, Dykxhoorn DM, Nestor MW. 2020. High-throughput screening of human induced pluripotent stem cell-derived brain organoids. *J Neurosci Methods.* 335:108627. doi:10.1016/j.jneumeth.2020.108627.
- Fen W, Sicen W, Xilan G, Health Science Center, School of Pharmacy, Xi’an Jiaotong University, Xi’an 710061, China. 2021. A review for cell-based screening methods in drug discovery. *Biophys Rep.* 7(6):504–516. doi:10.52601/bpr.2021.210042.
- Ferrari S, Di Iorio E, Barbaro V, Ponzin D, Sorrentino FS, Parmeggiani F. 2011. Retinitis pigmentosa: genes and disease mechanisms. *Curr Genomics.* 12(4):238–249. doi:10.2174/138920211795860107.
- Fleckenstein M, Keenan TDL, Guymer RH, Chakravarthy U, Schmitz-Valckenberg S, Klaver CC, Wong WT, Chew EY. 2021. Age-related macular degeneration. *Nat Rev Dis Primer.* 7(1):31. doi:10.1038/s41572-021-00265-2.
- Fligor CM, Lavekar SS, Harkin J, Shields PK, VanderWall KB, Huang K-C, Gomes C, Meyer JS. 2021. Extension of retinofugal projections in an assembled model of human pluripotent stem cell-derived organoids. *Stem Cell Rep.* 16(9):2228–2241. doi:10.1016/j.stemcr.2021.05.009.
- Gupta N, Brown KE, Milam AH. 2003. Activated microglia in human retinitis pigmentosa, late-onset retinal degeneration, and age-related macular degeneration. *Exp Eye Res.* 76(4):463–471. doi:10.1016/S0014-4835(02)00332-9.
- Haber AL, Biton M, Rogel N, Herbst RH, Shekhar K, Smillie C, Burgin G, Delorey TM, Howitt MR, Katz Y, et al. 2017. A single-cell survey of the small intestinal epithelium. *Nature.* 551(7680):333–339. doi:10.1038/nature24489.
- Handelman IL, Robertson JE, Weleber RG, Meyer SM. 1983. Retinal Toxicity of Therapeutic Agents. *J Toxicol Cutan Ocul Toxicol.* 2(2–3):131–152. doi:10.3109/15569528309065310.

- Hindley CJ, Cordero-Espinoza L, Huch M. 2016. Organoids from adult liver and pancreas: Stem cell biology and biomedical utility. *Dev Biol.* 420(2):251–261. doi:10.1016/j.ydbio.2016.06.039.
- Houston JG, Banks MN. 2003. High-Throughput Screening for Lead Discovery. In: *Burger's Medicinal Chemistry and Drug Discovery*. 1st ed. Wiley. p. 37–69. [accessed 2023 Oct 30]. <https://onlinelibrary.wiley.com/doi/10.1002/0471266949.bmc020>.
- Hu Y, Sui X, Song F, Li Y, Li K, Chen Z, Yang F, Chen Xiuyuan, Zhang Y, Wang X, et al. 2021. Lung cancer organoids analyzed on microwell arrays predict drug responses of patients within a week. *Nat Commun.* 12(1):2581. doi:10.1038/s41467-021-22676-1.
- Humphries P, Kenna P, Farrar G. 1992. On the molecular genetics of retinitis pigmentosa. *Science.* 256(5058):804–808. doi:10.1126/science.1589761.
- Jin M-Z, Han R-R, Qiu G-Z, Ju X-C, Lou G, Jin W-L. 2018. Organoids: An intermediate modeling platform in precision oncology. *Cancer Lett.* 414:174–180. doi:10.1016/j.canlet.2017.11.021.
- Kawamura S, Tachibanaki S. 2008. Rod and cone photoreceptors: Molecular basis of the difference in their physiology. *Comp Biochem Physiol A Mol Integr Physiol.* 150(4):369–377. doi:10.1016/j.cbpa.2008.04.600.
- Kim Suran, Cho A, Min S, Kim Sooyeon, Cho S. 2019. Organoids for Advanced Therapeutics and Disease Models. *Adv Ther.* 2(1):1800087. doi:10.1002/adtp.201800087.
- Krenn V, Bosone C, Burkard TR, Spanier J, Kalinke U, Calistri A, Salata C, Rilo Christoff R, Pestana Garcez P, Mirazimi A, et al. 2021. Organoid modeling of Zika and herpes simplex virus 1 infections reveals virus-specific responses leading to microcephaly. *Cell Stem Cell.* 28(8):1362–1379.e7. doi:10.1016/j.stem.2021.03.004.
- Krol J, Roska B. 2015. Rods Feed Cones to Keep them Alive. *Cell.* 161(4):706–708. doi:10.1016/j.cell.2015.04.031.
- Kwiatkowska E, Stefańska K, Zieliński M, Sakowska J, Jankowiak M, Trzonkowski P, Marek-Trzonkowska N, Kwiatkowski S. 2020. Podocytes—The Most Vulnerable Renal Cells in Preeclampsia. *Int J Mol Sci.* 21(14):5051. doi:10.3390/ijms21145051.
- Lakkaraju A, Umopathy A, Tan LX, Daniele L, Philp NJ, Boesze-Battaglia K, Williams DS. 2020. The cell biology of the retinal pigment epithelium. *Prog Retin Eye Res.* 78:100846. doi:10.1016/j.preteyeres.2020.100846.
- Lancaster MA, Knoblich JA. 2014. Organogenesis in a dish: Modeling development and disease using organoid technologies. *Science.* 345(6194):1247125. doi:10.1126/science.1247125.
- Lane A, Jovanovic K, Shortall C, Ottaviani D, Panes AB, Schwarz N, Guarascio R, Hayes MJ, Palfi A, Chadderton N, et al. 2020. Modeling and Rescue of RP2 Retinitis Pigmentosa Using iPSC-Derived Retinal Organoids. *Stem Cell Rep.* 15(1):67–79. doi:10.1016/j.stemcr.2020.05.007.
- Leong YC, Di Foggia V, Pramod H, Bitner-Glindzicz M, Patel A, Sowden JC. 2022. Molecular pathology of Usher 1B patient-derived retinal organoids at single cell resolution. *Stem Cell Rep.* 17(11):2421–2437. doi:10.1016/j.stemcr.2022.09.006.
- Léveillard T, Mohand-Saïd S, Lorentz O, Hicks D, Fintz A-C, Clérin E, Simonutti M, Forster V, Cavusoglu N, Chalmel F, et al. 2004. Identification and characterization of rod-derived cone viability factor. *Nat Genet.* 36(7):755–759. doi:10.1038/ng1386.
- Linsenmeier RA, Padnick-Silver L. 2000. Metabolic dependence of photoreceptors on the choroid in the normal and detached retina. *Invest Ophthalmol Vis Sci.* 41(10):3117–3123.

- Lukonin I, Serra D, Challet Meylan L, Volkmann K, Baaten J, Zhao R, Meeusen S, Colman K, Maurer F, Stadler MB, et al. 2020. Phenotypic landscape of intestinal organoid regeneration. *Nature*. 586(7828):275–280. doi:10.1038/s41586-020-2776-9.
- Lutty GA, McLeod DS. 2018. Development of the hyaloid, choroidal and retinal vasculatures in the fetal human eye. *Prog Retin Eye Res*. 62:58–76. doi:10.1016/j.preteyeres.2017.10.001.
- Masland RH. 2012. The Neuronal Organization of the Retina. *Neuron*. 76(2):266–280. doi:10.1016/j.neuron.2012.10.002.
- Mayerl SJ, Bajgai S, Ludwig AL, Jager LD, Williams BN, Bacig C, Stoddard C, Sinha D, Philpot BD, Gamm DM. 2022. Human retinal organoids harboring IMPG2 mutations exhibit a photoreceptor outer segment phenotype that models advanced retinitis pigmentosa. *Stem Cell Rep*. 17(11):2409–2420. doi:10.1016/j.stemcr.2022.09.004.
- McColgan P, Tabrizi SJ. 2018. Huntington’s disease: a clinical review. *Eur J Neurol*. 25(1):24–34. doi:10.1111/ene.13413.
- McKinley KL, Castillo-Azofeifa D, Klein OD. 2020. Tools and Concepts for Interrogating and Defining Cellular Identity. *Cell Stem Cell*. 26(5):632–656. doi:10.1016/j.stem.2020.03.015.
- Mohand-Said S, Deudon-Combe A, Hicks D, Simonutti M, Forster V, Fintz AC, Léveillard T, Dreyfus H, Sahel JA. 1998. Normal retina releases a diffusible factor stimulating cone survival in the retinal degeneration mouse. *Proc Natl Acad Sci U S A*. 95(14):8357–8362. doi:10.1073/pnas.95.14.8357.
- Montagnani S, Rueger MA, Hosoda T, Nurzynska D. 2016. Adult Stem Cells in Tissue Maintenance and Regeneration. *Stem Cells Int*. 2016:1–2. doi:10.1155/2016/7362879.
- Morgan JE. 2012. Retina ganglion cell degeneration in glaucoma: an opportunity missed? A review: RGC degeneration. *Clin Experiment Ophthalmol*. 40(4):364–368. doi:10.1111/j.1442-9071.2012.02789.x.
- Morrison SJ, Uchida N, Weissman IL. 1995. The Biology of Hematopoietic Stem Cells. *Annu Rev Cell Dev Biol*. 11(1):35–71. doi:10.1146/annurev.cb.11.110195.000343.
- Muller A, Sullivan J, Schwarzer W, Wang M, Park-Windhol C, Klingler B, Matsell J, Hostettler S, Galliker P, Duman M, et al. 2023. High-efficiency base editing for Stargardt disease in mice, non-human primates, and human retina tissue. *Neuroscience*. [accessed 2023 Oct 31]. <http://biorxiv.org/lookup/doi/10.1101/2023.04.17.535579>.
- Narayan DS, Wood JPM, Chidlow G, Casson RJ. 2016. A review of the mechanisms of cone degeneration in retinitis pigmentosa. *Acta Ophthalmol (Copenh)*. 94(8):748–754. doi:10.1111/aos.13141.
- Newton F, Megaw R. 2020. Mechanisms of Photoreceptor Death in Retinitis Pigmentosa. *Genes*. 11(10):1120. doi:10.3390/genes11101120.
- Parmeggiani F. 2011. Clinics, epidemiology and genetics of retinitis pigmentosa. *Curr Genomics*. 12(4):236–237. doi:10.2174/138920211795860080.
- Paşca SP, Arlotta P, Bateup HS, Camp JG, Cappello S, Gage FH, Knoblich JA, Kriegstein AR, Lancaster MA, Ming G-L, et al. 2022. A nomenclature consensus for nervous system organoids and assembloids. *Nature*. 609(7929):907–910. doi:10.1038/s41586-022-05219-6.
- Patrício D, Santiago J, Mano JF, Fardilha M. 2023. Organoids of the male reproductive system: Challenges, opportunities, and their potential use in fertility research. *WIREs Mech Dis*. 15(2). doi:10.1002/wsbm.1590. [accessed 2023 Aug 17]. <https://onlinelibrary.wiley.com/doi/10.1002/wsbm.1590>.

- Pleguezuelos-Manzano C, Puschhof J, den Brink S, Geurts V, Beumer J, Clevers H. 2020. Establishment and Culture of Human Intestinal Organoids Derived from Adult Stem Cells. *Curr Protoc Immunol.* 130(1). doi:10.1002/cpim.106. [accessed 2022 May 14]. <https://onlinelibrary.wiley.com/doi/10.1002/cpim.106>.
- Punzo C, Kornacker K, Cepko CL. 2009. Stimulation of the insulin/mTOR pathway delays cone death in a mouse model of retinitis pigmentosa. *Nat Neurosci.* 12(1):44–52. doi:10.1038/nn.2234.
- Raza C, Anjum R, Shakeel NUA. 2019. Parkinson’s disease: Mechanisms, translational models and management strategies. *Life Sci.* 226:77–90. doi:10.1016/j.lfs.2019.03.057.
- Romito A, Cobellis G. 2016. Pluripotent Stem Cells: Current Understanding and Future Directions. *Stem Cells Int.* 2016:1–20. doi:10.1155/2016/9451492.
- Rossi G, Manfrin A, Lutolf MP. 2018. Progress and potential in organoid research. *Nat Rev Genet.* 19(11):671–687. doi:10.1038/s41576-018-0051-9.
- Sagar, Herman JS, Pospisilik JA, Grün D. 2018. High-Throughput Single-Cell RNA Sequencing and Data Analysis. In: Vavouri T, Peinado MA, editors. *CpG Islands.* Vol. 1766. New York, NY: Springer New York. (Methods in Molecular Biology). p. 257–283. [accessed 2023 Oct 30]. [http://link.springer.com/10.1007/978-1-4939-7768-0\\_15](http://link.springer.com/10.1007/978-1-4939-7768-0_15).
- Sağraç D, Şişli HB, Şenkal S, Hayal TB, Şahin F, Doğan A. 2021. Organoids in Tissue Transplantation. In: Turksen K, editor. *Cell Biology and Translational Medicine, Volume 14.* Vol. 1347. Cham: Springer International Publishing. (Advances in Experimental Medicine and Biology). p. 45–64. [accessed 2023 Oct 26]. [https://link.springer.com/10.1007/5584\\_2021\\_647](https://link.springer.com/10.1007/5584_2021_647).
- Saha A, Capowski E, Fernandez Zepeda MA, Nelson EC, Gamm DM, Sinha R. 2022. Cone photoreceptors in human stem cell-derived retinal organoids demonstrate intrinsic light responses that mimic those of primate fovea. *Cell Stem Cell.* 29(3):460-471.e3. doi:10.1016/j.stem.2022.01.002.
- Sharma K, Krohne TU, Busskamp V. 2020. The Rise of Retinal Organoids for Vision Research. *Int J Mol Sci.* 21(22):8484. doi:10.3390/ijms21228484.
- Shen J, Yang X, Dong A, Petters RM, Peng Y-W, Wong F, Campochiaro PA. 2005. Oxidative damage is a potential cause of cone cell death in retinitis pigmentosa. *J Cell Physiol.* 203(3):457–464. doi:10.1002/jcp.20346.
- Slijkerman RWN, Song F, Astuti GDN, Huynen MA, Van Wijk E, Stieger K, Collin RWJ. 2015. The pros and cons of vertebrate animal models for functional and therapeutic research on inherited retinal dystrophies. *Prog Retin Eye Res.* 48:137–159. doi:10.1016/j.preteyeres.2015.04.004.
- Spirig SE, Renner M. 2023 May 22. Toward Retinal Organoids in High-Throughput. *Cold Spring Harb Perspect Med.*:a041275. doi:10.1101/cshperspect.a041275.
- Sridhar A, Hoshino A, Finkbeiner CR, Chitsazan A, Dai L, Haugan AK, Eschenbacher KM, Jackson DL, Trapnell C, Bermingham-McDonogh O, et al. 2020. Single-Cell Transcriptomic Comparison of Human Fetal Retina, hPSC-Derived Retinal Organoids, and Long-Term Retinal Cultures. *Cell Rep.* 30(5):1644-1659.e4. doi:10.1016/j.celrep.2020.01.007.
- Strauss O. 2005. The Retinal Pigment Epithelium in Visual Function. *Physiol Rev.* 85(3):845–881. doi:10.1152/physrev.00021.2004.
- Sun X-Y, Ju X-C, Li Y, Zeng P-M, Wu J, Zhou Y-Y, Shen L-B, Dong J, Chen Y-J, Luo Z-G. 2022. Generation of vascularized brain organoids to study neurovascular interactions. *eLife.* 11:e76707. doi:10.7554/eLife.76707.



- Takahashi K, Tanabe K, Ohnuki M, Narita M, Ichisaka T, Tomoda K, Yamanaka S. 2007. Induction of Pluripotent Stem Cells from Adult Human Fibroblasts by Defined Factors. *Cell*. 131(5):861–872. doi:10.1016/j.cell.2007.11.019.
- Takahashi K, Yamanaka S. 2006. Induction of Pluripotent Stem Cells from Mouse Embryonic and Adult Fibroblast Cultures by Defined Factors. *Cell*. 126(4):663–676. doi:10.1016/j.cell.2006.07.024.
- Tang X-Y, Wu S, Wang D, Chu C, Hong Y, Tao M, Hu H, Xu M, Guo X, Liu Y. 2022. Human organoids in basic research and clinical applications. *Signal Transduct Target Ther*. 7(1):168. doi:10.1038/s41392-022-01024-9.
- Toshimitsu K, Takano A, Fujii M, Togasaki K, Matano M, Takahashi S, Kanai T, Sato T. 2022. Organoid screening reveals epigenetic vulnerabilities in human colorectal cancer. *Nat Chem Biol*. 18(6):605–614. doi:10.1038/s41589-022-00984-x.
- Tremblay M-È. 2020. A Diversity of Cell Types, Subtypes and Phenotypes in the Central Nervous System: The Importance of Studying Their Complex Relationships. *Front Cell Neurosci*. 14:628347. doi:10.3389/fncel.2020.628347.
- Velasco S, Kedaigle AJ, Simmons SK, Nash A, Rocha M, Quadrato G, Paulsen B, Nguyen L, Adiconis X, Regev A, et al. 2019. Individual brain organoids reproducibly form cell diversity of the human cerebral cortex. *Nature*. 570(7762):523. doi:10.1038/s41586-019-1289-x.
- Weaver WM, Tseng P, Kunze A, Masaeli M, Chung AJ, Dudani JS, Kittur H, Kulkarni RP, Di Carlo D. 2014. Advances in high-throughput single-cell microtechnologies. *Curr Opin Biotechnol*. 25:114–123. doi:10.1016/j.copbio.2013.09.005.
- de Witte CJ, Espejo Valle-Inclan J, Hami N, Löhmußaar K, Kopper O, Vreuls CPH, Jonges GN, van Diest P, Nguyen L, Clevers H, et al. 2020. Patient-Derived Ovarian Cancer Organoids Mimic Clinical Response and Exhibit Heterogeneous Inter- and Inpatient Drug Responses. *Cell Rep*. 31(11):107762. doi:10.1016/j.celrep.2020.107762.
- Yao Y, Xu X, Yang L, Zhu J, Wan J, Shen L, Xia F, Fu G, Deng Y, Pan M, et al. 2020. Patient-Derived Organoids Predict Chemoradiation Responses of Locally Advanced Rectal Cancer. *Cell Stem Cell*. 26(1):17-26.e6. doi:10.1016/j.stem.2019.10.010.
- Yarfitz S, Hurley JB. 1994. Transduction mechanisms of vertebrate and invertebrate photoreceptors. *J Biol Chem*. 269(20):14329–14332.
- Zeit C, Robson AG, Audo I. 2015. Congenital stationary night blindness: An analysis and update of genotype–phenotype correlations and pathogenic mechanisms. *Prog Retin Eye Res*. 45:58–110. doi:10.1016/j.preteyeres.2014.09.001.
- Zhong X, Gutierrez C, Xue T, Hampton C, Vergara MN, Cao L-H, Peters A, Park TS, Zambidis ET, Meyer JS, et al. 2014. Generation of three-dimensional retinal tissue with functional photoreceptors from human iPSCs. *Nat Commun*. 5(1):4047. doi:10.1038/ncomms5047.

## **9 Appendix: manuscript supplementary tables**

**Table S1**

Inchi-key	SMILES	MOA	GeneIDs	Median adj. cone survival (%)
BWDQBBCUWLSASG-MDZDMLPSA-N	<chem>OCCN(CCC1=CNc2ccccc12)Cc3ccc/C=C/C(=O)NO)cc3</chem>	HDAC 1/2/3/6/8/10/11;Antimitotic Drugs;Apoptosis Inducers;Histone Deacetylase (HDAC) Inhibitors	HDAC9,HDAC6,HDAC5,HDAC7,HDAC8,HDAC11,HDAC10	0
ATSUJKLLCSXMLV-BUHFOSPRSA-N	<chem>ONC(=O)/C=C/c4ccc(CNCCN3c1cccc1c2ccccc23)cc4</chem>	Histone Deacetylase (HDAC) Inhibitors	HDAC9,HDAC5,HDAC7,HDAC8,HDAC11,HDAC10	5
NLKQTNNGJKCBXMU-MDZDMLPSA-N	<chem>ONC(=O)/C=C/c3ccc(CNCCc2cnc1ccc1c2)cc3</chem>	Histone Deacetylase (HDAC) Inhibitors	HDAC9,HDAC5,HDAC7,HDAC8,HDAC11,HDAC10	4
HPTMTYKYKUKYCQ-UHFFFAOYSA-N	<chem>Cc1ccc(cc1NS(C)(=O)=O)Nc2cc(ncn2)c3ccccc3O</chem>	CDK1/2 inhibitor	CCNA1	7
PIROHBFQHMKAPE-UHFFFAOYSA-N	<chem>CNc4nc1cccc1c(NCc2ccc(cc2)NC(=O)c3ccc(Cl)nc3)n4</chem>	beta-Catenin Inhibitors	CTNNB1,TCF4	9
QPKKAIMODKGHRH-UHFFFAOYSA-N	<chem>CCN(Cc1cccc(c1)c3ccnc(Nc2cccc(c2)[N+]([O-])=O)n3)C(C)C</chem>	Antimitotic Drugs;Inhibitors of Signal Transduction Pathways;Aurora-A (ARK1) Kinase Inhibitors;Glycogen Synthase Kinase 3 beta (GSK-3beta) tau Protein Kinase I) Inhibitors;Cyclin-Dependent Kinase Inhibitors	GSK3B,AURKA,CDKL5	10
MUAICZWSFWUFNA-INIZCTEOSA-N	<chem>C[C@H](NCc1ccc4c(c1)N=C(NC(=O)C2=CC=C(S2)C3C=NNC=3)N4CC(C)(C)O)C(C)C</chem>	ITK (EMT) Kinase Inhibitors;IL-4 Production Inhibitors;IL-2 Production Inhibitors	IL2,IL4,ITK	4
RLFKILXOLJVUNF-UHFFFAOYSA-N	<chem>COCc2c(ncc3Nc1ccc(cc1c23)OCc4ccc4)C(=O)OC(C)C</chem>	GABA(A) BZ Site Receptor Partial Agonists	GABRA1,GABRA2,GABRA3,GABRA5,GABRB3,GABRG2	14
PRDFBSVERLRMY-UHFFFAOYSA-N	<chem>CCOc1ccc(cc1)C3Nc2ccc(cc2N=3)C5Nc4ccc(cc4N=5)N6CCN(C)CC6</chem>	BCL2L1 gene inhibitor	BCL2L1	10
JWOGUUIOCYMBPV-GMFLJSBRSAN	<chem>CCC(=O)CCCC[C@H]4NC(=O)[C@H]1CCCCN1C(=O)[C@@H](NC(=O)[C@H](CC2=CN(OC)c3ccccc23)NC4=O)[C@@H](C)CC</chem>	HDAC inhibitor	HDAC3,HDAC4	13
SMYUEWYXIKCMEA-UHFFFAOYSA-N	<chem>Cc1ccc(cc1)OC2CCN(CC2)c4ncnc3ccc(F)cc34</chem>	Positive allosteric modulators (PAMs) of the muscarinic acetylcholine	CHRM4	12
VTGBZWHPJFMTKS-UHFFFAOYSA-N	<chem>CCc1ccc(cc1)OCc2ccccc2C(=O)Nc4cc3nc(C)cc(N)c3c4</chem>	OPRL1 gene inhibitor;OPRM1 gene inhibitor	OPRL1,OPRM1	11
SETVRSKZJJWOPA-FLDGXQSCSA-N	<chem>C/C(/C=C/[C@@]1(C)[C@H](C)CCC(=O)[C@@H]1C)=C\Cc2c(O)c(Cl)c(C)c(C=O)c2O</chem>	"AP-1 Inhibitors;Electron Transport Chain Inhibitors";AP-1 Inhibitors;Electron Transport Chain Inhibitors	JUN,UQCRC1	11
RBTBFTRPCNLSDE-UHFFFAOYSA-N	<chem>CN(C)c3ccc2N=C1C=CC(C=C1Sc2c3)=N+](C)C</chem>	Nitric Oxide Production Inhibitors;Tau Aggregation Inhibitors	MAPT	13
JUVIOZPCNVVQFO-HBGVWJBISAN	<chem>COc5cc4OC[C@H]3Oc1c(ccc2O[C@H](Cc12)C(C)=C)C(=O)[C@H]3c4cc5OC</chem>	Electron transport chain inhibitor;Apoptosis Inducers;NADH-Ubiquinone Oxidoreductase (Complex I) Inhibitors;Non-Steroidal Antiinflammatory Drugs;Electron Transport Chain Inhibitors;"Electron transport chain inhibitor;Apoptosis Inducers;NADH-Ubiquinone Oxidoreductase (Complex I) Inhibitors;Non-Steroidal Antiinflammatory Drugs;Electron Transport Chain Inhibitors"	NDUFS1,NOX4,NOX5	19
ZLUZDKXBTNQWOL-MDZDMLPSA-N	<chem>ONC(=O)/C=C/c3ccc(CNCCC1=CNc2ccccc12)cc3</chem>	HDAC inhibitor	HDAC9,HDAC6,HDAC5,HDAC7,HDAC8,HDAC11,HDAC10	13
ILAZEUGGANOTAY-VAWYXSNFSA-N	<chem>CC(C)N(CCC1=CNc2ccccc12)Cc3ccc(/C=C/C(=O)NO)cc3</chem>	Histone Deacetylase (HDAC) Inhibitors	HDAC9,HDAC5,HDAC7,HDAC8,HDAC11,HDAC10	15
OTSOOHRUMBRSHZ-UHFFFAOYSA-N	<chem>COCC[N+](C)(C)N(Cc1cncn1)C3C(=O)c2ccccc2C(=O)C=34</chem>	BIRC5 gene inhibitor	BIRC5	14

Inchi-key	SMILES	MOA	GeneIDs	Median adj. cone survival (%)
XQYZDYMELSDRZ-UHFFFAOYSA-N	<chem>COc3ccc(Cc1nccc2cc(OC)c(cc12)OC)cc3OC</chem>	Phosphodiesterase PDE10A Inhibitors	PDE4C,PDE10A,ENPP6	11
ALBKMJDFBZVHAK-UHFFFAOYSA-N	<chem>CCOC(=O)c3ncc2Nc1ccc(cc1c2c3CO)OCc4cccc4</chem>	Anxiolytics	GABRA1,GABRA2,GABRA3,GABRB3,GABRG2	10
NUUSUAWULNXMGF-UHFFFAOYSA-N	<chem>O=C(Nc1ccc(Cl)c(Cl)c1)Nc3ccc2N=NSc2c3</chem>	Eukaryotic Translation Initiation Factor 2-alpha Kinase 1 (HRI) Activators	EIF2AK1	12
FUGQNAUKABUDQI-UHFFFAOYSA-N	<chem>CC(C)C2=Cc1c(ncnc1S2)N3CCN(CC3)C4=NCC(C)(C)S4</chem>	Inhibitor of MEN1 (Menin);MEN1 inhibitor	MEN1	18
SCJXQZZYGYLKJG-CQSZACIVSA-N	<chem>CC[C@@H](N)CNc1ccnc(n1)c2cc(ccc2O)C3C=NN(C)C=3</chem>	protein kinase d inhibitor	PKD1	18
RDALZZCKQLGJP-UHFFFAOYSA-N	<chem>CC2=Cc1c(cccc1N2c5nc3CCOCc3c(NCc4cccc4)n5)C(N)=O</chem>	p97 AAA ATPase inhibitor	VCP	16
IYVIAGDMQOYYQC-OUKQBFOZSA-N	<chem>ONC(=O)/C=C/c2ccc(CNCCCc1ccccc1)cc2</chem>	Histone Deacetylase (HDAC) Inhibitors	HDAC9,HDAC5,HDAC7,HDAC8,HDAC11,HDAC10	19
VQQRBBFRJRBWPF-UHFFFAOYSA-N	<chem>CCN4CCN(Cc1ccc(cc1C(F)(F)F)NC(=O)Nc2ccc(cc2)Oc3ccnc(N)n3)CC4</chem>	Flt3 (FLK2/STK1) Inhibitors	FLT3	13
SKBXAZQJXDJNFI-RMKNXTFCSA-N	<chem>COc3ccc2NC=C(CCNc1ccc(/C=C/C(=O)NO)cc1)c2c3</chem>	Histone Deacetylase (HDAC) Inhibitors	HDAC9,HDAC5,HDAC7,HDAC8,HDAC11,HDAC10	12
XQYASZNUFDVMFH-CQSZACIVSA-N	<chem>C[C@@H]2CN(Cc1ccc(F)cc1)CCN2C(=O)COc3ccc(Cl)cc3NC(N)=O</chem>	Chemokine CCR1 Antagonists	CCR1	15
YJGVMLPVUAXIQN-XVVDYKMHSA-N	<chem>COc1cc(cc(OC)c1OC)[C@@H]4c3cc2OCOc2cc3[C@H](O)[C@H]5COC(=O)[C@H]45</chem>		TUBA4A,TUBB2A,TUBA1A,TUBA1B,TUBB3,TUBB4A,TUBB4B,TUBB1,TUBB6,TUBA1C,TUBA3E,TUBA3D,TUBB,TUBB8,TUBB2B,TUBA3C,TUBG1,TUBG2,TUBD1,TUBA8	17
OKJDLRMQHZRYOZ-UHFFFAOYSA-N	<chem>NCCCN4C(=O)c1cc(ccc1C3C(=O)c2cc(O)cc2C=34)[N+]([O-])=O</chem>	Dual Top1, TDP1 inhibitors	TOP1,TDP1	16
BPRNMVDTWIHULJ-AWEZNOQLSA-N	<chem>C[C@@H](CN1CCN(CC1)S(=O)(=O)c2ccc(Cl)c(Cl)c2)Nc3ncnc4C(C)=CS34</chem>	Lysophosphatidate-2 receptor antagonist	LPAR2	22
BPNUXQPIQBZCMR-IBGZPJMESA-N	<chem>CC1=NNc2ccc(cc12)c3nccc(c3)OC[C@@H](N)C4CCCC4</chem>	cAMP-Dependent Protein Kinase (PKA) Inhibitors;Inhibitors of Signal Transduction Pathways;PKB alpha/Akt1 Inhibitors	PRKACA,PRKACB,PRKACG	22
XVOOCQSWCCRVDY-UHFFFAOYSA-N	<chem>COc4cc(Br)c(NC1=NC(=CS1)C2=C(C)N=C3N=CC=CN23)c(Br)c4</chem>	Polycomb Complex Protein BMI-1 Inhibitors	BMI1	16
AWIVHRPYFSSVOG-UHFFFAOYSA-N	<chem>Fc3ccc(CNc1ncnc2ccc(F)cc12)cc3</chem>	Autophagy Agonist;Phosphodiesterase V (PDE5A) Inhibitors	PDE5A	15
WOFGKQKJKFJLB-UHFFFAOYSA-N	<chem>COCCc1cc(ccn1)C2=CNc3cc(ccc23)C(=O)c4ccc(Cl)c(c4)S(N)(=O)=O</chem>	MMP-13 (Collagenase 3) Inhibitors;MMP-2 (Gelatinase A) Inhibitors	MMP2,MMP13	22
SXHHURZUIGDYAR-QGZVFWFLSA-N	<chem>C[C@@H]1CCCN1c3cc(cc(Nc2cc(C#N)ccn2)n3)C4(C#N)CCN(C)CC4</chem>	MAP3K12 (DLK) Inhibitors	MAP3K12	12
SGYJGGKDBGXCNZDIDWYTNSA-N	<chem>CC4(C)NC(=O)[C@H](CCCCC(=O)C1CO1)NC(=O)[C@H]2CCCN2C(=O)[C@H](Cc3cccc3)NC4=O</chem>	Reported to be a general HDAC inhibitor	HDAC1,HDAC2,HDAC3,HDAC4,HDAC6,HDAC5	19
GAKKPKBEHVILH-UHFFFAOYSA-N	<chem>CNC1=NC(C)=C(S1)c4ccnc(Nc2ccc(c2)N3CCNCCC3)n4</chem>	CDK Inhibitor;Pan Kinase Inhibitor	CDK2,CCNE2	20
CHILCFMQWMQVAL-UHFFFAOYSA-N	<chem>Oc1ccc(Cl)cc1C(=O)Nc2cc(cc(c2)C(F)(F)F)C(F)(F)F</chem>	IKK-2 (IKK-beta) Inhibitors;NF-kappaB (NFKB) Activation Inhibitors	IKKB	14
KPBNHDGDUADAGP-VAWYXSNFSA-N	<chem>O=C(/C=C/c1cccnc1)NCCCC2CCN(CC2)C(=O)c3cccc3</chem>	Angiogenesis Inhibitors;Apoptosis Inducers;Nicotinamide Phosphoribosyltransferase (NMPRTase) Inhibitors	NAMPT	23

Inchi-key	SMILES	MOA	GeneIDs	Median adj. cone survival (%)
VJXBYUITQBTTQM-DSRNDQRRSA-N	<chem>CC[C@H](C)[C@H]2NC(=O)[C@H]1C SSSCC=C[C@H](CC(=O)N[C@H](CC SC)C(=O)N1)OC(=O)C[C@H]2O</chem>	HDAC inhibitor (no hydroxamic acid)	HDAC1,HDAC2,HDAC3, HDAC6,HDAC8	15
IYNDTACKOAXKBJ-UHFFFAOYSA-N	<chem>OCCCNc1cc(ccn1)c3ccnc(Nc2cccc(Cl)c2)n3</chem>	Protein Kinase C (PKC) Inhibitors;CDK1 Inhibitors;CDK2 Inhibitors	CDK1,CDK2	15
IEENMDADGAZPAM-UHFFFAOYSA-N	<chem>CCC(C)C6C(=O)N1NCCCC1C(=O)N2 NCCCC2C(=O)N(C)C(Cc3ccccc3)C(=O)N4CCCC4C(=O)NC(Cc5ccccc5)C(=O)N6O</chem>	Vasopressin (AVP) V1a Antagonists;Vasopressin (AVP) V2 Antagonists	AVPR1A,AVPR2	13
VFBGXTUGODTSPK-BAQGIRSFSA-N	<chem>O=C3Nc2ccc1N=CSc1c2/C3=C/C4=CNC=N4</chem>	PKR Inhibitor	EIF2AK2	18
HCAQGGQIHFVVIX-LYXAAFRTSA-N	<chem>C/C(=N)NC(N)=N/c1ccc(cc1)NC(=O)Nc2ccc(cc2)/C(/C)=N/NC(N)=N</chem>	Ribonuclease P Inhibitors;Checkpoint Kinase 2 (Chk2) Inhibitors	CHEK2	20
BFXLAXBXCXOWNH-UHFFFAOYSA-N	<chem>[O-][N+](=O)c1cc(ccc1Cl)S(=O)(=O)Nc2c cc(Cl)cc2C(=O)Nc3ccc(Cl)cc3</chem>	Phosphopantetheine Adenylyltransferase (PPAT) Inhibitors	COASY	24
BBLGCDSLCDDALX-LKGBESRRSA-N	<chem>C/C=C(\C)/[C@H](O)[C@H](C)/C=C(\C)/C=C/C/C(/C)=C/Cc1nc(OC)c(OC)c(O)c1C</chem>	NADH oxidase inhibitors;Electron transport chain inhibitor	NDUFAB1,NDUFS1,NDUFV1	19
FUSNMLFNXJSCDI-UHFFFAOYSA-N	<chem>Cc1cccc(c1)N(C)C(=S)Oc3ccc2ccccc2c3</chem>	Fungal Squalene Monooxygenase Inhibitors	SQLE	24
OWBFCJROIKNMGD-BQYQJAHWSA-N	<chem>COc2cc(OC)c(/C=C/S(=O)(=O)Cc1ccc(OC)c(c1)NCC(O)=O)c(c2)OC</chem>	Antagonist of Raf-Ras interaction	BRAF,RAF1,ZHX2	24
HRNLUBSXIHFDPH-UHFFFAOYSA-N	<chem>Nc1cccc1NC(=O)c4ccc(CNc2nccc(n2)c3cccn3)cc4</chem>	HDAC1/2;Apoptosis Inducers;Histone Deacetylase 1 (HDAC1) Inhibitors	HDAC1,HDAC2,HDAC3	21
WQAVPPWWLLVGFK-VTNASVEKSA-N	<chem>COc4ccc(C[C@H](NC(=O)[C@H](C)N C(=O)CN1CCOCC1)C(=O)N[C@@H](Cc2ccccc2)C(=O)[C@@]3(C)CO3)cc4</chem>	Immunoproteasome Inhibitors	PSMB8	18
DNODJHQYSZVNMH-UHFFFAOYSA-N	<chem>Nc2ccc(O)c3C(=O)N(C1CCC(=O)NC1=O)C(=O)c23</chem>	CRBN neomorph;E3 ligase inhibitor	CRBN	22
IAKHMKGGTNLKSZ-INIZCTEOSA-N	<chem>COc3cc2CC[C@H](NC(C)=O)C1=CC(=O)C(=CC=C1c2c(OC)c3OC)OC</chem>	Tubulin Polymerase Inhibitors	TUBA4A,TUBB2A,TUBA1A,TUBA1B,TUBB3,TUBB4A,TUBB4B,TUBB1,TUBB6,TUBA1C,TUBA3E,TUBA3D,TUBB,TUBB8,TUBB2B,TUBA3C,TUBG1,TUBG2,TUBD1,TUBA8	13
WQBLEMAGSGUUGW-UHFFFAOYSA-N	<chem>Nc1cc(ccn1)c3ccnc(Nc2cccc(Cl)c2)n3</chem>	CDK1 Inhibitors	CDK1	24
YJGVMLPVUAXIQNHAEOHBJNSA-N	<chem>COc1cc(cc(OC)c1OC)[C@@H]4c3cc2OCOc2cc3[C@H](O)[C@H]5COC(=O)[C@@H]45</chem>	CASP3 activator;apoptosis inhibitor;IGF1R inhibitor;IGF-1R Inhibitors;Caspase 3 Activators;Apoptosis Inducers	CASP3,IGF1R	17
ZCURBFFRNVPIASCYBMUJFWSA-N	<chem>CCCCC(=O)N3C[C@@H](CC)c2c1cccc1c(O)cc23</chem>	covalent inhibitor of ALDH1A1	ALDH1A1	22
GVIFMXAPEOVXKOUHFFFAOYSA-N	<chem>COc5cc(CN4N=C(CCN1CCN(CC1)c2cccc(Cl)c2C)c3cc(OC)c(cc34)OC)ccc5OC</chem>	Calmodulin Antagonists	CALM1	21
LUTPUCJIKBULCQUHFFFAOYSA-N	<chem>CC2CCc1cc(F)ccc1N2C(=O)COc4ccc c3cnccc34</chem>	Bile Acid Responsive TGR5 Receptors (GPBAR1, AXOR 109, GPCR19) Agonists	GPBAR1	17
QLJDJSOFNVSHNGVMPITWQZSA-N	<chem>ONC(=O)/C=C/c3ccc(CNCCC1=CNc2ccc(F)cc12)cc3</chem>	Histone Deacetylase (HDAC) Inhibitors	HDAC9,HDAC5,HDAC7, HDAC8,HDAC11,HDAC10	19

Inchi-key	SMILES	MOA	GeneIDs	Median adj. cone survival (%)
UIFFUZRFRDZJC-SBOETFBSA-N	<chem>CCCCC[C@H]2C(=O)O[C@H](C)[C@H](NC(=O)c1cccc(NC=O)c1O)C(=O)O[C@@H](C)[C@H]2OC(=O)CC(C)C</chem>	Electron transport chain inhibitor;Cytochrome c reductase;Electron Transport Chain Inhibitors	UQCRC1	30
SDABUVHLPSIZEG-NBMRYCAZSA-N	<chem>CN4C(=O)[C@@]35C[C@](C)(C#N)[C@H](c2ccc1OCOc1c2)N3C(=O)[C@]4(C)SS5</chem>	induces concomitant H3K9me3 downregulation	SUV39H1	31
XWQVQSXLXAXOPJ-NJDAHKKSA-N	<chem>COC[C@H](C)N[C@@H]1CC[C@H](CC1)Nc2cc(c(Cl)cn2)c4cccc(NCC3(C#N)CCOCC3)n4</chem>	CDK9/Cyclin T1 Inhibitors	CCNT1,CDK9	28
JGDCRWYOMWSTFC-AZGSIFHYSA-N	<chem>C[C@]12CC[C@H](O)C[C@H]1CC[C@@H]3[C@@H]2[C@H](O)C(=O)[C@]4(C)[C@H](CC[C@]34O)C5C=CC(=O)OC=5</chem>	Arenobufagin, SMUT	PSMB1,PSMB2,PSMB5,ATP1B4	23
QSYLKMKIVWJAAK-UHFFFAOYSA-N	<chem>Cc5cc(Nc1ccc(cc1)NC(=O)c2ccc(cc2)Nc4ccnc3ccccc34)nc(N)n5</chem>	DNA Methyltransferase I Inhibitors	DNMT1	23
OHAXNCGNVGGWSO-UHFFFAOYSA-N	<chem>Oc2cc1cccc1cc2C(=O)Nc3ccc(Cl)cc3</chem>	Cyclic AMP Response Element-Binding Protein (CREB) Inhibitors	CREB1	28
DYLJVOXRWLXDIG-UHFFFAOYSA-N	<chem>COc1cccc(OC)c1C2=CC(=NN2c3ccnc4cc(Cl)ccc34)C(=O)NC6(C(O)=O)C5C7CC(C5)CC6C7</chem>	Carboxypeptidase A Inhibitors;Neurotensin NTS1 (NT1) Receptor Antagonists	NTSR1	29
XUSKJHCMMWAAHV-SANMLTNEA-N	<chem>CC[C@@]1(O)C(=O)OCc2c1cc3n(Cc4c(c5cc(O)ccc5nc43)[Sij](C)(C)(C)(C)C)c2=O</chem>	DNA-Intercalating Drugs;DNA Topoisomerase I Inhibitors	TOP1	25
ZGLXUQQMLLIKAN-SVIJTADQSA-N	<chem>COc1cc(cc(OC)c1OC)[C@@H]4c3cc2OCOc2cc3C[C@H]5COC(=O)[C@H]45</chem>	Cyclooxygenase-2 Inhibitors;Non-Steroidal Antiinflammatory Drugs;Angiogenesis Inhibitors	CASP3,PTGS2	34
ULXXDDBFHOBEHA-CWDCEQMOSA-N	<chem>CN(C)C/C=C/C(=O)Nc3cc2c(Nc1ccc(F)c(Cl)c1)ncnc2cc3O[C@H]4CCOC4</chem>	Irreversible EGFR (HER1;erbB1) Inhibitors;HER2 (erbB2) Inhibitors;Inhibitors of Signal Transduction Pathways	EGFR,ERBB2,ERBB4	23
KQNZDYITLMIZCT-KQPMLPITSA-N	<chem>C[C@H]2CCC/C=C/[C@@H]1C[C@H](O)C[C@H]1[C@H](O)/C=C/C(=O)O2</chem>	Apoptosis Inducers;Caspase 3 Activators;Autophagy inducer;"Apoptosis Inducers;Caspase 3 Activators;Autophagy inducer"	ARF1,GBF1,CYTH2,ARFGFE2,ARFGFE1,CYTH1	28
CDOVNWVANFFLJ-UHFFFAOYSA-N	<chem>C1CN(CCN1)c2ccc(cc2)C4C=NC3=C(C=NN3C=4)c6ccnc5ccccc56</chem>	Activin Receptor Like Kinase 3 (ALK3 BMPR-IA) Inhibitors;Activin Receptor Like Kinase 2 (ALK2 ActR-IA) Inhibitors	ACVR1,BMPR1A,BMPR1B	49
KAKPGJJRYRSTP-UHFFFAOYSA-N	<chem>COc1cc(cc(c1)N2CCN(CC2)C(=O)Nc4nc3cc(F)ccc3nc4OC)OC</chem>	phosphorylated-p68 RNA helicase inhibitor	DDX5	24
GUGBOAVFOFNJFG-VAWYXSNFSA-N	<chem>ONC(=O)/C=C/c3ccc(CNCCC1=CNc2ccccc12)cc3</chem>	Histone Deacetylase (HDAC) Inhibitors	HDAC9,HDAC5,HDAC7,HDAC8,HDAC11,HDAC10	30
UTOXGQNLFXWCMS-QGZVFWFLSA-N	<chem>CS(=O)(=O)N1CCCC(C1)C2=NOC(=N2)[C@H](CCCC3CCCC3)CC(=O)NO</chem>	Procollagen C-Proteinase Inhibitors	BMP1	28
INVTYAOGFAGBOE-UHFFFAOYSA-N	<chem>Nc1cccc1NC(=O)c3ccc(CNC(=O)OCc2ccnc2)cc3</chem>	HDAC1/3;Wnt pathway agonist;Histone deacetylase-1 inhibitor;Histone deacetylase-2 inhibitor	HDAC1,HDAC2,HDAC3	35
QQQFNQWZHSZIC-UHFFFAOYSA-N	<chem>CC1NC(CO)=C(C(=O)C=1Cl)c2ccc(cc2)Oc3ccc(cc3)OC(F)F</chem>	"P. falciparum Cytochrome b-c1 Complex (Complex III subunit 3) Inhibitors;Electron Transport Chain Inhibitors";"P. falciparum Cytochrome b-c1 Complex (Complex III subunit 3) Inhibitors;Electron Transport Chain Inhibitors	UQCRC1	35
ODPGGGTTSYGTGO-UHFFFAOYSA-N	<chem>CCN4CCN(Cc1ccc(cc1C(F)F)NC(=O)Nc2ccc(cc2)Oc3cc(NC)ncn3)CC4</chem>	Flt3 (FLK2/STK1) Inhibitors;Inhibitors of Signal Transduction Pathways	MAPK14,FLT3,KIT,PDGFRB,MAPK8,MAPK10	22
QJZRFPJCVMNVAV-HHHXNRCGSA-N	<chem>CC(C)[C@H](C2=Nc1cc(Cl)ccc1C(=O)N2Cc3ccccc3)N(CCN)C(=O)c4ccc(C)cc4</chem>	Antimitotic Drugs;Kinesin-Like Spindle Protein KIF11 (KSP, Eg5) Inhibitors	KIF11	25
ITFBYYCNVFPKD-FMIDTUQUSA-N	<chem>CC5(C)CC[C@@]4(CC[C@]3(C)[C@H](C(=O)C=C2[C@@]1(C)C=C(C#N)</chem>	Apoptosis Inducers;Nitric Oxide Production Inhibitors;Nuclear Factor, Erythroid Derived 2, Like 2 (Nrf2) Activators;Antiinflammatory Drugs;PPARgamma	NFE2L2,PPARG,KEAP1	37

Inchi-key	SMILES	MOA	GeneIDs	Median adj. cone survival (%)
	<chem>C(=O)C(C)(C)[C@@H]1CC[C@]23C)[C@@H]4C5)C(=O)N6C=CN=C6</chem>	Agonists;"Apoptosis Inducers;Nitric Oxide Production Inhibitors;Nuclear Factor, Erythroid Derived 2, Like 2 (Nrf2) Activators;Antiinflammatory Drugs;PPARgamma Agonists"		
XFMZYCHKCPPZQW-HXUWFJFHSA-N	<chem>CN(C)C[C@@H](OC(=O)N3CC2=C(NC(=O)c1ccc(F)cc1)NN=C2C3(C)C)c4cccc4</chem>	PAK4 gene inhibitor	PAK4	27
MRAMUVZVDBOPEH-JOCHJYFZSA-N	<chem>O=C(CCI)N([C@@H]1CCCN(C1)C(=O)c2ccc(cc2)N3CCOCC3)c4cccc4</chem>	covalent modifier of catalytic cysteine of pro-CASP8	CASP8	16
WPTTVJLTNAWYAO-KPOXMGGZSA-N	<chem>COC(=O)[C@]15CCCC(C)(C)[C@H]1[C@H]4C(=O)C=C3[C@@]2(C)C=C(C#N)C(=O)C(C)[C@H]2CC[C@@]3(C)[C@]4(C)CC5</chem>	Angiogenesis Inhibitors;Antiinflammatory Drugs;Apoptosis Inducers;Bcl-2 Inhibitors;Glutathione Reductase (NADPH) Activators;Heme Oxygenase Activators;IKK-1 (IKK-alpha) Inhibitors;NF-kappaB (NFkB) Activation Inhibitors;Nitric Oxide Production Inhibitors;Nuclear Factor, Erythroid Derived 2, Like 2 (Nrf2) Activators;PPARgamma Agonists	KEAP1,IKKBK	41
QAIPRVGONGVQAS-DUXPYHPUSA-N	<chem>OC(=O)/C=C/c1ccc(O)c(O)c1</chem>	5-Lipoxygenase Inhibitors;HIV Integrase Inhibitors;Antioxidants	ALOX5	30
JDJGAAQTPZJIDZ-UHFFFAOYSA-P	<chem>C[n+ ]2cccc1cc(ccc12)NC(=O)c3cccc(c3)C(=O)Nc5ccc4c(ccc[n+ ]4C)c5</chem>	Telomerase Inhibitors;DNA G-quadruplex (G4) Ligands	TERT	28
DFBIRQPKNDILPW-KTGKZQHOSA-N	<chem>CC(C)[C@]17O[C@H]1[C@@H]2O[C@]26[C@]3(O)[C@H]3CC5C4COC(=O)C=4CC[C@]56C)[C@H]7O</chem>	ERCC3 (TFIIH subunit)	ERCC3	35
FJHBVJOVLFPMQE-QFIPXVFZSA-N	<chem>CCc4c1cc(O)ccc1nc5C3=CC2=C(CO)C(=O)[C@]2(O)CC)C(=O)N3Cc45</chem>	Apoptosis Inducers;DNA Topoisomerase I Inhibitors	TOP1	27
NSMRMZWAHUBRPG-UHFFFAOYSA-N	<chem>NC(=O)CCNc1cc(ccn1)c3ccnc(Nc2ccc(Cl)c2)n3</chem>	CDK1 Inhibitors	CDK1	30
MYKJVLTXPNIGOV-KTKRTIGZSA-N	<chem>CCN(C/C=C/c2ccc(C1CCCC1)c(Cl)c2)C3CCCC3</chem>	sigma1 Receptor Ligands;sigma2 Receptor Ligands	SIGMAR1	30
NDDAHWYSQHTHT-UHFFFAOYSA-N	<chem>CC2Cc1cccc1N2NC(=O)c3ccc(Cl)c(c3)S(N)=O</chem>	Carbonic Anhydrase Type VII Inhibitors	CA4,CA5A,CA7,CA12,CA5B	38
KXMZDGSRSRSGHMMK-VWLOTQADSA-N	<chem>NC4=NC(Nc2ccc1CC[C@@H](CCc1c2)N3CCCC3)=NN4c7cc6CCc5ccccc5c6nn7</chem>	Axl tyrosine kinase receptor inhibitor	AXL	22
JADDQZYHOWSFJD-FLNNQWLSA-N	<chem>CCNC(=O)[C@H]1O[C@H]([C@H](O)[C@@H]1O)N3C=Nc2c(N)ncn23</chem>	Adenosine Receptor Agonists	ADORA2A	31
BCWCEHMHCDJCAD-UHFFFAOYSA-N	<chem>Cc1ccc(cc1)C(=O)C(=O)c2ccc(C)cc2</chem>	Carboxylesterase Inhibitors	CES1,CES2,CES3,CES1P1,CES5A	35
PCFKMZRPZATASD-UHFFFAOYSA-N	<chem>CS(=O)(=O)N5CC1(CCN(CC1)C(=O)Nc2cnc(cn2)c3ccccc3)c4cccc45</chem>	Neuropeptide Y5 (NPY Y5) Antagonists	NPY5R	43
AUVVAXYIELKVAI-CKBKHPWSA-N	<chem>CC[C@H]3CN2CCc1cc(OC)c(cc1[C@H]2C[C@@H]3C[C@H]4NCc5cc(OC)c(cc45)OC)OC</chem>	Translation inhibitor	RPS14,RPS20	34
TXJZRSRTPUYRW-NQIIRXRSA-N	<chem>COC(=O)c1ccc(cc1)[C@H]4C3Nc2ccc(cc2C=3C[C@H](C(=O)OC)N4C(=O)C(Cl)</chem>	GPX4 covalent inhibitor	GPX4	20
DZIUPOCVDSYPSY-UHFFFAOYSA-N	<chem>Cc1c(ccc2NC=Cc12)Nc3c(C#N)cncc3C6=Cc5cc(CN4CCN(C)CC4)ccc5O6</chem>	Protein Kinase PKC theta Inhibitors	PRKCQ	39
RDONXGFGWSSFMY-UHFFFAOYSA-N	<chem>CCS(=O)(=O)Nc2ccc(Oc1ccc(F)cc1F)c(c2)C3=CN(C)C(=O)C4NC=CC3=4</chem>	Bromodomain-Containing Protein 4 (Brd4, HUNK1) Inhibitors	BRD4	33
CEGSUKYESLWKJP-UHFFFAOYSA-N	<chem>C(CC1=CNc2ccccc12)Nc3ccc(cc3)Nc4cnc4</chem>	MDM2 (hdm2) Inhibitors	MDM2	34
FJDDSMSDZHURBJ-UHFFFAOYSA-N	<chem>COc2ccc1NC(I)=C(CCNC(C)=O)c1c2</chem>	MTNR1A agonist;MTNR1B agonist	MTNR1A,MTNR1B	38
YKJYKKNCCRKFSL-BFHYXJOUSA-N	<chem>COc2ccc(C[C@@H]1NC[C@@H](O)[C@@H]1OC(C)=O)cc2</chem>	translation inhibitor	RPL3,RPL8,RPL11,RPL15,RPL19,RPL23A,RPL	45



Inchi-key	SMILES	MOA	GeneIDs	Median adj. cone survival (%)
			37,RPL23,RPL13A,RPL26L1,RSL24D1,RPL10L	
JRWROCI MS DXGOZ-UHFFFAOYSA-N	<chem>CC(C)(C)c1ccc(cc1)S(=O)(=O)Nc2ccc(Cl)cc2C(=O)c3cc[n+][[O-]]cc3</chem>	CCR9 chemokine antagonist	CCR9	39
RVKFQAJXCZXQY-CBZIJGRNSA-N	<chem>C[C@]34CC[C@@H]2c1ccc(cc1CC[C@@H]2[C@@H]3CCC4=O)OS(N)(=O)=O</chem>	Estrogen Receptor (ER) Agonists; Steryl Sulfatase Inhibitors	STS	41
RPDFDSQFBCJTDY-GAQXSTBRSA-N	<chem>CC(C)Oc6cc(CC(=O)N4CCC[C@@](CC[N+]12CCC(CC1)(CC2)c3ccccc3)(C4)c5cc(Cl)c(Cl)cc5)ccc6</chem>	Tachykinin NK1 Antagonists	TACR1	38
FDWQSLRDIBRKEI-UHFFFAOYSA-N	<chem>CC(C)(C)C3=CN=C(CSC2=CN=C(NC(=O)Cc1ccc(CNC(CO)CO)cc1)S2)O3</chem>	CDK2/Cyclin E Inhibitors; CDK1 Inhibitors; CDK4 Inhibitors	CCNE1,CDK1,CDK2,CDK4,CCNE2	33
ULKIYKLTIXRBOD-UHFFFAOYSA-N	<chem>OC(=O)C(CP(O)(O)=O)c1ccccc1</chem>	Glutamate Carboxypeptidase II (NAALADase; NAAG Peptidase, FOLH1, PSMA) Inhibitors	FOLH1	34
NICHJJOSEXYBED-AMGIVPHBSA-N	<chem>CC(C)C[C@H](NC(=O)CCN(C)C)c1cc(Cl)ccc1N2CCN(CC2)C(=O)[C@H](C)Cc3ccc(Cl)cc3</chem>	Melanocortin MC4 Receptor Antagonists	MC4R	37
HUNGUWOZPQBXGX-UHFFFAOYSA-N	<chem>O=C(Cc1ccc(c[n1]c2ccc(cc2)OCCN3C COCC3)NC4CCCC4</chem>	c-src allosteric inhibitor; allosteric Src inhibitor; Src Kinase Inhibitors; Antimitotic Drugs; Inhibitors of Signal Transduction Pathways; Tubulin polymerization inhibitors	SRC, TUBG2	38
IRGAIDAWHGYOKD-UHFFFAOYSA-N	<chem>COc1cc(F)c(cc1OC)C4Nc3ncc(Cl)c(NCC2CCNCC2)c3N=4</chem>	JAK1 selective inhibitors	CDK2, JAK1, AURKB	36
NCNRHFGMJRPRSK-MDZDMXLPSA-N	<chem>ONC(=O)/C=C/c1cccc(c1)S(=O)(=O)Nc2ccccc2</chem>	HDACs; Apoptosis Inducers; Histone Deacetylase 1 (HDAC1) Inhibitors; Histone Deacetylase 2 (HDAC2) Inhibitors; Angiogenesis Inhibitors	HDAC1, HDAC2, HDAC9, HDAC5, HDAC7, HDAC8, HDAC11, HDAC10	30
RGXYAZGELLKDA-UHFFFAOYSA-N	<chem>[O-][N+](=O)C1=CC=C(SCCCCCO)C2=NON=C12</chem>	Glutathione-S-Transferase P1 (GSTP1) Inhibitors	GSTM2, GSTP1	36
RZKDEGZIFSJVNA-IBGZPJMESA-N	<chem>C[C@H]4CN(Cc3ccc(CC(=O)N1CCC(CC1)Nc2cccc(F)c2)cc3)CCN4</chem>	Motilin Receptor Agonists	MLNR	34
YUJFUSDUQKTNNX-UHFFFAOYSA-N	<chem>Cc4cccc5C(CC1C(=O)N(CCCCCN)C(=O)N1S(=O)(=O)c2cc(C(=O)N(C)C)c(cc2)Oc3cc(Cl)c(O)cc3)=CNc45</chem>	SSTR2 agonist	SSTR2	37
UKMJWGFHXMGNG-VZUYHUTRSA-O	<chem>CCCC[P+](CCCC)(CCCC)Cc1ccc(cc1)NC(=O)[C@@H](Cc3ccc2cccc2c3)N/C(/NC4CCCC4)=N/C5CCCC5</chem>	BDKRB2 antagonist	BDKRB2	35
WRWCAQNPEXYGJK-PKNBQFBNSA-N	<chem>CC2(C)CCC(C)(C)c1cc(ccc12)C3CCC4OC(/C=C/C(O)=O)=CC3=4</chem>	Retinoid RXRalpha Agonists	RXRA	38
SBOKKVUBLNZTCT-OUKQBFOZSA-N	<chem>Oc3nc1ccc(Cl)cc1c(c2ccccc2)c3C(=O)/C=C/C5Nc4cccc4N=5</chem>	Apoptosis Inhibitors; PKB alpha/Akt1 Inhibitors	AKT1	39
FIVPIPIDMRVLAY-RBJBARPLSA-N	<chem>CN3C(=O)[C@]24CC1=CC=C[C@H](O)[C@H]1N2C(=O)[C@@]3(CO)SS4</chem>	NF-kappaB (NFKB) Activation Inhibitors	SUV39H1	37
MPUQHZXIXSTTDU-QXGSGNESAS-N	<chem>NS(=O)(=O)OC[C@@H]1C[C@H](C[C@@H]1O)N5C=Cc4c(N[C@H]2CCc3ccccc23)ncnc45</chem>	NEDD8-Activating Enzyme (NAE) Inhibitors	NAE1, UBA3	41
UBPYLKGKZZVDX-UHFFFAOYSA-N	<chem>COc4cc(Nc2c1cc(OC)c(cc1ncc2C#N)OCCCN3CCN(C)CC3)c(Cl)cc4Cl</chem>	Abl Kinase Inhibitors; Apoptosis Inducers; Bcr-Abl Kinase Inhibitors; Inhibitors of Signal Transduction Pathways; Src Kinase Inhibitors; STAT-5 Inhibitors	FYN	44
OJCKRNPLOZHAOU-MNKIFKDHSAS-N	<chem>C[C@H]1C[C@@H](C)[C@H](C)[C@@H](O)C(/C#N)=C/C=C/C[C@H](O)C(=O)[C@H](O)[C@@H](C)C1)[C@@H]2CCC[C@H]2C(O)=O</chem>	Translation inhibitor; TARS inhibitor; angiogenesis inhibitor	TARS1	39
VRQMAABPASPXMW-HDICACEKSA-N	<chem>COc4cc(CCC3C=C(NC(=O)c1ccc(cc1)N2[C@@H](C)N[C@@H](C)C2)NN=3)cc(c4)OC</chem>	FGFR1 gene inhibitor	FGFR1	37

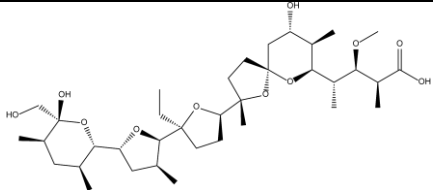
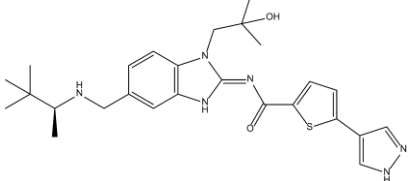
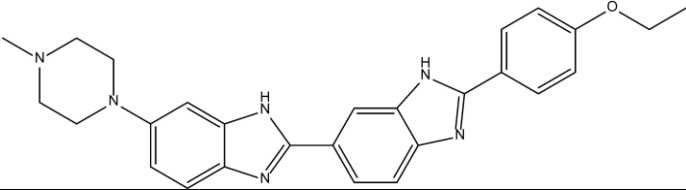
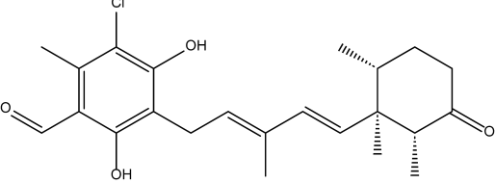
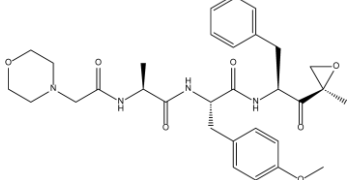
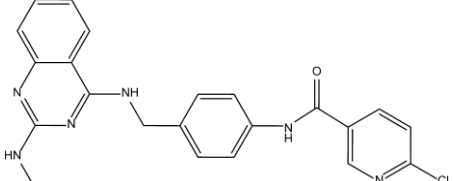


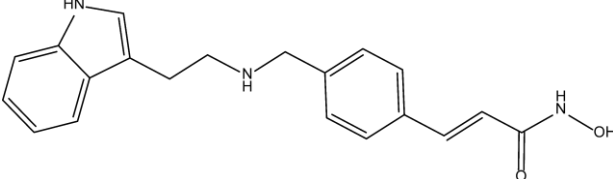
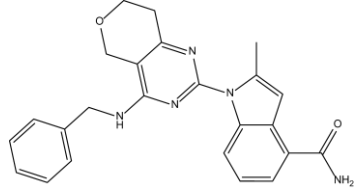
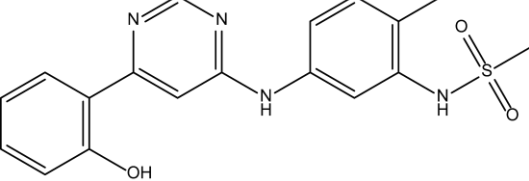
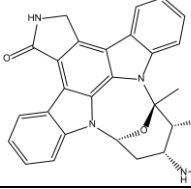
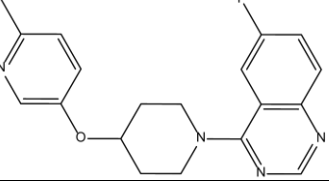
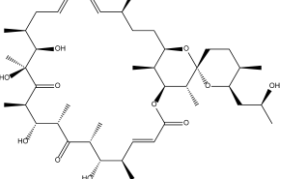


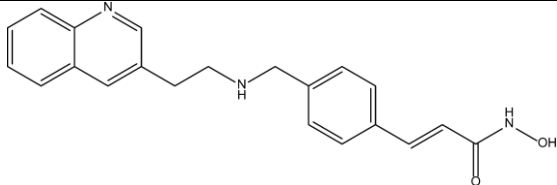
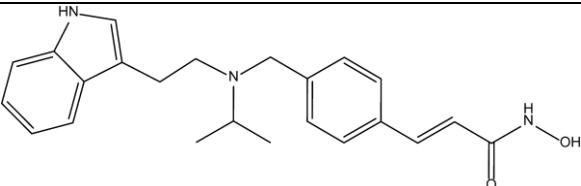
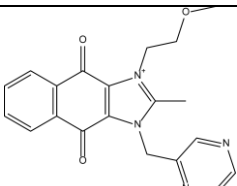
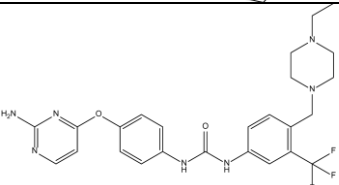
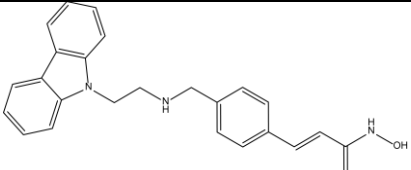
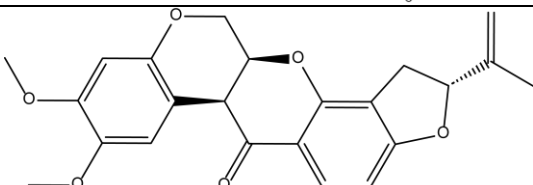
Inchi-key	SMILES	MOA	GeneIDs	Median adj. cone survival (%)
RPGDCRNUJYFGLT-UHFFFAOYSA-N	<chem>CC(CN)C1=CNc2ccc(O)cc12</chem>		HTR1F	34
LCNDUGHNYMJGIW-UHFFFAOYSA-N	<chem>CN2C(=O)C1C(=NOC=1C=C2c3ccccc3)c4ccccc4</chem>	mgluR7 Antagonists	GRM7	42
XQVVPGYIWAGRNI-JOCHJYFZSA-N	<chem>CC[C@@H]4C(=O)N(C)c3cnc(Nc1ccc(cc1OC)C(=O)NC2CCN(C)CC2)nc3N4C5CCCC5</chem>	Antimitotic Drugs;Polo-like Kinase-1 (Plk-1) Inhibitors	PLK1,BRD4	46
HHOVRZGUSBMKKU-ZDUSSCGKSA-N	<chem>CNc1nccc(n1)C2=CC=C(S2)C(=O)N[C@H](CN)Cc3ccc(Cl)cc3Cl</chem>	PKA and AKT (a.k.a. PKB)	AKT1	36
MRBBFOWSPXHYQT-FCXRPNKRSA-N	<chem>COc3cc(/C=C/C2=CC(\C=C\c1ccc(O)c(c1)OC)=NO2)ccc3O</chem>	beta-Amyloid (Abeta) Aggregation Inhibitors;Cyclooxygenase-1 Inhibitors;Cyclooxygenase-2 Inhibitors;Free Radical Scavengers	APP,PTGS1,PTGS2	45
PPLNRTPNYCWODC-UHFFFAOYSA-N	<chem>Oc3cc2Nc1ccccc1c2cc3C(=O)Nc4ccc(Cl)cc4</chem>	Carboxylesterase Inhibitors	CES2	36
QMCXVSJLYBVIHV-VXGBXAGGSA-N	<chem>C[C@@H]1CC(C[C@@H](C)N1)Nc2nccc(n2)C3=CNc4c(F)cccc34</chem>	IKBKB inhibitor	IKBKB	41
VRYZCEONIWEUAV-UHFFFAOYSA-N	<chem>Cc1cc(C)cc(c1)C(=O)NOCCCCC(=O)NO</chem>	HDAC 4/5	HDAC4,HDAC5	40
RTKIYFITIVXBLE-WKWSCTOISA-N	<chem>C/C(/C=C/C(=O)NO)=C\C(C)C(=O)c1ccc(cc1)N(C)C</chem>	HDAC inhibitor	HDAC1,HDAC3,HDAC4,HDAC6,HDAC10	21
TZZISDZOBASIEO-UHFFFAOYSA-N	<chem>CC(C)N4C=C(c2ccnc(Nc1cc(ccc1C)C(N)=O)n2)c3ccncc34</chem>	NFkappaB-inducing kinase (NIK;MAP3K14) Inhibitors	MAP3K14	44

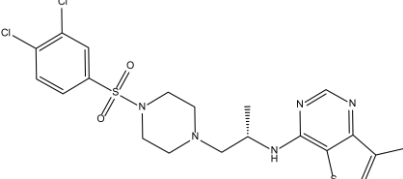
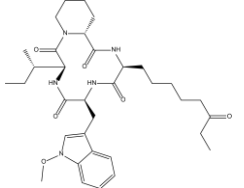
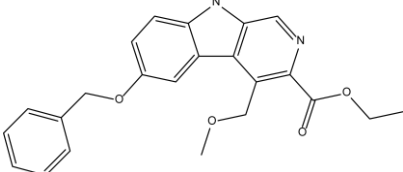
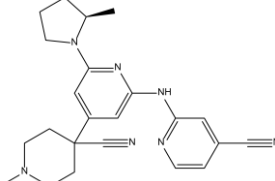
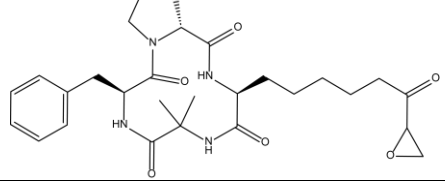
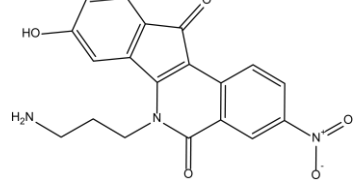
**Table S1:** Compound summary of all significant cone-damaging compounds of the primary screen.

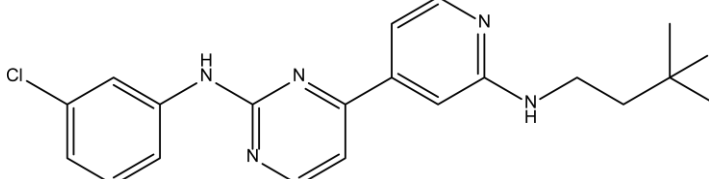
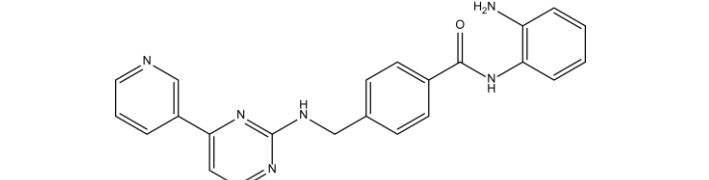
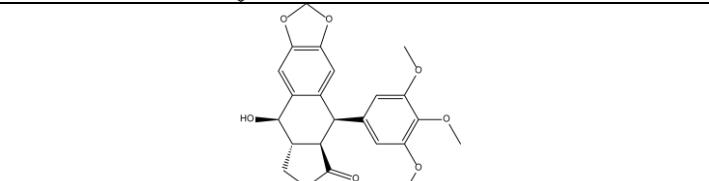
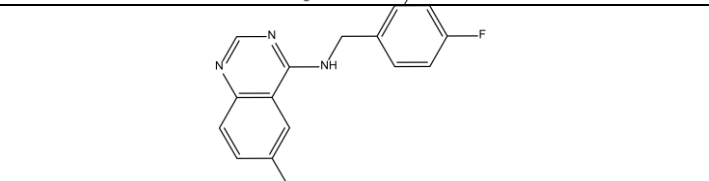
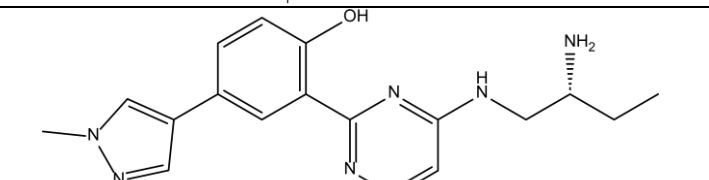
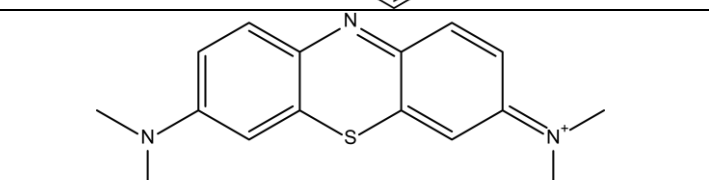
**Table S2**

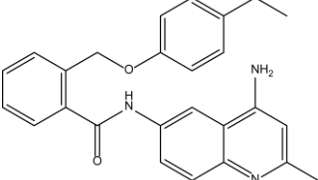
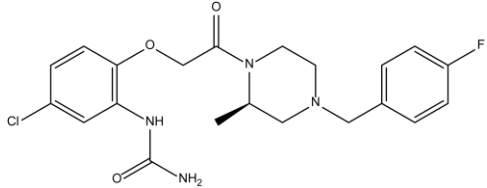
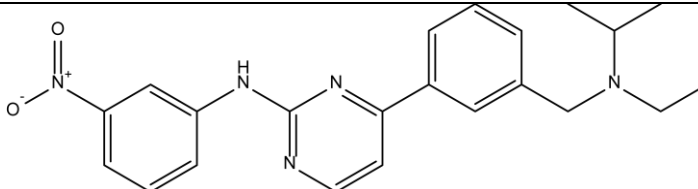
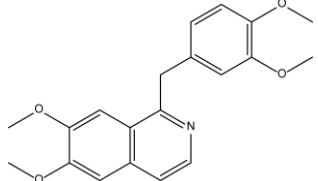
MOA-name	Structure	Inchi-key	Median cone survival (%)				Significant at any concentration
			0.01 $\mu$ M	0.1 $\mu$ M	1 $\mu$ M	10 $\mu$ M	
Sodium ionophore		GAOZTHIDHYLHMS-KEOBGNEYSAN	99	34	31	8	*
ITK Kinase inhibitor		MUAICZWSFWUFNA-INIZCTEOSAN	100	92	91	14	*
BCL2L1 inhibitor		PRDFBSVERLRRMY-UHFFFAOYSAN	104	111	64	14	*
AP-1 inhibitor		SETVRSKZJJWOPA-FLDGXQSCSAN	105	111	14	29	*
Immunoproteasome inhibitor		WQAVPPWLLVGFK-VTNASVEKSAN	101	106	53	11	*
Beta-Catenin inhibitor		PIROHBFQHMKAPE-UHFFFAOYSAN	106	92	98	21	*

MOA-name	Structure	Inchi-key	Median cone survival (%)				Significant at any concentration
			0.01 $\mu$ M	0.1 $\mu$ M	1 $\mu$ M	10 $\mu$ M	
HDAC inhibitor 3		ZLUZDKXBTNQWOL-MDZDMXLPSA-N	93	68	52	22	*
AAA ATPase p97 inhibitor		RDALZZCKQFLGJP-UHFFFAOYSA-N	104	102	25	26	*
CDK1-2 inhibitor		HPTMTYKYKUKYCQ-UHFFFAOYSA-N	101	90	120	22	*
Staurosporine		HKSZLNNOFSGOKW-FYTWWXJKSA-N	73	89	69	24	*
PAM of mAChR		SMYUEWYXIKCMEA-UHFFFAOYSA-N	95	106	105	25	*
Inhibitor of mitochondrial ATPase		MNULEGDCPYONBU-WMBHJXFZSA-N	92	32	58	58	*

MOA-name	Structure	Inchi-key	Median cone survival (%)				Significant at any concentration
			0.01 $\mu$ M	0.1 $\mu$ M	1 $\mu$ M	10 $\mu$ M	
HDAC inhibitor 1		NLKQTNQJKCBXMU-MDZDMXLPSA-N	91	85	57	32	*
HDAC inhibitor 6		ILAZEUQQANOTAY-VAWYXSNFSA-N	91	63	70	33	*
BIRC5 gene inhibitor		OTSOOHRUMBRSHZ-UHFFFAOYSA-N	92	72	66	31	*
FLT3 inhibitor		VQQRBBFRJRBWPF-UHFFFAOYSA-N	104	94	90	31	*
HDAC inhibitor 4		ATSUJKLLCSXMLV-BUHFOSPRSA-N	93	78	44	36	*
Complex I inhibitors		JUVIOZPCNVVQFO-HBGVWJBISA-N	104	39	81	60	*

MOA-name	Structure	Inchi-key	Median cone survival (%)				Significant at any concentration
			0.01 $\mu$ M	0.1 $\mu$ M	1 $\mu$ M	10 $\mu$ M	
LPA 2 receptor antagonist		BPRNMVDTWIHULJ-AWEZLNQCLSA-N	104	109	98	20	*
HDAC inhibitor 5		JWOGUUIOCYMBPV-GMFLJSBRSA-N	100	95	80	36	*
Anxiolytic		ALBKMJDFBZVHAK-UHFFFAOYSA-N	103	105	105	21	*
MAP3K12 inhibitor		SXHHURZUIGDYAR-QGZVFWFLSA-N	89	111	111	19	*
HDAC inhibitor 2		SGYJGGKDGBXCNY-ZDIDWYTNSA-N	85	66	68	49	*
Top1-TDP1 inhibitor		OKJDLRMQHZRYOZ-UHFFFAOYSA-N	108	98	99	43	*

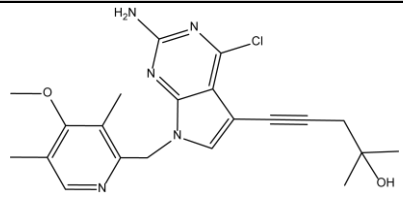
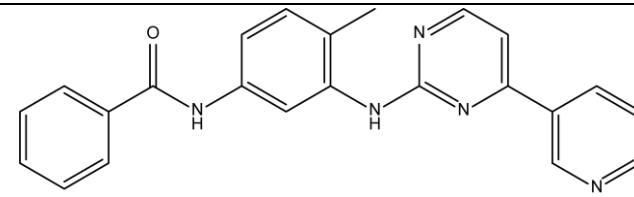
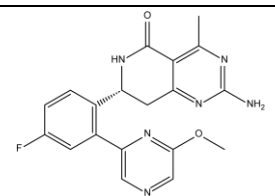
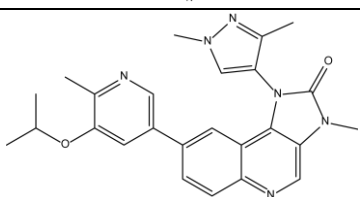
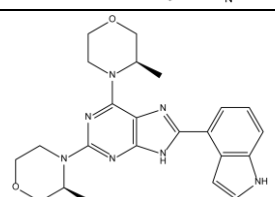
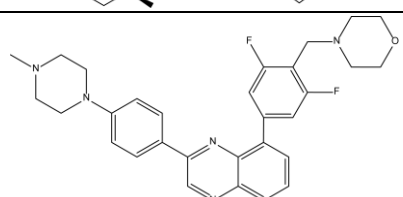
MOA-name	Structure	Inchi-key	Median cone survival (%)				Significant at any concentration
			0.01 $\mu$ M	0.1 $\mu$ M	1 $\mu$ M	10 $\mu$ M	
CDK1 inhibitor		AAAAA	111	101	91	39	*
HDAC inhibitor 7		HRNLUBSXIHFDHP-UHFFFAOYSA-N	98	101	90	57	*
Antimitotic Agent		YJGVMLPVUAXIQN-XVVDYKMHSA-N	112	79	49	72	*
PDE5A inhibitor		AWIVHRPYFSSVOG-UHFFFAOYSA-N	98	108	112	41	*
PKD inhibitor		SCJXQZZYGYLKJG-CQSZACIVSA-N	95	103	99	62	*
Tau Aggregation inhibitor		RBTFTRPCNLSDE-UHFFFAOYSA-N	105	107	96	79	

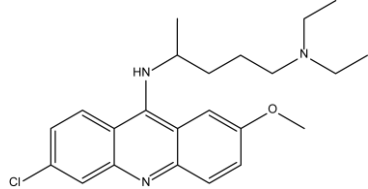
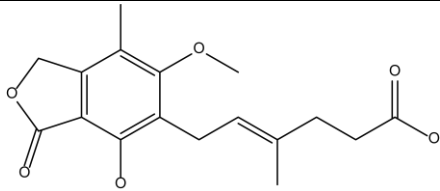
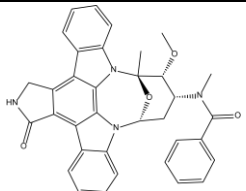
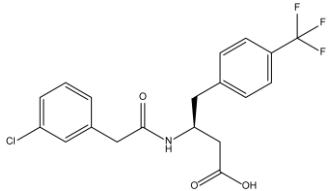
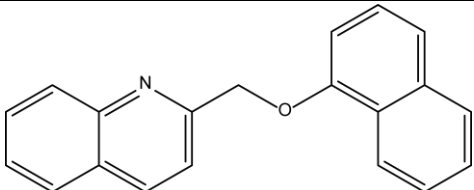
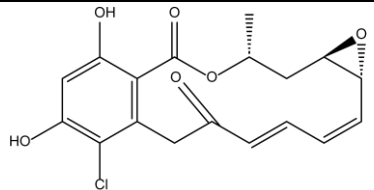
MOA-name	Structure	Inchi-key	Median cone survival (%)				Significant at any concentration
			0.01 $\mu$ M	0.1 $\mu$ M	1 $\mu$ M	10 $\mu$ M	
OPRL1-OPRM1- gene inhibitor		VTGBZWHPJFMTKS-UHFFFAOYSA-N	105	106	107	84	
Chemokine CCR1 antagonist		XQYASZNUFDVMFH-CQSZACIVSA-N	115	106	124	85	
Antimitotic drug		QPKKAIMODKGHRH-UHFFFAOYSA-N	96	111	110	83	
PDE10A inhibitor		XQYZDYMELSDJRZ-UHFFFAOYSA-N	107	114	99	78	

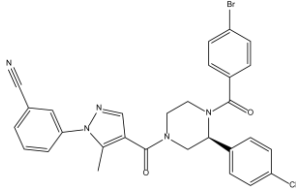
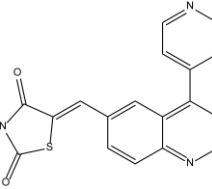
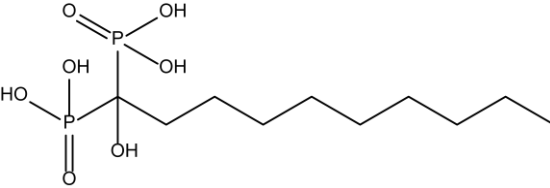
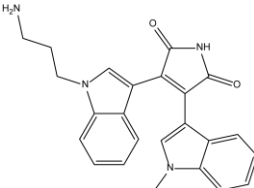
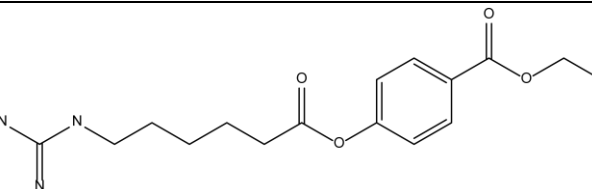
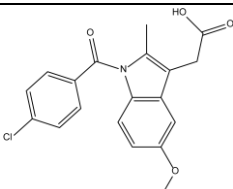
**Table S2:** Compound summary of all retested cone-damaging compounds in the secondary screen.

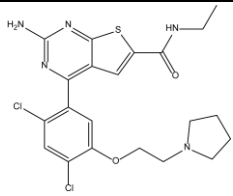
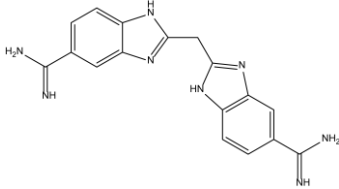
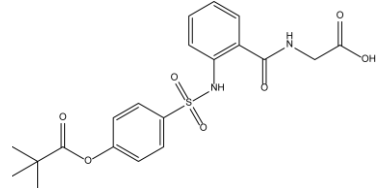
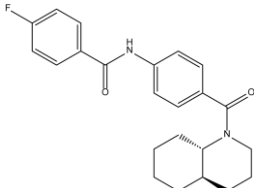
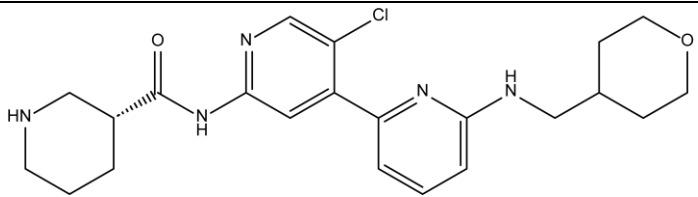
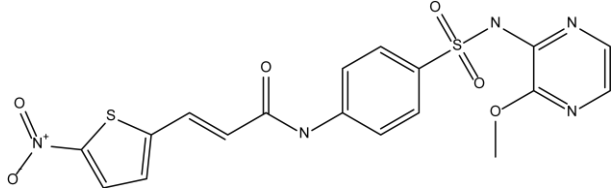


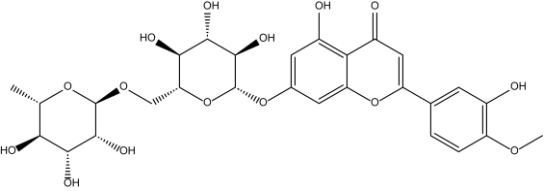
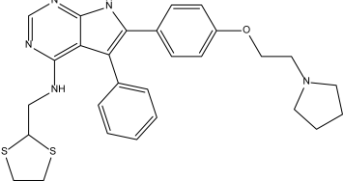
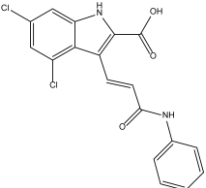
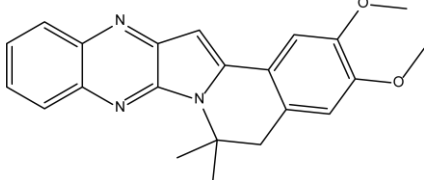
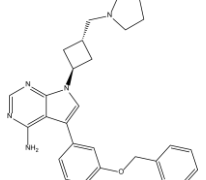
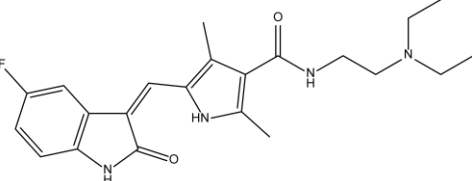
**Table S3**

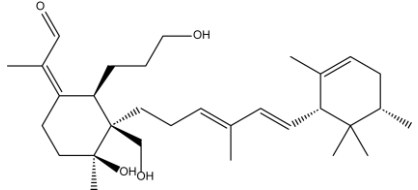
MOA-name	Structure	Inchi-key	Median adj. cone survival (%)				Significant at any concentration
			0.01 $\mu$ M	0.1 $\mu$ M	1 $\mu$ M	10 $\mu$ M	
HSP90 inhibitor 2		VOASEWXFCTZRDF-UHFFFAOYSA-N	67	78	84	71	*
PDGFR inhibitor 1		UOEJSOXEHKCNAE-UHFFFAOYSA-N	58	47	54	81	*
HSP90 inhibitor 1		XRFHWSYKRFEPRACYBMUJFWSA-N	70	71	80	78	*
MTOR inhibitor 1		YWDAJLXJSLKKPA-UHFFFAOYSA-N	61	67	61	76	*
MTOR inhibitor 2		BYPBFDASESWSQGCABCVRRESA-N	59	49	47	72	
Jak1-2 inhibitor		LBZZVBOHWAZYRL-UHFFFAOYSA-N	59	72	55	56	

MOA-name	Structure	Inchi-key	Median adj. cone survival (%)				Significant at any concentration
			0.01 $\mu$ M	0.1 $\mu$ M	1 $\mu$ M	10 $\mu$ M	
TP53 expression enhancer		GPKJTRJOBQGKQK-UHFFFAOYSA-N	63	49	70	61	
IMPDH inhibitor		HPNSFSBZBAHARI-RUDMXATFSA-N	59	50	66	69	
Flt3-PKC-inhibitor		BMGQWWWVWDBQGC-IIFHNQTCSA-N	51	60	52	67	
GPR43 antagonist		QOSIJVVNNGXEKE-INIZCTEOSA-N	51	54	67	53	
Lipoxygenase inhibitors		NZLDBNPKNBCGEN-UHFFFAOYSA-N	54	59	58	67	
HSP90 gene modulator		WYZWZEOGROVHK-GTMNPGAYSA-N	60	58	65	56	

MOA-name	Structure	Inchi-key	Median adj. cone survival (%)				Significant at any concentration
			0.01 µM	0.1 µM	1 µM	10 µM	
EIF4A3 inhibitor		BDGKKHWJYBQRIE- HHHXNRCGSA-N	52	36	50	64	
PI3Kalpha inhibitor		QDITZBLZQQZVEE- YBEGLDIGSA-N	58	58	49	63	
GGPS1 inhibitor		NSCPCMXXWUFFNL- UHFFFAOYSA-N	58	55	51	63	
PKC inhibitor		UQHKJRCFSLMWIA- UHFFFAOYSA-N	53	62	60	57	
AP-1-tryptase-MATE1 inhibitor		YKGYIDJEEQRWQH- UHFFFAOYSA-N	62	58	54	62	
Cyclooxygenase inhibitor		CGIGDMFJXJATDK- UHFFFAOYSA-N	58	60	46	62	

MOA-name	Structure	Inchi-key	Median adj. cone survival (%)				Significant at any concentration
			0.01 $\mu$ M	0.1 $\mu$ M	1 $\mu$ M	10 $\mu$ M	
HSP90 inhibitor 3		WJUNQSYQHIVFX-UHFFFAOYSA-N	59	61	54	62	
Protease inhibitor		QZKOOEFIMWKZPK-UHFFFAOYSA-N	57	55	49	62	
Elastase inhibitor		BTGNGJLZOIYID-UHFFFAOYSA-N	59	61	55	60	
11beta-HSD1 inhibitor		WSUXACNDZSQZBC-IERDGPVSA-N	55	54	61	56	
CDK9 inhibitor		PHESISZXAITBIM-MRXNPFEDSA-N	59	60	52	59	
Covalent necroptosis inhibitor		FNPPHVLYVGMZMZ-XBXARRHUSA-N	51	56	60	56	

MOA-name	Structure	Inchi-key	Median adj. cone survival (%)				Significant at any concentration
			0.01 $\mu$ M	0.1 $\mu$ M	1 $\mu$ M	10 $\mu$ M	
AhR agonist		GZSOSUNBTXMUFQ-YFAPSIMESA-N	55	55	60	52	
ACK inhibitor		ZJLXSIPWULUCRJ-UHFFFAOYSA-N	52	42	39	59	
NMDA glycine-site antagonist		WZBNEZWCNKUOSM-VOTSOKGWSA-N	58	50	49	48	
IL-5R antagonists		HIXSPVQXXDULHS-UHFFFAOYSA-N	55	50	56	53	
IGF-1R inhibitor		LSFLAQVDISHMNB-AFARHQOCSA-N	50	51	54	56	
Receptor tyrosine kinase inhibitor		WINHZLLDWRZWRT-ATVHPVEESA-N	53	49	54	50	

MOA-name	Structure	Inchi-key	Median adj. cone survival (%)				Significant at any concentration
			0.01 $\mu$ M	0.1 $\mu$ M	1 $\mu$ M	10 $\mu$ M	
Lymphangiogenesis inducer		CUWJDZXEDIUEEW-HLFHJSLSSA-N	42	47	44	50	

**Table S3:** Compound summary of all retested cone-saving compounds in the secondary screen.

**Table S4**

Target	Species	Dilution	Source	Identifier
Bassoon	Mouse (monoclonal)	1:800	Enzo	SAP7F407
ARR3	Mouse (monoclonal)	1:500	Gift from the Laboratory of Wolfgang Baehr, University of Utah	-
NRL	Goat (polyclonal)	1:500	R&D systems	AF2945-SP
ONECUT2	Sheep (polyclonal)	1:100	R&D systems	AF6294
SOX9	Rabbit (polyclonal)	1:500	Millipore	AB5535
TRPM1	Rabbit (polyclonal)	1:200	ATLAS	HPA014779
CHAT	Goat (polyclonal)	1:300	Merck Millipore	AB144P
mCAR	Rabbit (polyclonal)	1:200	Merck Millipore	AB15282

**Table S4:** Primary antibody list